Winter 12-15-2017

Characterization of Structural Dynamics of the Human Head using Magnetic Resonance Elastography

Andrew Arun Badachhape
Washington University in St. Louis

WASHINGTON UNIVERSITY IN ST. LOUIS

School of Engineering and Applied Sciences

Department of Biomedical Engineering

Dissertation Examination Committee:
Philip V. Bayly, Chair
Hong Chen
Ruth J. Okamoto
Jin-Yu Shao
Joshua S. Shimony

Characterization of Structural Dynamics of the Human Head using Magnetic Resonance Elastography

by

Andrew A. Badachhape

A dissertation presented to
The Graduate School
of Washington University in
partial fulfillment of the
requirements for the degree
of Doctor of Philosophy

December 2017
Saint Louis, Missouri

Table of Contents

List of Figures

List of Tables

Acknowledgments

Dr. Philip Bayly provided exceptional mentorship and support over the course of my doctoral research. His wealth of knowledge, attention to detail, and near-limitless energy inspired me to push boundaries and ask big questions in this work. I deeply thank him for providing me with a rewarding and scientifically rigorous research project.

Dr. Ruth Okamoto was instrumental in the design and execution of the research in this work. I thank her for the innumerable hours she spent working alongside me to collect and analyze data. Her mentorship and guidance has helped me grow tremendously as a scientist and engineer over the past four years.

Dr. Curtis Johnson provided the MR elastography sequences used throughout this work. MR Technologists Glenn Foster, Scott Love, Mark Nolte, and Laura Foehne at the Washington University Center for Clinical Imaging Research provided indispensable assistance in collecting MRI data from human volunteers and phantoms. Kenji Aono provided the materials and expertise to help fabricate the cranial phantoms studied in my final research aim.

My colleagues in the Bayly lab, John Schmidt and Charlotte Guertler, provided valuable assistance throughout my doctoral training. John helped immensely with finite element modeling data presentation and interpretation. I am deeply grateful for his support and encouragement over the years. Charlotte had a knack for asking the right question at the right time. Her design expertise proved invaluable in the implementation of my accelerometer data collection system.

I also had the privilege of working alongside several exceptional undergraduate researchers: Ramona Durham, Samuel Nadell, Brent Efron, and Jake Ireland. Ramona greatly assisted with anatomical MRI data analysis and segmentation. Samuel performed excellent work on accelerometer array design and testing. Brent performed validation studies to assess the accuracy of motion reconstruction from accelerometers. Jake was instrumental in the design, creation, and testing of Sylgard® phantoms described in my final aim. I looked forward to coming in to lab every day to work alongside my fellow lab members.

This work would not have been possible without the assistance of the wonderful staff in both the Biomedical Engineering and Mechanical Engineering departments at Washington University in St. Louis. Karen Teasdale and Susan Seel provided constant support and guidance throughout my graduate studies. Linda Buckingham, Laura Barker, Felicia Dilworth, and Kevin Cowell helped me navigate administrative tasks and provided me with the resources necessary to complete my research. Gene Bulfin maintained computational and modeling resources crucial to this work.

Financial support for this work was provided by National Institutes of Health (NIH) Grant R01 NS055951 and ONR Grant N00014-15-C-5160.

Andrew Badachhape

Washington University in St. Louis

December 2017

"If I have seen further than others, it is by standing on the shoulders of giants."

-Isaac Newton

To my mother and father, the giants who enabled me to reach for the stars.

ABSTRACT OF THE DISSERTATION

Characterization of Structural Dynamics of the Human Head using

Magnetic Resonance Elastography

by

Andrew A. Badachhape

Doctor of Philosophy in Biomedical Engineering

Washington University in St. Louis, 2017

Professor Philip V. Bayly, Chair

In traumatic brain injury (TBI), the skull-brain interface, composed of three meningeal layers: the dura mater, arachnoid mater, and pia mater, along with cerebrospinal fluid (CSF) between the layers, plays a vital role in transmitting motion from the skull to brain tissue. Magnetic resonance elastography (MRE) is a noninvasive imaging modality capable of providing *in vivo* estimates of tissue motion and material properties. The objective of this work is to augment human and phantom MRE studies to better characterize the mechanical contributions of the skull-brain interface to improve the parameterization and validation of computational models of TBI. Three specific aims were to: 1) relate 3D skull kinematics estimated from tri-axial accelerometers to brain tissue motion (rigid-body motion and deformation) estimated from MRE, 2) modify existing MRE data collection methods to capture simultaneous scalp and brain displacements, and 3) create cylindrical and cranial phantoms capable of simulating a CSF interface and dural membranes. Achievement of these aims has provided new quantitative understanding of the transmission of skull motion to the brain.

Chapter 1: Quantitative Assessment of Skull and Brain Motion for Parameterization and Validation of Head Biomechanics Models

1.1 Overview

Sudden impact or acceleration of the head can lead to traumatic brain injury (TBI), which is associated with a wide spectrum of neurological dysfunction. Though simulation using computational models holds great promise for developing methods for injury prediction and prevention, confidence in the predictions of current models is limited. In particular, the boundary or interface conditions describing the transmission of motion from the skull to the brain are poorly understood. These boundary conditions are clearly different in animal and human heads, due to anatomical differences between species, and are different in cadavers than in live subjects, due to differences in the vasculature and CSF post mortem. Thus, experimental data from coupled skull and brain motion *in vivo* are needed to create more accurate models of TBI in humans. Noninvasive imaging methods such as magnetic resonance elastography (MRE) can be used to provide characterization of skull mechanics and resulting brain tissue motion and deformation. The review presented in this chapter will describe current efforts to model skull and brain kinematics along with the fundamentals and applications of MRE. This section concludes with an overview of three specific aims encompassing efforts to expand understanding of the transmission and attenuation of skull motion to brain tissue.

1.2 Significance

1.2.1 Motion transmission from the skull to the brain is critical for characterizing traumatic brain injury

Traumatic brain injury (TBI), caused by rapid brain tissue deformation in response to sudden linear and angular accelerations of the skull, is a prevalent neurological disorder [1], [2]. Every year, approximately 1.7 million new cases arise in the U.S. with associated costs exceeding $56 billion [1]. Figure 1.1 documents the findings of a recent epidemiology study that compared the costs of TBI to those of other common injuries.

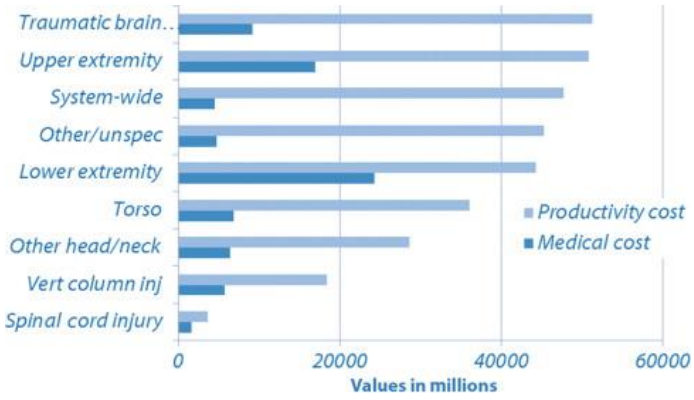

Figure 1.1: Financial burden of injury comparison by body region. Medical costs cover medical treatments, hospitalizations, and deaths within and outside the medical system. Productivity costs are associated with lost wages and benefits due to incapacity to work. Reprinted from [1].

TBI comprises a large set of conditions and symptoms. Concussions are a common type of TBI with transient symptoms of loss of consciousness and/or mild cognitive impairment [3]. In addition to acute or severe trauma, brain injury also occurs from repeated, sub-concussive levels of impact [4]. Blast-induced TBI has also recently emerged as an important medical concern for combat veterans exposed to improvised explosive devices (IED) [5]. It is widely understood that

brain tissue deformation can lead to diffuse axonal injury (DAI), or shearing and stretching of axonal fibers embedded in brain white matter [6]. Studies of neuronal damage resulting from tissue deformation have identified biomarkers that show promise in diagnosing TBI [7], [8].

While the cognitive effects of TBI are well documented, the mechanisms linking mechanical insult and neurological injury are not well understood. Specifically, there is little understanding of how skull motion is transmitted to brain motion during traumatic brain injury. The field of TBI modeling has focused on (i) capturing appropriate material parameters for brain tissue and (ii) creating subject-specific, accurate geometry for finite element models [9]–[11], however the details of the coupling between skull and brain kinematics remain unclear.

There are numerous computational biomechanical models of head dynamics, but evaluating these models is challenging [12]. A common conclusion among these studies is that the interface between the skull and brain, specifically dural membranes, sinuses, and a layer of cerebrospinal fluid (CSF), holds the brain in suspension within the skull and plays a prominent role in motion transmission. Previous work on relating skull and brain motion encompasses studies ranging from animal experiments [13], [14], cadaver experiments [15], [16], human studies using magnetic resonance imaging (MRI) [17]–[20] , and various physical and virtual models [10], [21]–[23]. However, experimental studies of relative skull and brain motion are difficult to perform and interpret. Animal skulls and brains, for instance, are anatomically dissimilar from those of humans, and a cadaver head is quite different from an intact human head *in vivo*. Imaging studies such as those using MRI show great promise in providing *in vivo* assessment of

brain displacement. Skull motion is hard to record using MRI [17], [18], however, due to the low MR signal in bone [24], [25].

1.2.2 The skull-brain interface plays a crucial role in motion transmission during injury

Connections between the skull and brain exist at the brain stem and at various vascular, neural or membranous connections at the base and boundaries of the brain. Inside the skull, the brain is encased in multiple membranes including the dura mater, arachnoid mater, and pia mater. As the skull moves, these membranes and the cerebrospinal fluid (CSF) and blood contained in spaces between the various layers cushion brain tissue and limit its amplitude of motion [21], [26]. Together, these membranes and sinuses, hereafter referred to as the "skull-brain interface", play an integral role in injury mechanics. In addition to being enveloped by a reservoir of CSF in sinuses in the sub-arachnoid space, the brain is coupled to the skull by the falx cerebri and tentorium cerebelli. The falx is an inner fold of the dura mater extending into the longitudinal fissure to separate both hemispheres of the brain. Connecting to the falx posterior is the tentorium, another extension of the dura mater that separates the cerebellum from the occipital lobes. Results from prior research suggest that these membranes play an integral role in transmitting and reflecting shear waves in brain tissue [27].

As a simple model, the brain can be thought of as a mass suspended by springs within a rigid container as shown in Figure 1.2 [18]. Sudden skull motion in this simplified example will induce brain deformation [28], where displacements will be largest near the boundaries where

the skull-brain interface is located. Additionally, one would expect motion to be more constrained near the base, as that is where the brain attachment is likely firmest. The heterogeneity of this attachment and suspension system means that deceleration of the skull (Figure 1.2b) will cause the skull to both translate and rotate even though the skull is only experiencing translational motion. Note in this schematic that the model assumes an elastic interface though viscoelastic effects are more likely to be seen.

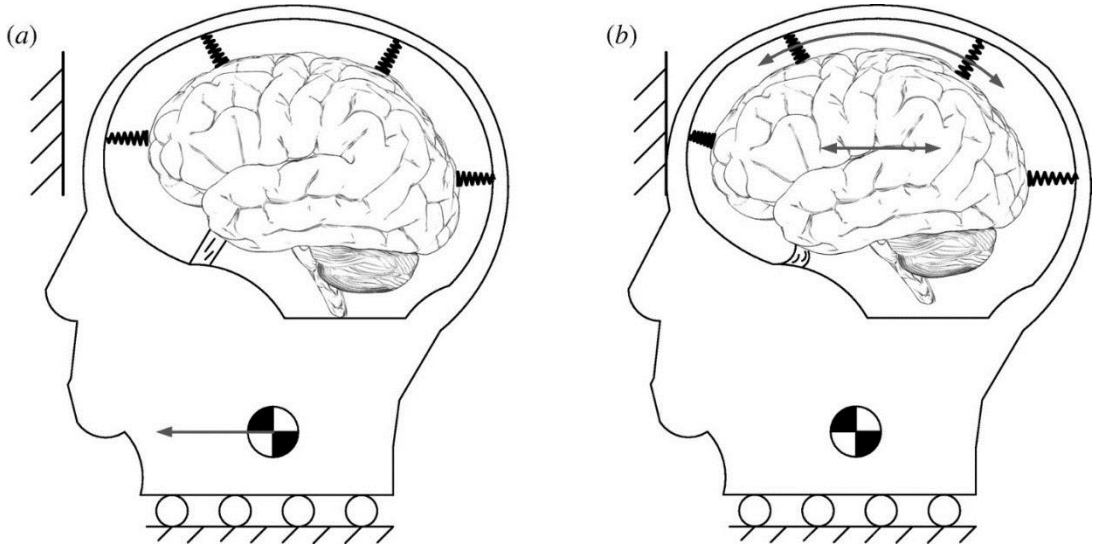

<u>Figure 1.2:</u> A simplified schematic demonstrating brain motion as it is held in suspension within the rigid skull. A) The skull translates towards a platform in the upper left until it collides and B) experiences sudden linear deceleration while the brain undergoes both linear and angular displacement. Reprinted from [18].

Brain displacement does not reflect only rigid-body motion; sudden deceleration can also lead to dynamic deformation [17], [18], [29] reflecting apparent shearing motion of brain tissue.

1.2.3 Computational models of traumatic brain injury require experimental data to model the mechanics of the skull-brain interface

Computational models of TBI have great potential for characterizing TBI. They are capable of replicating injurious levels of skull acceleration that are impossible to do in experimental studies with humans. However, these simulations require accurate tissue material properties, loading conditions, and boundary conditions and must be compared to experimental data for validation.

State of the art finite element (FE) models of human head dynamics boast anatomically accurate features (scalp, cranial bone and fossa, dural membranes, blood vessels, white and gray matter CSF, etc.) along with high spatial and temporal resolution for interaction and boundary conditions [10], [12], [28], [30]. An example model, created by researchers at the KTH Royal Institute of Technology is shown in Figure 1.3. Experimental comparisons of FE models have included cadaver intracranial pressure studies [31] and x-ray studies [32], however there is a pressing need for investigation of mechanical concepts such as tissue strain or strain rate. While FE models gain increased functionality and capability each year, accurate, *in vivo* experimental data that is suitable for comparison is hard to find.

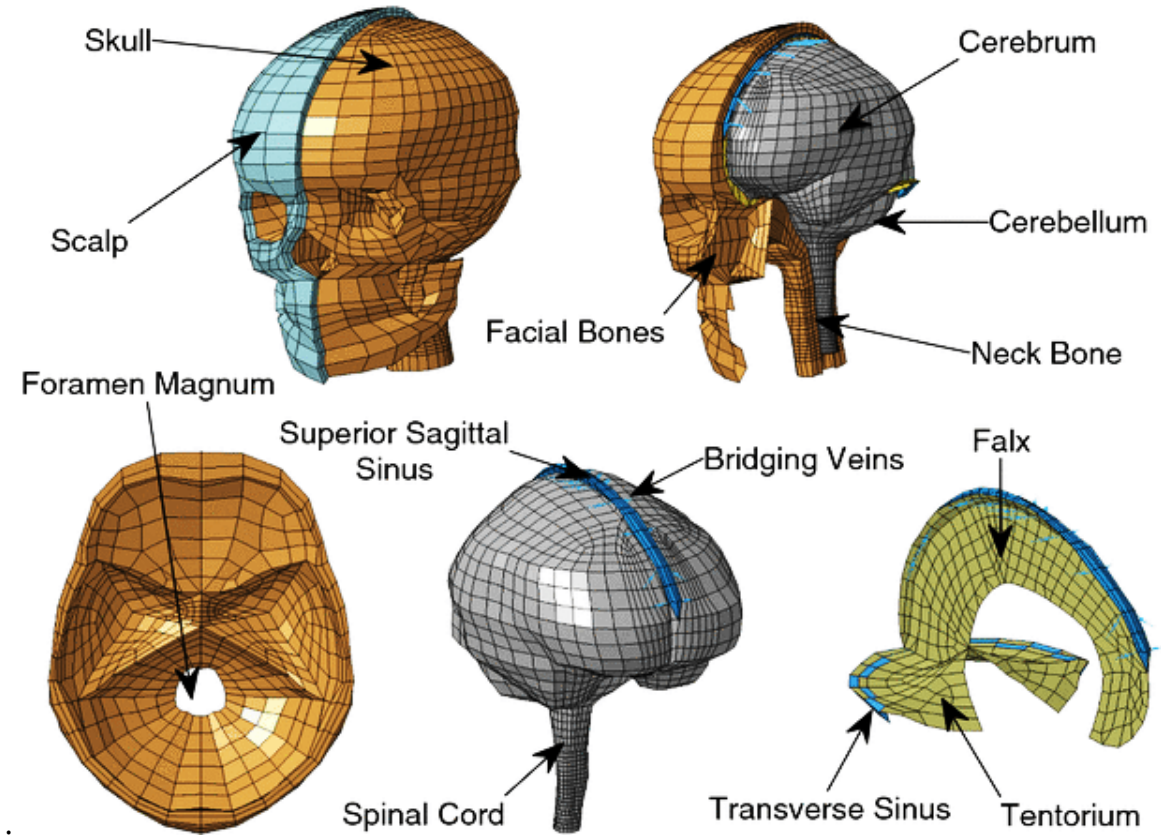

Figure 1.3: Human head FE model created by the Kleiven group at KTH Royal Institute of Technology, Sweden. This computational model has accurate structural and anatomical features and incorporates material behavior taken from experimental data. Reprinted from [33].

Characterizing head dynamics, including both skull and brain motion, through imaging is essential for providing noninvasive, *in vivo* assessments of tissue displacement. Magnetic Resonance Imaging (MRI) studies examining relative head and brain motion *in vivo* have used image registration [20] and MR tagging [17]. Another modality that has the potential for characterizing head dynamics is magnetic resonance elastography (MRE). MRE is a phase-contrast MRI sequence capable of noninvasively describing the material and mechanical properties of biological tissue in vivo [34], [35].

1.3 Measuring Human Brain Tissue Motion with Magnetic Resonance Elastography

1.3.1 Principles of magnetic resonance elastography

MRI is a noninvasive imaging method capable of providing anatomical and functional data on brain tissue. MRI signal is derived from the spin precession of hydrogen nuclei in a strong magnetic field. A material element containing a group of nuclei within the same magnetic field is referred to as a spin packet, or isochromat. The precession of a spin packet is predominantly aligned with the magnetic field but can be altered through use of radiofrequency (RF) pulses. Differences in precession phase and frequency can then be encoded through gradients in the magnetic field, which create spatially varying spin packets. Anatomical MRI images derive contrast from differences in water content or decay of longitudinal (T1) or transverse (T2) components of spin precession. Emphasizing either of these components enables the acquisition of T1-weighted or T2-weighted anatomical images that provide different contrast of brain regions [36]–[38] (Figure 1.4).

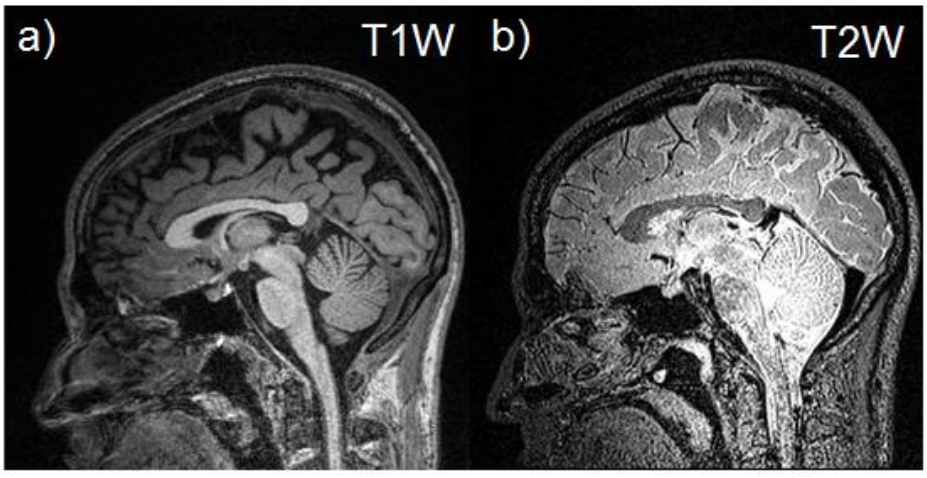

Figure 1.4: a) T1-weighted and b) T2-weighted anatomical images of the human head (sagittal slice).

Phase-contrast MRI methods build upon the fundamental principles of MRI by measuring the relative angular position, or phase, of the transverse magnetization vector for each spin packet. The frequency of precession for each spin packet depends on the local magnetic field strength, which can be altered by the presence of gradients within the magnetic field. These gradients vary temporally and induce changes in the RF signal phase of each packet, which encodes a proportional displacement. If spin packets are moving in the presence of a gradient, they will have different phase than spin packets that remain motionless in the same gradient. The concept of phase-contrast MRI has yielded applications for measuring blood flow using magnetic resonance angiography (MRA) [39] and soft tissue motion and material characterization through magnetic resonance elastography [34].

MRE measures harmonic shear wave propagation through biological soft tissue by synchronizing an applied external vibration with an oscillating magnetic field gradient. MRE enables estimation of tissue motion in response to external actuation. The motion of soft tissue can be described through rigid motion and deformation. For harmonic excitation, deformation is characterized through wave propagation by both shear and longitudinal wave motion. By making appropriate assumptions about domain size, elasticity, and the mode of wave propagation, tissue material properties, such as the shear modulus, can be estimated from the shear wave velocity estimated from MRE [35].

1.3.2 Selected continuum mechanics topics in MRE

This section reviews background and development of the mechanical concepts underlying MRE. These concepts include kinematics, particularly rigid-body displacements and strain, and wave propagation in a linear, homogeneous, and isotropic medium.

Kinematics

The displacement at any point in a deformable body can be due to rigid-body translation and rotation, and deformation. Consider a body with a particular configuration at reference time t_0 that undergoes deformation and changes to a different configuration at time t (Figure 1.5). In this body, a point, P, undergoes a displacement, $\boldsymbol{u}$, so that it arrives at some position: $\boldsymbol{x} = \boldsymbol{X} + \boldsymbol{u}(\boldsymbol{X}, t)$. A neighboring point, Q, is at some infinitesimally close location $\boldsymbol{X} + d\boldsymbol{X}$ at time t_0 and thus arrives at some position: $\boldsymbol{x} + d\boldsymbol{x} = \boldsymbol{X} + d\boldsymbol{X} + \boldsymbol{u}(\boldsymbol{X} + d\boldsymbol{X}, t)$.

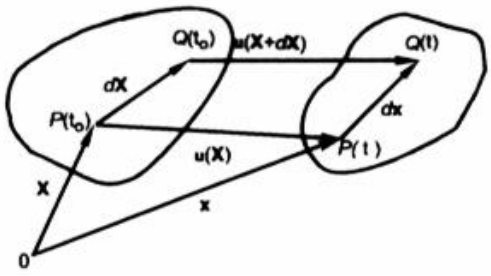

Figure 1.5: Displacement of some body containing two points, P and Q, that undergoes deformation. Reprinted from [40].

By subtracting the position of the deformed configurations for points P and Q, we find an expression for the differential displacement, $d\boldsymbol{x}$**:**

$$d\boldsymbol{x} = d\boldsymbol{X} + \boldsymbol{u}(\boldsymbol{X} + d\boldsymbol{X}, t) - \boldsymbol{u}(\boldsymbol{X}, t) \tag{1.1}$$

Which can be reduced using the definition of a gradient vector function:

$$d\boldsymbol{x} = d\boldsymbol{X} + (\boldsymbol{\nabla u})d\boldsymbol{X} \tag{1.2}$$

where $\boldsymbol{\nabla u}$ is the displacement gradient. A body undergoing rigid rotation produces non-zero displacement gradients regardless of material deformation; thus different measures are required to describe deformation. Equation 1.2 can be rewritten as:

$$d\boldsymbol{x} = (\boldsymbol{I} + \boldsymbol{\nabla u})d\boldsymbol{X} \tag{1.3}$$

$$d\boldsymbol{x} = \boldsymbol{F}d\boldsymbol{X} \tag{1.4}$$

Where $\boldsymbol{I}$ is the identity matrix, and the matrix $\boldsymbol{F} = (\boldsymbol{I} + \boldsymbol{\nabla u})$. In order to decouple deformation in a non-orthogonal $\boldsymbol{F}$ matrix, consider the dot product of equation 1.4 with itself:

$$d\boldsymbol{x} \cdot d\boldsymbol{x} = \boldsymbol{F}d\boldsymbol{X} \cdot \boldsymbol{F}d\boldsymbol{X} = d\boldsymbol{X} \cdot \boldsymbol{F}^{\boldsymbol{T}}\boldsymbol{F}d\boldsymbol{X} \tag{1.5}$$

In the case where $\boldsymbol{F}$ is orthogonal, that is, $\boldsymbol{F^T F = I}$, then $\boldsymbol{F}$ describes only rigid-body displacements:

$$d\boldsymbol{x} \cdot d\boldsymbol{x} = d\boldsymbol{X} \cdot \boldsymbol{F^T F} d\boldsymbol{X} = d\boldsymbol{X} \cdot d\boldsymbol{X} \tag{1.6}$$

In the non-orthogonal case, it can then be shown that:

$$\boldsymbol{F^T F} = (\boldsymbol{I} + \boldsymbol{\nabla u})^T (\boldsymbol{I} + \boldsymbol{\nabla u}) = \boldsymbol{I} + \boldsymbol{\nabla u} + (\boldsymbol{\nabla u})^T + (\boldsymbol{\nabla u})^T \boldsymbol{\nabla u} \tag{1.7}$$

In the case of small displacement gradients, $(\boldsymbol{\nabla u})^T \boldsymbol{\nabla u}$ is a smaller quantity than the components of $\boldsymbol{\nabla u}$, which enables the following approximation:

$$\boldsymbol{F^T F} \approx \boldsymbol{I} + \boldsymbol{\nabla u} + (\boldsymbol{\nabla u})^T \equiv \boldsymbol{I} + 2\boldsymbol{\varepsilon} \tag{1.8}$$

Here, $\boldsymbol{\varepsilon}$ is a tensor describing the changes in lengths resulting from small deformation, thus it is known as infinitesimal strain. This measure can be expressed as:

$$\boldsymbol{\varepsilon} = \frac{1}{2}[(\nabla \mathbf{u})^T + \nabla \boldsymbol{u}] \tag{1.9}$$

In MRE of soft tissue, displacements encoded by phase include both rigid-body motion of the tissue and deformation. Typically, rigid-body motion effects are removed as tissue bulk motion, leaving only tissue deformation, which is often characterized through strain measures [41], [42].

Wave Propagation in an Unbounded and Homogeneous Linear Elastic Regime

The general equation for dynamic equilibrium can be written by expressing force as stresses ($\boldsymbol{\sigma}$) acting on differential sized areas [40]:

$$\rho \frac{\partial^2 \boldsymbol{u}}{\partial t^2} = \nabla \cdot \boldsymbol{\sigma} \tag{1.10}$$

Where ρ is material density and t is time. For a linear, homogeneous, and isotropic medium, stress ($\boldsymbol{\sigma}$) can be described using strain ($\boldsymbol{\varepsilon}$) and the Lamé constants, λ and μ:

$$\boldsymbol{\sigma} = \lambda \boldsymbol{I} \cdot tr(\boldsymbol{\varepsilon}) + 2\mu \boldsymbol{\varepsilon} \tag{1.11}$$

By combining equations 1.10 and 1.11, the following expression can be calculated:

$$\rho \frac{\partial^2 \boldsymbol{u}}{\partial t^2} = \nabla \cdot \left(\lambda \boldsymbol{I} \cdot tr(\boldsymbol{\varepsilon})\right) + \nabla \cdot (2\mu\, \boldsymbol{\varepsilon}) \tag{1.12}$$

To simplify this expression, it is helpful to define the following:

$$tr(\boldsymbol{\varepsilon}) = \nabla \cdot \boldsymbol{u} \tag{1.13}$$

$$\nabla \cdot \boldsymbol{\varepsilon} = \frac{1}{2}(\nabla \cdot (\nabla \cdot \boldsymbol{u}) + (\nabla^2 \boldsymbol{u})) \tag{1.14}$$

By substituting in these definitions, Equation 1.12 can then be simplified:

$$\rho \frac{\partial^2 \boldsymbol{u}}{\partial t^2} = \nabla \cdot (\nabla \cdot \boldsymbol{u})\lambda + 2\mu(\nabla \cdot \boldsymbol{\varepsilon}) \tag{1.15a}$$

$$\Rightarrow \rho \frac{\partial^2 \boldsymbol{u}}{\partial t^2} = \nabla \cdot (\nabla \cdot \boldsymbol{u})\lambda + \mu(\nabla \cdot (\nabla \cdot \boldsymbol{u}) + (\nabla^2 \boldsymbol{u})) \tag{1.15b}$$

$$\Rightarrow \rho \frac{\partial^2 \boldsymbol{u}}{\partial t^2} = \mu \nabla^2 \boldsymbol{u} + (\lambda + \mu)(\nabla \cdot (\nabla \cdot \boldsymbol{u})) \tag{1.16}$$

Equation 1.16 is the equation governing 3D wave propagation in a linear, homogenous, isotropic medium. Here, the compression, $\boldsymbol{u_c}$, and shear, $\boldsymbol{u_s}$, components of wave displacement $\boldsymbol{u}$ can be decoupled through calculation of the divergence $(\nabla \cdot \boldsymbol{u})$ and curl $(\nabla \times \boldsymbol{u})$ of the vector field respectively. Note here that $\nabla \times \boldsymbol{u_c} = 0$ and $\nabla \cdot \boldsymbol{u_s} = 0$.

Many applications in MRE focus on shear deformation, thus the amplitude of curl is often measured and presented to provide an estimate of shear wave motion. For a displacement field that contains contributions from only shear waves, equation 1.16 reduces to:

$$\rho \frac{\partial^2 \boldsymbol{u_s}}{\partial t^2} = \mu \nabla^2 \boldsymbol{u_s} \tag{1.17}$$

Which enables solution of the Lamé constant, μ, which is referred to as the complex shear modulus G^* throughout the rest of this work.

1.3.3 Magnetic resonance elastography of the brain

MRE enables noninvasive assessment of the material and mechanical properties of tissue. As mechanical properties are calculated from displacement fields produced by oscillatory motion, there are multiple modes of data acquisition and analysis [43]. MRE has been applied to a large range of tissues and organs, including the brain.

In MRE of the brain, vibrations are applied to the skull in order to induce shear waves in the brain [44], [45]. Previous studies have demonstrated the ability of MRE to provide local estimates of the mechanical properties of healthy brain tissue [45]–[48], as well as changes in brain material properties due to development, aging, injury, or disease [49]–[52]. MRE is also a valuable tool for parameterizing and validating computational models of TBI [11], [53]. A number of methods exist to estimate material properties in soft tissue, such as local direct inversion (LDI) [54], non-linear inversion (NLI) [55], [56], or local frequency estimation (LFE) [35].

Assessing the material properties of biological tissue is difficult due to how its properties vary with temperature, fluid perfusion, blood pressure, time post-mortem, and metabolic activity. Brain tissue is also viscoelastic, meaning that different actuation frequencies elicit different mechanical responses. Though MRE has shown great promise with *in vivo* tissue material property estimation, substantial variance still exists across the literature [57]. Validation studies of MRE have been performed in animal brain tissue by comparing estimates from MRE *in vivo* with direct mechanical measurements *ex vivo* [58], [59]. These studies offer insight into MRE

accuracy, but substantial difference in methodology and experimental scope may lead to differing conclusions about the mechanical response of brain tissue.

MRE studies of the human brain typically provide intracranial displacement fields along three orthogonal directions according to an anatomical convention, specifically along the right-left (RL) lateral, anterior-posterior (AP), and superior-inferior (SI) anatomical axes. MRE displacement fields are harmonic; shear wave propagation within brain tissue can be shown at different time points along a waveform as shown in Figure 1.6.

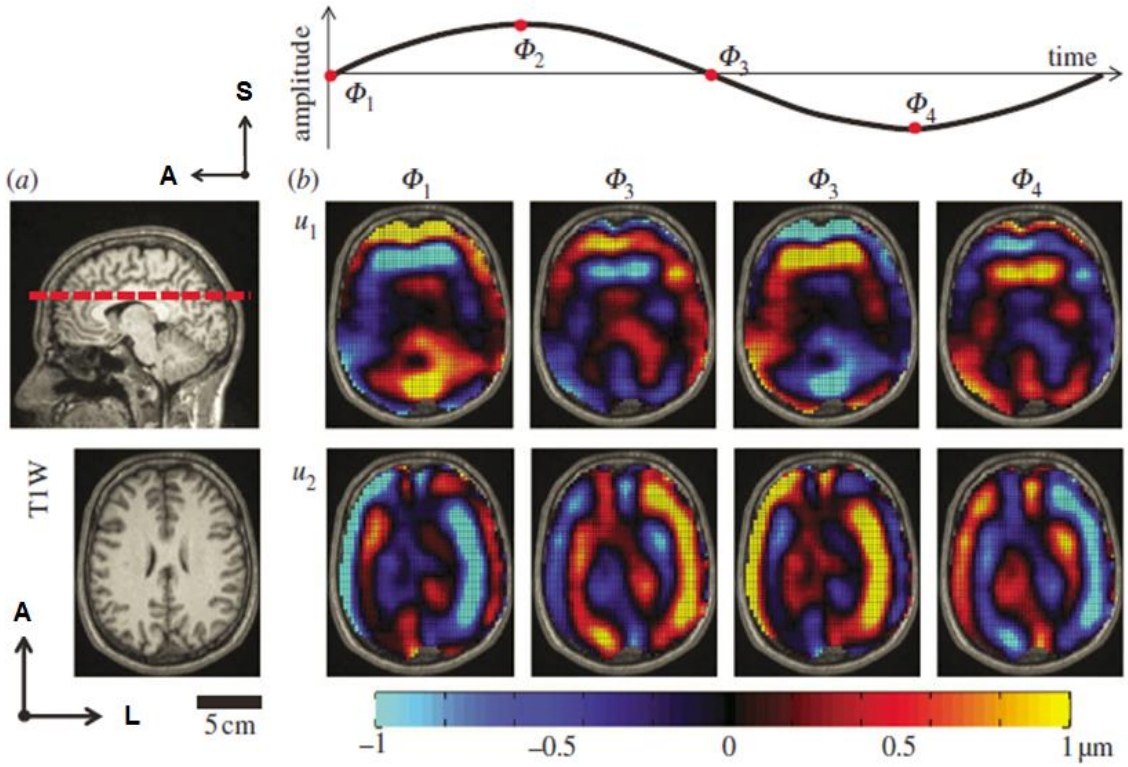

Figure 1.6: Two components of shear wave displacement acquired from MRE are shown at a single slice of brain tissue. a) Anatomical T1-weighted MRI images of an axial slice of brain tissue that includes features such as the corpus callous and lateral ventricles. b) In-plane displacement fields at four points within a single period of actuation show shear wave propagation from the outside of the brain towards the midbrain. Figure reprinted and modified from [45].

While there have been numerous studies analyzing shear wave displacement of brain tissue [44], [45], [48], [56], few studies report rigid-body motion of the brain estimated from MRE. As mentioned above, MRE phase contrast contains contributions from both rigid-body motion and wave motion, however most studies filter out rigid-body motion and consider wave motion in order to analyze strain and material properties. There is great potential for using MRE to improve understanding of relative skull and brain motion if one can accurately characterize skull motion simultaneously with MRE-derived brain tissue displacement.

1.4 Summary

Numerous studies have attempted to characterize relative skull and brain motion; however recent advances in imaging technology, specifically MRE, may enable assessment of simultaneous skull and brain motion *in vivo*. Though computational models of TBI have improved their technical scope and anatomical accuracy, experimental measurements of brain biomechanics are essential for parameterization and validation. Specifically, noninvasive characterization of the mechanical contributions of the skull-brain interface during skull motion is desirable.

Multiple studies have demonstrated that MRE of the brain can be used to provide reliable estimates of mechanical properties; however there is also scope for using MRE to characterize full 3D brain kinematics. In particular, we can visualize both rigid-body motion and deformation of the brain in response to skull excitation. Further, computational models of TBI need better representations of how a soft, compliant interface and stiff dural membranes alter motion

transmission from the skull to the brain. Continued work on these questions is important for the understanding of TBI and the consequent ability to predict and prevent brain injury.

1.5 Specific Aims and Dissertation Outline

1.5.1 Specific aims

In order to provide more accurate parameters for TBI modeling, I have developed and applied new imaging and modeling techniques for measuring skull and scalp motion. This dissertation describes progress on three specific aims:

Aim 1: Relate 3D skull kinematics to brain tissue deformation by comparing (i) direct mechanical characterization of skull motion by an array of tri-axial accelerometers with (ii) brain displacement estimates from MRE.

Aim 2: Design an acquisition and analysis protocol capable of estimating simultaneous scalp and brain displacements using MRE.

Aim 3: Model the mechanical and material properties of the skull-brain interface using simplified (cylindrical) and anatomically-accurate cranial phantoms.

1.5.2 Dissertation outline

The current chapter provides motivation and background for a study of skull and brain motion. Chapter 2 provides an overview of methodology, including estimation of rigid-body kinematics from an array of accelerometers, and magnetic resonance imaging methods.

MRE estimates of brain tissue displacement are compared with accelerometer-derived estimates of skull motion in Chapter 3. These *in vivo* estimates of relative skull and brain motion are compared to analogous measurements of motion in a cylindrical, glycerol-gelatin phantom.

A modified MRE data acquisition process for capturing simultaneous scalp, skull, and brain motion is presented in Chapter 4. This chapter explores using MRE estimates of scalp motion as a surrogate for estimating skull motion. Using methods developed in Aim 1, scalp and brain displacements estimated from MRE are compared with skull motion estimated from accelerometers.

Chapter 5 outlines the creation and testing of cylindrical phantoms and cranial phantoms of increasing complexity. The goal of these models is to characterize both interfacial and membranous properties and decouple their effects to better assess the mechanisms of transmission and attenuation at the skull-brain interface.

The general conclusions of this study, experimental limitations, and future work are discussed in Chapter 6.

Chapter 2: General Methodology: Theoretical Framework, Imaging, and Data Analysis

2.1 Overview

In this chapter, general experimental methods used in Chapters 3-5 are developed. These methods include: estimation of rigid-body motion from accelerometers, estimation of displacement fields from MRE phase, and MRE sequence timing and synchronization. Other topics include how three-dimensional (3D) harmonic motion can be described by elliptical trajectories and how accelerometer motion reconstruction was tested and validated.

2.2 Rigid-body Kinematics Estimated from Tri-axial Accelerometers

2.2.1 Three-dimensional harmonic motion described by elliptical trajectories

Consider a complex vector $\boldsymbol{u}_0 = (u_0, v_0, w_0)$ describing 3D harmonic motion at a frequency, Ω: $\boldsymbol{u}(t) = \mathrm{Re}[\boldsymbol{u}_0 \mathrm{e}^{i\Omega t}]$. The components of this vector can be described by:

$$u_0 = \mathrm{r}_1 \mathrm{e}^{i\psi_1}, \tag{2.1a}$$

$$v_0 = \mathrm{r}_2 \mathrm{e}^{i\psi_2}, \tag{2.1b}$$

$$w_0 = \mathrm{r}_3 \mathrm{e}^{i\psi_3}, \tag{2.1c}$$

where r_n is the amplitude and ψ_n is the phase of each component. In harmonic motion, the trajectory shape is determined by the relative amplitudes and phases of these components. When all three components are exactly in phase, that is $\psi_1 = \psi_2 = \psi_3$, the trajectory collapses to a straight line (Figure 2.1a). If the three components have different temporal phase, however, then the resulting trajectory is an ellipse (Figure 2.1b). For this analysis, I determined the relative spatial orientation of two elliptical trajectories by finding the spatial angle between the vectors normal to the plane of each ellipse (Figure 2.1c). The normal vectors are calculated from the cross product of the real and imaginary parts of the coefficient vectors.

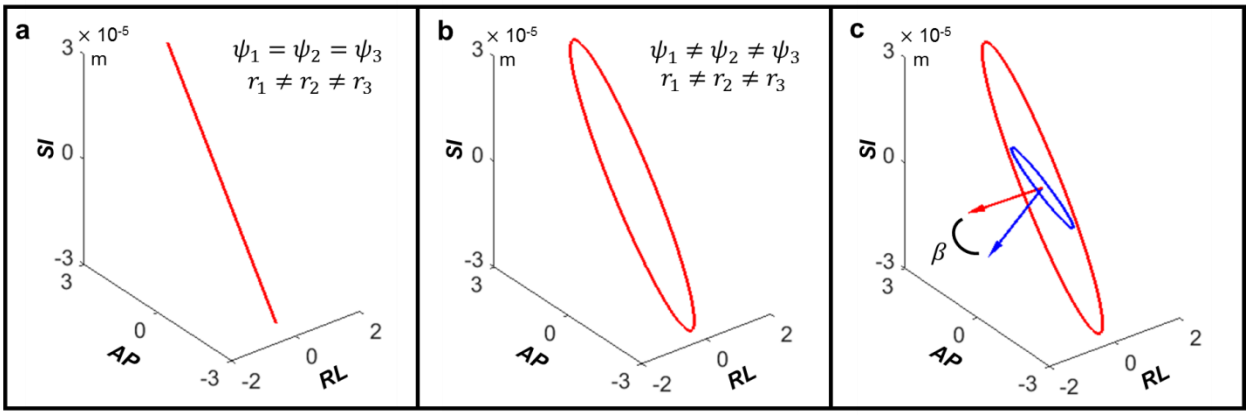

Figure 2.1: During 3D harmonic motion, the trajectory of each point depends on the amplitude and phase of each component. A) The trajectory is a straight line when all three components have the same temporal phase, ψ, even if the component magnitudes, r_n, are different B) The trajectory becomes an ellipse when the three components have different temporal phase. C) The spatial angle, β, between the vectors normal to the plane of each ellipse (arrows) was used to describe the difference in spatial orientation of motion (β = 0.9 rad in this example).

2.2.2 Mouth guard array (MGA) design and tri-axial accelerometer data collection

In order to characterize skull motion during MRE, I designed an accelerometer data collection system capable of acquiring and processing signals acquired from three tri-axial, MRI-safe accelerometers (TSD109C2-MRI, BIOPAC©, Goleta, CA). The components used for this system are described in Appendix A. Accelerometer data was collected assuming a right-handed coordinate system with three orthogonal axes: right-left (RL), anterior-posterior (AP), and superior-inferior (SI). For these three directions, the right, anterior, and superior directions were chosen to be positive, giving us a right-anterior-superior (RAS) coordinate system. During accelerometer data collection, the accelerometers are oriented so that the x, y, and z signal components map in the following way (first letter indicates positive direction): $x \rightarrow LR, y \rightarrow SI, z \rightarrow AP$.

To mount the accelerometers during an MRE experiment, I designed a 3D printed interface that could be embedded within a commercial sports mouth guard (ShockDoctor® Low Profile Lip Guard). This accelerometer mouth-guard array (MGA) was designed to allow for rigid placement of the accelerometers and easy retrieval from the subject during the scanning protocol (Figure 2.2). To accomplish this, the MGA was designed to be low profile, meaning it would not protrude too far in the anterior direction and touch the head coil.

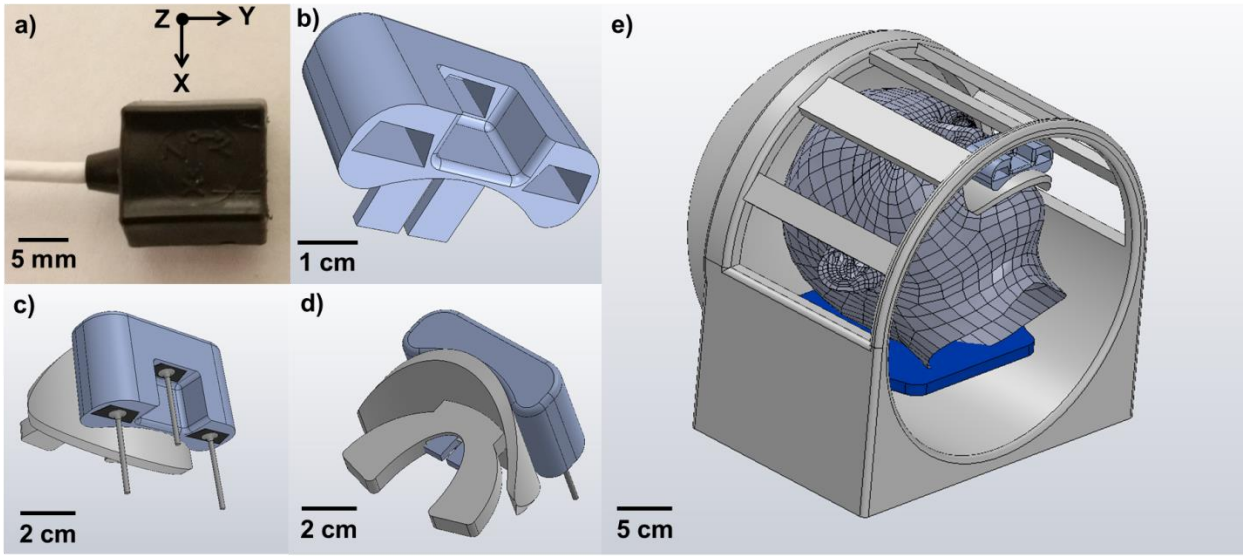

Figure 2.2: Accelerometer mouth guard array (MGA) design and implementation A) Tri-axial accelerometer with positive directions labeled. B) 3D printed MGA has slots for three tri-axial accelerometers and two protrusions to fit into the ventilation shafts of the commercial mouth guard. C) MGA embedded in commercial mouth guard with accelerometers positioned in each of the three slots. D) Rear view of MGA and commercial mouth guard to show MGA protrusions through the ventilation shaft. E) Rendering of subject biting down on MGA while inside head coil. MGA is designed to fit within the head coil and be retrieved without moving the subject or removing the head coil.

Accelerometer data is collected at 10,000 samples/sec over a window ranging from 35-45 seconds depending on the length of the scan. The accelerometer signals can contain noise from the MRE sequence. To remove noise, the accelerometer signal is bandpass filtered using a range of 5-500 Hz and median filtered with a window size of 51 elements (MATLAB© *medfilt1* command). Some artifacts due to the MRE sequence are useful to sample, however, such as the RF pulse and inversion pulse. These artifacts are later used as landmarks to synchronize accelerometer and MRE data (Section 2.3.3).

2.2.3 Skull kinematics estimation from tri-axial accelerometers

Skull motion during MRE at 50 Hz is well approximated as rigid-body motion [60]; standard 3D kinematic equations for rigid-body acceleration (Eq. 2.2a-c) are used [61]. Here, $\boldsymbol{a}$ is linear acceleration, $\boldsymbol{\alpha}$ is angular acceleration, $\boldsymbol{r}$ defines the distance between some point and the skull origin (approximated as the posterior clinoid process), and $\boldsymbol{\omega}$ is angular velocity. Each of these vectors consists of three components, denoted as x, y, and z, to represent the right-left (RL), anterior-posterior (AP), and superior-inferior (SI) directions. Thus, (a_x^O,a_y^O, a_z^O) are, respectively, the RL, AP, and SI linear accelerations of the skull origin; (ω_x, ω_y, ω_z) are rates of rotation (angular velocity) about the RL, AP, and SI directions, respectively; and (α_x, α_y, α_z) are the components of angular acceleration. (a_x,a_y, a_z) are the components of linear acceleration of a point whose position, measured from the skull origin, is (r_x, r_y, r_z). The right-hand side of these equations will contain 9 unknowns (3 components of motion for each of $\boldsymbol{a}$, $\boldsymbol{\alpha}$, and $\boldsymbol{\omega}$ at the skull origin) which can be solved using the known values of linear acceleration at the positions of the tri-axial accelerometers.

$$a_x = a_x^O + (\alpha_y r_z - \alpha_z r_y) + (\omega_x(\omega_y r_y + \omega_z r_z) - r_x(\omega_y^2 + \omega_z^2)) \quad (2.2a)$$

$$a_y = a_y^O + (\alpha_z r_x - \alpha_x r_z) + (\omega_y(\omega_z r_z + \omega_x r_x) - r_y(\omega_x^2 + \omega_z^2)) \quad (2.2b)$$

$$a_z = a_z^O + (\alpha_x r_y - \alpha_y r_x) + (\omega_z(\omega_x r_x + \omega_y r_y) - r_z(\omega_x^2 + \omega_y^2)) \quad (2.2c)$$

To provide additional information, rigid-body velocity expressions (Eq. 2.3a-c) may also be used to estimate $\boldsymbol{\omega}$ [29, 30]. Velocity ($\boldsymbol{v}$) at each accelerometer position can be estimated through integration of the acceleration signal.

$$v_x = v_x^O + \omega_y r_z - \omega_z r_y \tag{2.3a}$$

$$v_y = v_y^O + \omega_z r_x - \omega_x r_z \tag{2.3b}$$

$$v_z = v_z^O + \omega_x r_y - \omega_y r_x \tag{2.3c}$$

The acceleration signals are expressed as Fourier coefficients (sum of sinusoids) j, providing the ability to integrate acceleration in the frequency domain. Equations 2.4a-c demonstrate how velocity and displacement ($\boldsymbol{u}$) are calculated. Here Ω is angular frequency (rad/s), φ is phase shift, D is amplitude, t is time, the subscript j denotes the Fourier harmonic, and the subscript q refers to each of the three Cartesian components of motion.

$$a_q = \sum_j D_{qj} sin(\Omega_j t + \varphi_j) \tag{2.4a}$$

$$\Rightarrow v_q = -\sum_j \frac{D_{qj}}{\Omega_j} cos(\Omega_j t + \varphi_j) \tag{2.4b}$$

$$\Rightarrow u_q = -\sum_j \frac{D_{qj}}{\Omega_j^2} sin(\Omega_j t + \varphi_j) \tag{2.4c}$$

The components of displacement at a point on the skull at position $\boldsymbol{r}$ with respect to the origin can then be reconstructed by defining three components of translation ($\bar{u}_x^O$, $\bar{u}_y^O$, and $\bar{u}_z^O$) and three components of rotation ($\theta_x, \theta_y,$ and θ_z) about the skull origin and solving Equations 2.5a-c:

$$\bar{u}_x = \bar{u}_x^O + \theta_y r_z - \theta_z r_y \quad (2.5a)$$

$$\bar{u}_y = \bar{u}_y^O + \theta_z r_x - \theta_x r_z \quad (2.5b)$$

$$\bar{u}_z = \bar{u}_z^O + \theta_x r_y - \theta_y r_x \quad (2.5c)$$

2.2.4 Validation of motion reconstruction from tri-axial accelerometer data

To test the accuracy of motion reconstruction, I compared accelerations reconstructed from measurements with the accelerometer array to simultaneous acceleration data measured with an independent sensor, during known translational and rotational motions (Figure 2.3). Oscillatory rotational motion was generated by a Torsional Plant 205 (ECP©, Bell Canyon, CA) at a frequency of 10 Hz while translational motion was generated with an Electro-seis 113 Long Stroke Shaker (APS Dynamics ©, San Juan Capistrano, CA) at a frequency of 50 Hz. The MGA was mounted on the moving section of each device. An additional accelerometer was placed on each device to serve as a reference. For rotational experiments, the MGA was oriented so that the motion corresponded to rotation about the RL axis. For linear motion the MGA was oriented so translation was in the AP direction. The normalized root-mean-square error (NRMSE) was calculated from the RMS difference between the acceleration reconstructed from the MGA and the recorded signal from the reference accelerometer, normalized by the reference acceleration

magnitude. In the rotational experiment, NRMSE was 0.04 in the AP direction and 0.02 in the SI direction. In the translational experiment, NRMSE was 0.04 in the AP direction and 0.08 in the SI direction. Noise, non-rigid motion, and nonlinearity can contribute to reconstruction error; these are more apparent in low-amplitude harmonic signal, such as in the translational experiment SI motion. However, since the SI component is a small fraction of the acceleration magnitude, its contribution to the overall error is small.

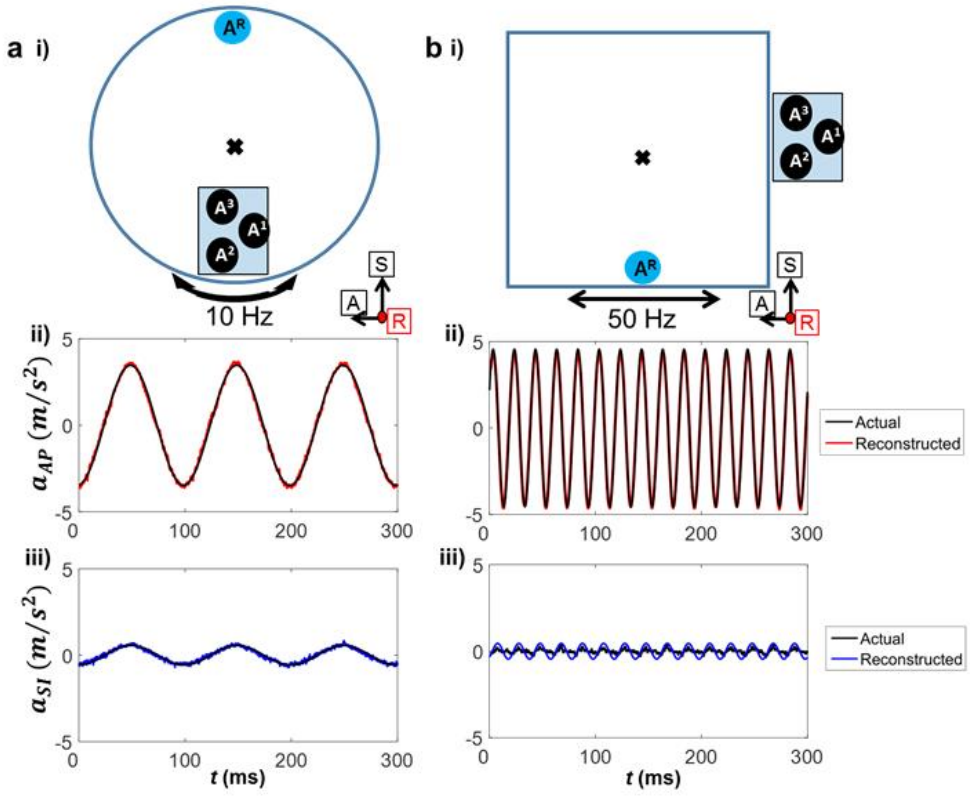

Figure 2.3: Validation of accelerometer motion reconstruction using constrained angular and linear motion. (a)(i) The accelerometer MGA was placed on the bottom disk of a torsional vibration demonstration system (ECP 205 Torsional Plant, ECP©, Bell Canyon, CA) and used to reconstruct in-plane motion at the location of a fourth reference accelerometer placed at the top of the platform. Oscillation frequency: 10 Hz. (a)(ii) Normalized reconstruction RMS error in the AP direction, NRMSE=0.04; (a)(iii) normalized RMS error in the SI direction, NRMSE=0.02. (b)(i) A horizontal shaker (APS Electro-seis 113 Long Stroke Shaker, APS Dynamics ©, San Juan Capistrano, CA) was used to validate translational motion reconstruction. The MGA was placed on the posterior of the platform while the reference accelerometer was placed on the side. Oscillation frequency: 50 Hz. (b)(ii) AP direction NRMSE=0.04, (b)(iii) SI direction NRMSE=0.08.

2.3 Imaging Methods and Analysis

2.3.1 Estimation of harmonic displacement from magnetic resonance elastography

In MRE, external vibrations are applied in order to induce shear waves throughout soft tissue [44], [51], [62]. These shear waves are observed using MRE imaging sequences with motion-encoding gradients that oscillate at the vibration frequency, producing phase contrast images proportional to displacement [34], [63]. When oscillating motion-encoding gradients of constant amplitude, frequency, and duration are applied in three orthogonal directions, a vector of motion-induced phase is acquired. The displacement at these voxels is proportional to the phase accumulated from application of the motion-encoding gradients [34], [63]. In this work, two MRE sequences are used: a 2D spiral MRE sequence with 2 mm voxel resolution [56] and an echo-planar imaging MRE sequence with 3 mm voxel resolution. The pulse sequence diagram for the spiral 2D MRE sequence is shown in Figure 2.4.

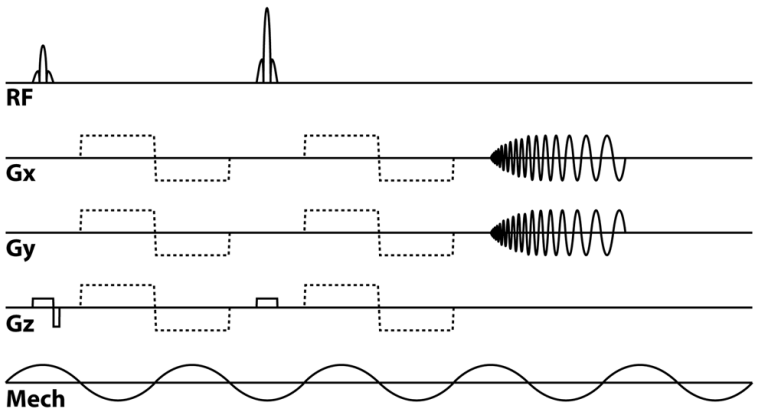

Figure 2.4: Pulse sequence diagram for the spiral 2D MRE sequence. Bilateral motion-encoding gradients are applied sequentially along three orthogonal directions to encode harmonic motion. Variable density, multi-shot spiral readout gradients are applied to sample k-space and reduce distortion. Reprinted from [56].

The MRE phase contrast, Φ, for time-varying (square wave) motion-encoding gradients, $\boldsymbol{G}(t)$, and harmonic displacement field $\boldsymbol{u}(\boldsymbol{r},t)$ is:

$$\Phi = N\gamma \int_0^T \boldsymbol{G}(t) \cdot \boldsymbol{u}(\boldsymbol{r},t)dt \tag{2.6}$$

where γ is the gyromagnetic ratio of ^{1}H, T is the period, N is the number of motion-encoding gradients, and $\boldsymbol{u}(\boldsymbol{r},t) = \boldsymbol{u}_o e^{i(\Omega t-\psi)}$ is the vector of displacement at reference position $\boldsymbol{r}$ and time t. Here, Ω is angular frequency (rad/s) and $\psi = \psi(\boldsymbol{r})$ is the temporal phase shift of the displacement at that voxel.

Evaluation of this integral yields an expression for the MRE phase contrast Φ, including a temporal phase shift relative to the refocusing pulse:

$$\Phi = \frac{4N\gamma G e^{-i\left(\psi-\frac{\pi}{2}\right)}u_G}{\Omega} \tag{2.7}$$

Here, u_G is the component of $\boldsymbol{u}_o$ in the direction of the gradient: $u_G = \boldsymbol{G} \cdot \boldsymbol{u}_o/G$ and G is the motion encoding gradient strength. The sensitivity of the MRE sequence can be doubled by computing the phase difference between acquisitions using positively (P) and negatively (N) polarized motion-encoding gradients.

$$\Phi_T = \Phi_P - \Phi_N = 2\Phi_P = \frac{8N\gamma G e^{-i\left(\psi-\frac{\pi}{2}\right)}u_G}{\Omega} \tag{2.8}$$

The magnitudes of the total (reported) phase Φ_T and of the displacement u_G are linearly related to each other by the ratio $u_G / \Phi_T = \Omega/(8N\gamma G)$.

2.3.2 Unwrapping MRE phase contrast

MRE phase contrast (Φ) is originally constrained to the principal range $(-\pi, \pi]$, which can cause wrapping and complicate recovery of the original amplitude. For example, if the amplitude of tissue displacement is 30 microns at 50 Hz, a bilaterally applied MEG with strength of 7 mT/m will result in phase amplitude of 2.87 radians. If the MEG strength is 10 mT/m, the phase amplitude will increase to 4.09 radians, which will appear wrapped in the resulting image. In addition to phase wrapping in space (which is already a challenging problem [35, 36]), the harmonic data may also be wrapped in time. In cases where the wave motion is much smaller in amplitude than the rigid-body motion (e.g. MRE experiments in this work where external head excitation causes brain tissue vibration), this problem is particularly challenging as all voxels in a single phase offset may be wrapped.

As an example of the need for temporal unwrapping, MRE data from a single human subject is shown at MEG strengths of 4, 7, 10, and 25.9 mT/m in Figure 2.5. Unwrapping in time is difficult to perform due to the very coarse sampling: 8 points per period. Therefore, to accurately recover the harmonic time series, I used a custom temporal post-processing algorithm following initial spatial unwrapping of 3D volumes with a widely-used, third-party algorithm (FSL

PRELUDE [32]). The temporal post-processing algorithm consisted of tabulating all possible permutations of the motion-encoded phase at a selected voxel, with a value of $0, -2\pi,$ or 2π added at each time point. This resulted in 3^8, or 6561 permutations. The 8-point FFT of each permutation was calculated, and the permutation that contained the highest fraction of power at the fundamental frequency FFT, was then selected as the temporal unwrapping solution.

As Figure 2.5 shows, the rigid-body motion is homogeneous across the FOV, meaning that the same unwrapping scheme was used for each voxel. MRE data was then processed at lower MEGS to view an unwrapped AP phase contrast waveform in the same subject. Data from this protocol confirmed that MRE phase contrast was proportional to the strength of the motion encoding gradients. The MRE phase waveform acquired at lower MEGS was used as a template to check the unwrapped solution for the waveform at higher MEGS.

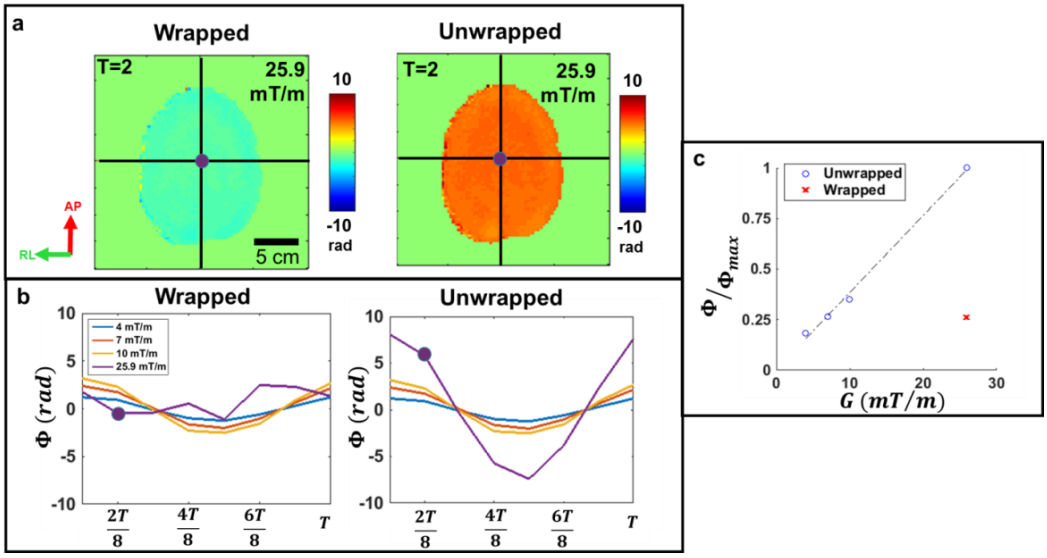

Figure 2.5: Comparison of MRE phase contrast (Φ) captured by different motion-encoding gradient strengths (MEGS). a) Visualization of the wrapped and unwrapped phase contrast encoded by the maximum MEGS of 25.9 mT/m at time point 2. b) Comparison of wrapped and unwrapped MRE phase contrast at a single voxel (purple circle) between EPI-MRE trials at 4, 7, 10, and 25.9 mT/m. c) Line plot of MRE phase contrast, normalized to the unwrapped phase contrast at 25.9 mT/m. Unwrapped data points were fitted to a linear model (R^2 = 0.99).

In future studies, it is recommended to continue performing spatial unwrapping of high MEG strength MRE data using FSL Prelude followed by temporal unwrapping guided by comparison to lower MEGS MRE data.

2.3.3 Synchronizing accelerometer signals with MRE data acquisition

When accelerometer data was acquired during MRE imaging, artifacts, such as abrupt deflections, in the accelerometer signal trace corresponded with landmarks in the MRE sequence such as the refocusing pulse and spiral gradients in the 2D MRE spiral sequence (Figure 2.6). To relate the phases of skull motion and brain motion, the center of the 180° refocusing pulse was chosen as a common temporal landmark for synchronizing the accelerometer and MRE signals. The relative phase of the accelerometer recordings was determined from the FFT of the

accelerometer time series, setting the initial time point ($t = 0$) at the center of the refocusing pulse. The relative phase shift of the MRE signal was found directly from the FFT of the time series of MRE phase contrast, which is already referenced to the center of the refocusing pulse with a phase shift of $\pi/2$ radians (5 ms at 50 Hz). Similar methods are used for other MRE sequences such as the EPI sequence, which also uses the same number of bilaterally applied motion encoding gradients as the spiral 2D sequence, but has slightly different timing relative to the refocusing pulse.

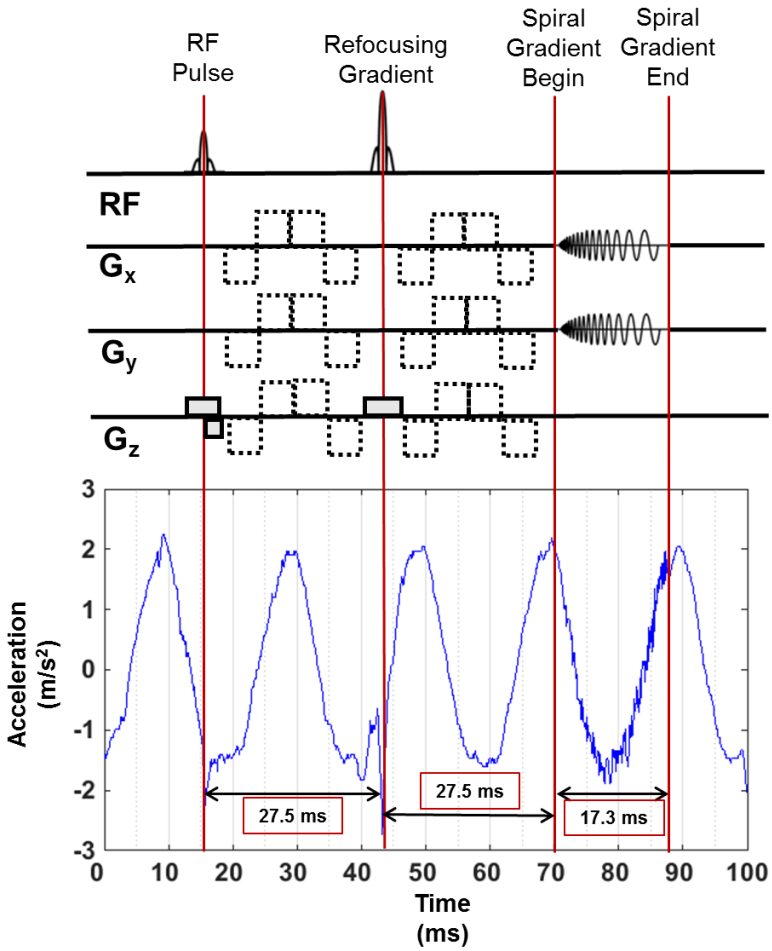

Figure 2.6: Artifact in the accelerometer trace can be used to locate landmarks in the MR pulse sequence, such as the RF pulse, refocusing gradient, and spiral gradients. A 2D spiral MRE pulse sequence diagram is shown [20]. Bipolar motion-encoding gradients (dashed boxes) are applied sequentially.

Chapter 3:Comparison of 3D Skull Kinematics to Brain Tissue Deformation *in vivo*

3.1 Overview

In the study presented in this chapter, displacements of points in the skull were reconstructed using data from an array of MRI-safe accelerometers and compared to displacements of neighboring material points in brain tissue, estimated from MRE measurements. Comparison of the relative amplitudes, directions, and temporal phases of harmonic motion in the skulls and brains of six human subjects shows that the skull-brain interface significantly attenuates and delays transmission of motion from skull to brain. In contrast, in a cylindrical gelatin "phantom", displacements of the rigid case (reconstructed from accelerometer data) were transmitted to the gelatin inside (estimated from MRE data) with little attenuation or phase lag.

The material presented in this chapter is published in the American Society of Mechanical Engineering (ASME) Journal of Biomechanical Engineering [64]. An erratum updating some of the published data is forthcoming. Some figures printed in this dissertation may not match currently published data.

3.2 Methods

3.2.1 MRE imaging procedures and instrumentation

MRE imaging of six adult, male human subjects and a cylindrical gelatin phantom was performed on Siemens Trio® 3T MRI scanners located at the Beckman Institute at University of Illinois in Urbana-Champaign and the Center for Clinical Imaging Research at Washington University in St. Louis. All studies were approved by the Institutional Review Board (IRB) of the respective institutions.

Subjects lay supine with their heads centered in a Siemens 12 channel head coil. Skull vibrations were induced at a frequency of 50 Hz through a commercially available mechanical actuator (Resoundant^{TM}, Rochester, MN) using a pillow-like actuator (Mayo Clinic, Rochester, MN) positioned on the back of the subject's head at the skull occipital protuberance [49]. The head rests on the pillow, and is stabilized by pads placed laterally. Skull vibrations were induced at 18% Resoundant^{TM} amplitude. Three-dimensional skull kinematics were measured using three MRI safe tri-axial accelerometers (TSD109C2-MRI, BIOPAC©, Goleta, CA) embedded in an array constructed from a commercial sports mouth guard and 3D-printed interface (Figure 3.1). The relative positions of the MGA and the pillow actuator were identified with vitamin E capsules that appeared with high signal in the field of view of T_1-weighted MR images. Subject brain volume (1378 ± 192 cm^3) was calculated through segmentation of gray and white matter tracts in T_1-weighted MRI data [65].

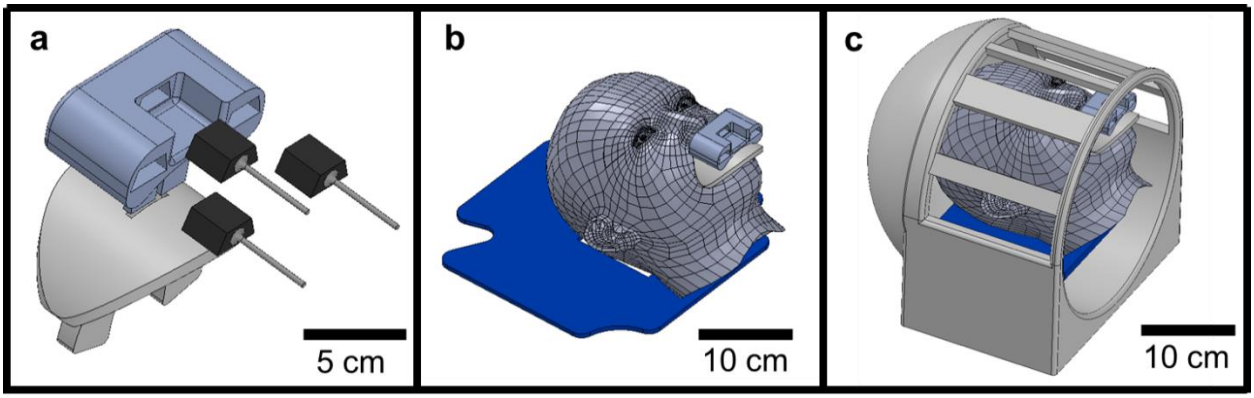

Figure 3.1: Schematic illustration of the accelerometer mouth guard array (MGA) and its positioning for a human subject. (a) Spacing of the three accelerometers within the MGA. (b) The subject bites down firmly on the mouth guard while lying supine on the pillow actuator. (c) 3D rendering of the relative placement of the subject, pillow actuator, and MGA inside the head coil.

A multishot spiral MRE sequence with 2 mm isotropic voxels was used to measure brain tissue displacement, which is encoded as phase in the resulting MR images [56]. Imaging parameters included 26 mT/m motion-encoding gradient strength, 6 k-space interleaves, 8 phase offsets, and twenty axial slice acquisition in the region of the corpus callosum (Figure 3.2), with an image volume of 240 mm x 240 mm x 40 mm and a scan duration of approximately 11 minutes. While MRI-safe, the accelerometers induced imaging artifacts, thus a single slice scan with duration of approximately 36 seconds was performed in order to record skull acceleration during the MRE sequence. After this scan, The MGA was removed while the subject's head remained in the head coil and the full, 20 slice MRE scan was performed.

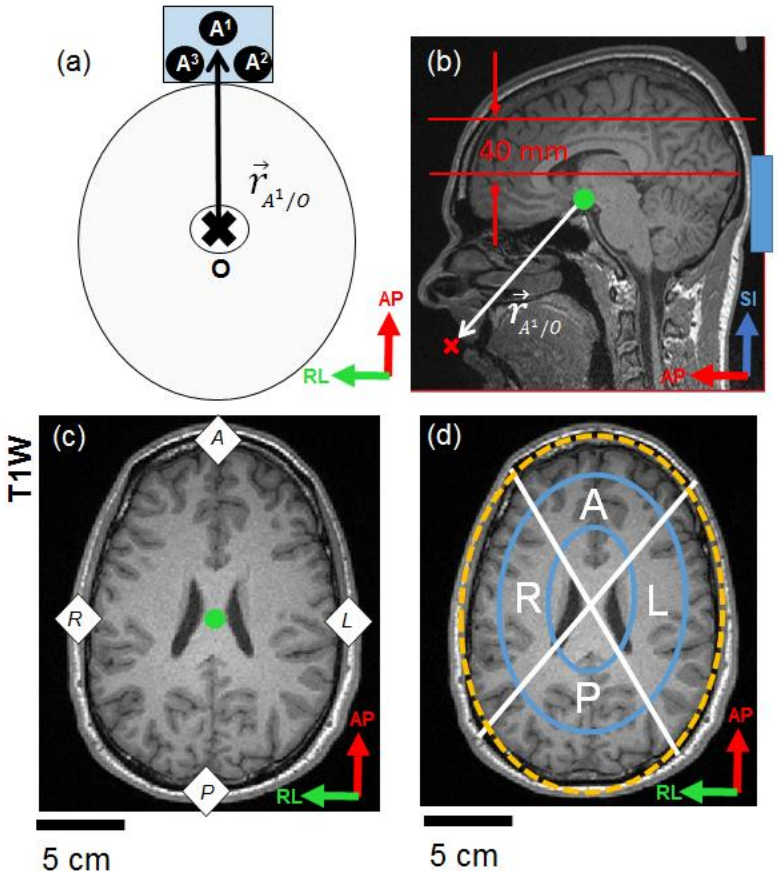

Figure 3.2: 3D kinematics are estimated at four points around the skull. (a) Schematic diagram of the accelerometer positions relative to the origin. (b) Sagittal MR image showing the relative distance, $r_{A^1/O}$, between the skull origin, approximated as the posterior clinoid process (green circle), and accelerometer 1 (A^1) within the MGA. The relative location of the pillow actuator is outlined as the blue rectangle. The MRE acquisition planes, encompassing twenty slices at 2 mm voxel resolution, are outlined in red. (c) T1-weighted images are used to determine the position of the four reconstruction points Anterior (A), Right (R), Left (L), and Posterior (P) relative to the origin. (d) Regional analysis of MRE measurements is performed by segmenting the MRE images into three rings and four quadrants. A mask based on image amplitude was applied to isolate brain tissue from the skull (orange oval).

To provide an MR phantom with simpler properties that could be used to validate techniques and compare behavior, a cylindrical phantom (~13 cm long and 13 cm in diameter) was fabricated from a plastic case filled with 1.65 L (1.81 kg) of a gelatin-glycerol-water solution (4% gelatin, 48% glycerol and 48% water by weight [66]). For brevity, this mixture is referred to as gelatin. The gelatin phantom was refrigerated for a minimum of 12 hours to allow the gelatin to set. The

gelatin phantom was equilibrated for 3 hours at room temperature before imaging. The storage modulus, or real part of the viscoelastic shear modulus, of gelatin samples was 1.8 kPa, as measured with dynamic shear testing at 50 Hz [66]. A 3D printed holder was used to rigidly attach the MGA to the outer surface of the gelatin phantom's cylindrical plastic case. The gelatin phantom was positioned in the head coil, stabilized laterally with pads, and vibrated using the pillow actuator at 50 Hz. The lower weight of the gelatin phantom, 1.8 kg compared to approximately 3.5-4.5 kg for the human skull [30], necessitated a Resoundant^{TM} actuation amplitude of 3% to minimize phase wrapping of the MRE images.

The experimental protocol thus involved the following steps:

1) Position subject outside the scanner bore with the accelerometer MGA.

2) Record skull accelerations in response to the pillow actuator without the spiral MRE sequence running.

3) Move subject into the scanner bore and acquire accelerometer data from a single-slice MRE sequence.

4) Remove the MGA without removing the subject's head from the coil.

5) Run anatomical scan (T_1-weighted: 3D MPRAGE, 0.9 mm isotropic voxels) and 20-slice spiral MRE sequence.

This protocol enabled comparison of skull dynamics (reconstructed from accelerometer data) and brain tissue displacement (estimated from MRE measurements) in the same subject.

3.2.2 Analysis of MRE displacement measurements

As noted previously, MRE phase contrast includes the effects of oscillatory rigid-body motion, longitudinal wave motion, and shear wave motion. During imaging, oscillatory, rigid-body motion can be described through both translation in the x, y, and z directions along with rotation about each of those axes. Additionally, when the amplitude of motion is large, motion-induced phase wrapping may occur. This was commonly seen in the phase-encoded anterior-posterior component of motion. Wrapped phase was spatially unwrapped using FSL PRELUDE [67] and temporally unwrapped through implementation of FFT power analysis of unwrapped phase solutions.

After unwrapping the MRE phase data, the three complex displacement components at each voxel were obtained by converting phase to displacement and extracting the first harmonic using a temporal Fourier transform. Components of rigid-body displacement ($\bar{\boldsymbol{u}}$) were estimated for comparison with skull motion reconstructed from the accelerometers. A set of three rotation components ($\theta_x, \theta_y,$ and θ_z) and three translation components ($\bar{u}_x^O$, $\bar{u}_y^O$, and $\bar{u}_z^O$) about the brain origin were used to describe 3D, rigid-body displacement in the brain at each voxel location (denoted by position $\boldsymbol{r}$ with respect to the brain origin).

These complex components were solved by least squares fitting of the total displacement (estimated from MRE data) at all voxels within the brain to the same model of rigid-body displacement used for capturing skull motion in Section 2.2.3. These equations are reprinted here for convenience (Eq.3.1a-c):

$$\bar{u}_x = \bar{u}_x^O + \theta_y r_z - \theta_z r_y \quad (3.1a)$$

$$\bar{u}_y = \bar{u}_y^O + \theta_z r_x - \theta_x r_z \quad (3.1b)$$

$$\bar{u}_z = \bar{u}_z^O + \theta_x r_y - \theta_y r_x \quad (3.1c)$$

The contribution of shear and longitudinal waves to the displacement field ($\tilde{\boldsymbol{u}}$) was estimated by removing rigid-body motion from the total displacement field estimate. In addition, in an isotropic, uniform, elastic or viscoelastic material, the curl of the displacement field contains only contributions of shear waves. The curl ($\boldsymbol{\Gamma}$) was estimated through local polynomial fitting and differentiation of the displacement field to provide a separate estimate of the contribution of shear waves. Wave motion for both human subjects and the gelatin phantom are reported in terms of both wave displacement and curl. Strain magnitudes resulting from wave propagation are reported as octahedral shear strain (ε_s) [68]. Octahedral shear strain, ε_s, can be calculated from the components of the strain tensor ε:

$$\varepsilon_s = \frac{2}{3}\sqrt{(\varepsilon_{xx} - \varepsilon_{yy})^2 + (\varepsilon_{xx} - \varepsilon_{zz})^2 + (\varepsilon_{yy} - \varepsilon_{zz})^2 + 6\,(\varepsilon_{xy}^2 + \varepsilon_{xz}^2 + \varepsilon_{yz}^2)^2} \quad (3.2)$$

Octahedral shear strain is a measure of the maximum value of shear strain on any plane. For comparison with estimates of strain and curl (non-dimensional measures of displacement per unit length), the displacement of the case or skull was normalized by the radius of the case or the major semi-axis of the skull.

To characterize brain tissue displacements in different regions and compare them with skull motion at specific locations, MRE measurements were separated into twelve regions of interest (ROI) including three shells (outer, middle, and inner) and four quadrants (anterior, A; right, R; left, L; and posterior, P) (Figure 3.2d). MRE measurements in the gelatin phantom were separated similarly into 12 ROIs: four corresponding A, P, R, and L quadrants and 3 shells.

3.2.3 Comparison of skull and brain displacements

Displacements at four discrete points: anterior (A) near the forehead, right (R) by the right temple, left (L) by the left temple, and posterior (P) near the skull occipital protuberance (Figure 3.2a, 3.2c) were reconstructed from acceleration data. Reconstruction points and the skull origin were located from T_1-weighted anatomical scans (Figure 3.2b). On the gelatin phantom, anterior, right, left, and posterior reconstruction points were similarly chosen as central points along each cylinder edge.

Estimates of skull displacement at four material points in the skull (reconstructed from accelerometer measurements) were compared to analogous estimates of displacement at

neighboring material points in the brain (estimated from MRE measurements). In general harmonic motion, where the three components of motion are not exactly in phase, the 3D trajectory of each point in the brain and skull is an ellipse, represented as a complex coefficient vector, $\boldsymbol{u}_0$, multiplied by a complex exponential in time, $\boldsymbol{u}(t) = \boldsymbol{u}_0 \exp(i\Omega t)$. The elliptical trajectories of material points in skull and brain tissue were described by their relative amplitudes, spatial orientations, and temporal phase. The amplitude of each elliptical trajectory is reported as its mean radius: the circumference of the corresponding ellipse divided by 2π.

Consider two 3D complex coefficient vectors $\boldsymbol{u}_0$ and $\boldsymbol{v}_0$, corresponding to elliptical trajectories of skull motion and brain tissue rigid-body motion, respectively. The vectors normal to the two elliptical trajectories are used to calculate the spatial angle, β. The dot product of the two complex coefficient vectors can be used to calculate temporal phase shift, φ [69]. The vector normal to each ellipse is found from the cross product of the real and imaginary components of the coefficient vectors, as shown in Equations 3.3 and 3.4.

$$\boldsymbol{N_u} = Re[\boldsymbol{u}_0] \times Im[\boldsymbol{u}_0] \tag{3.3}$$

$$\boldsymbol{N_v} = Re[\boldsymbol{v}_0] \times Im[\boldsymbol{v}_0] \tag{3.4}$$

The spatial angle, β, between the two ellipses is then found from Equation 3.5.

$$\cos\beta\,(\boldsymbol{u_0}, \boldsymbol{v_0}) = \frac{(\boldsymbol{N_u} \cdot \boldsymbol{N_v})}{\|\boldsymbol{N_u}\|\|\boldsymbol{N_v}\|} \tag{3.5}$$

In order to compare the phases of skull and brain motion captured in their complex coefficient vectors, a common reference for t = 0 is needed to describe the relative timing between the MRE sequence and skull acceleration profile. The center of the refocusing pulse of the MRE sequence was chosen as the common reference. The temporal phase shift, φ, between skull and brain tissue motion was estimated as the phase angle of the complex dot product (Eq.3.6).

$$\varphi = \angle(\boldsymbol{u}_0{}^* \cdot \boldsymbol{v}_0) \tag{3.6}$$

3.3 Results

3.3.1 Motion of the human skull and gelatin phantom case reconstructed from accelerometers

During MRE imaging of human subjects, the Resoundant^{TM} system causes the pillow actuator to vibrate the back of the skull. Examples of accelerations reconstructed at the anterior, right, and posterior points are shown in Figure 3.3. The acceleration magnitudes typically ranged from 2-5 m/s^2. Acceleration components reconstructed at the left (L) and right (R) skull points were similar in magnitude and phase. The SI component of acceleration was largest at the posterior. AP acceleration magnitudes were similar at all reconstruction points. Data generally suggest a combination of AP linear acceleration and rotation of the skull about the RL axis. The mean magnitudes of the components of skull acceleration for the six human subjects are compared to those of the gelatin phantom case in Table 3.1. The gelatin phantom case had lower acceleration amplitude than the human skull, and the largest component was consistently in the AP direction, even at the posterior reconstruction point.

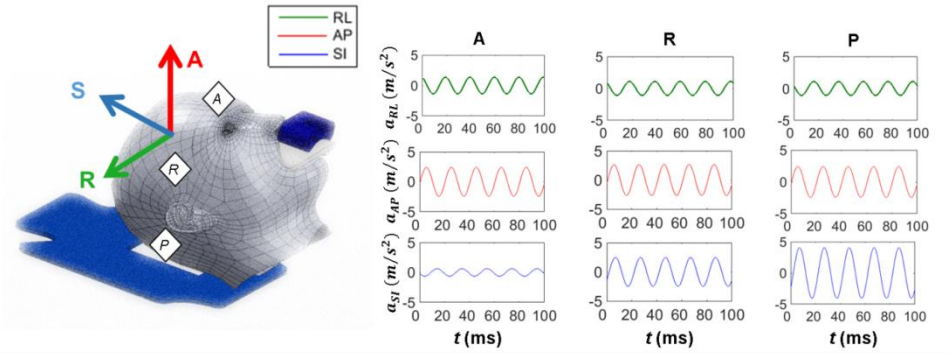

Figure 3.3: Reconstructed acceleration profile (RL - green, AP - red, and SI - blue) at skull anterior (A), right (R), and posterior (P) points during MRE of a typical human subject (actuator frequency: 50 Hz, actuator amplitude = 18%)

To characterize the uncertainty in the accelerometer measurements obtained during MRE in the absence of a reference accelerometer, I compared the accelerations reconstructed at the positions of the embedded accelerometers to the recorded accelerometer data. NRMSE for each acceleration component was obtained by averaging the NRMSE of that component for the three accelerometers in the MGA. Normalized errors for reconstructed accelerations in human studies were: NRMSE = 0.05 (RL direction), NRMSE = 0.10 (AP direction), and NRMSE = 0.07 (SI direction). In the gelatin phantom, reconstructed data also showed reasonable agreement with recorded values: NRMSE = 0.13 (RL direction), NRMSE = 0.10 (AP direction), and NRMSE = 0.16 (SI direction). The higher NRMSE in the gel phantom is likely due to the lower amplitude of acceleration, which leads to a lower signal-to-noise ratio in the data.

Position	Human Skull (n=6)			Gelatin Phantom		
	a_{RL} (RMS m/s^2)	a_{AP} (RMS m/s^2)	a_{SI} (RMS m/s^2)	a_{RL} (RMS m/s^2)	a_{AP} (RMS m/s^2)	a_{SI} (RMS m/s^2)
Anterior	0.60 ± 0.38	2.23 ± 0.46	0.42 ± 0.11	0.15	0.77	0.51
Right	0.58± 0.35	2.31 ± 0.44	1.54 ± 1.06	0.09	0.81	0.33
Left	0.58 ± 0.35	2.16 ± 0.48	1.51 ± 0.71	0.09	0.73	0.41
Posterior	0.61 ± 0.36	2.23 ± 0.46	2.90 ± 1.58	0.05	0.77	0.23
NRMSE (Dimensionless)	0.05	0.10	0.07	0.13	0.10	0.16

Table 3.1: Reconstructed acceleration components for human skull and gelatin phantom case at the four reconstruction points. NRMSE characterizes the accuracy of reconstruction using the difference between the measured accelerations and the accelerations reconstructed at the accelerometer locations.

3.3.2 Motion of human brain tissue and phantom gelatin estimated from MRE

Rigid-body and wave motion in both gelatin and brain tissue were estimated from MRE measurements, as described previously. In the gelatin phantom, most of the total displacement field is due to wave displacement (Figure 3.4a,b). In human subjects, the MRE measurements reflect a relatively uniform displacement field with high amplitude in the AP direction (Figure 3.4d), suggesting a larger contribution from rigid-body motion than from wave displacement fields. Amplitudes of wave displacement and curl in the gelatin phantom (Figure 3.4b,c) were higher relative to total displacement than in human brain tissue.

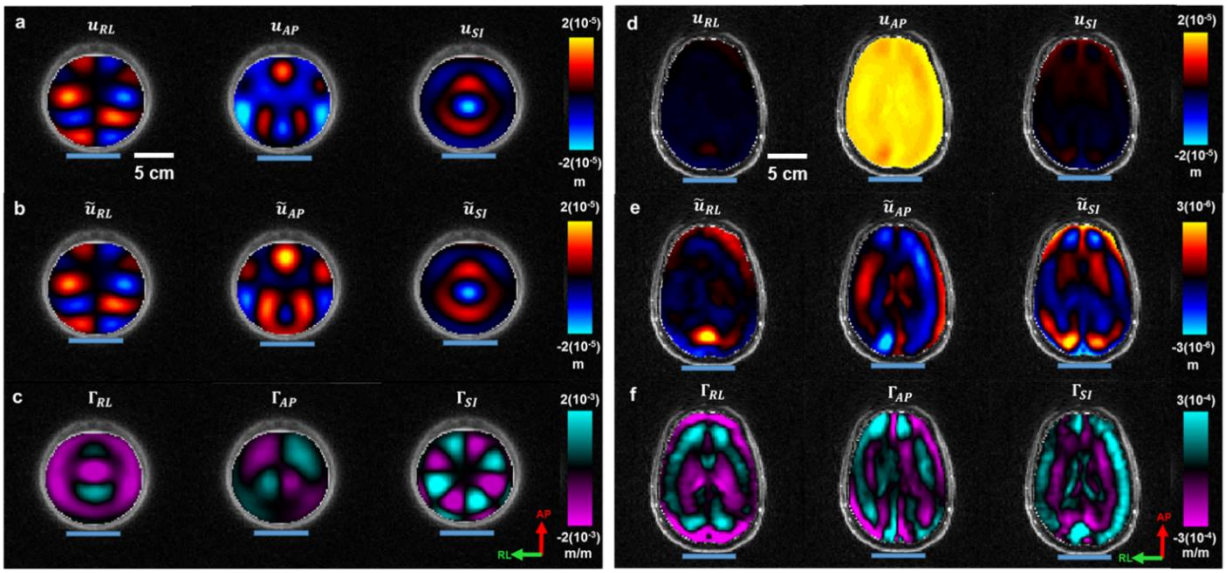

Figure 3.4: (a, d) Representative total MRE displacement fields in (a) the gelatin phantom and (d) a human subject at the first of eight time points; (b, e) corresponding wave displacement fields; (c, f) corresponding curl fields. Wave displacement is obtained by subtracting rigid-body motion from the total displacement field. Note the different displacement color scales in panels (d) and (e). The blue bar at the bottom of each image indicates the approximate location of the pillow actuator.

3.3.3 Comparison of case and gelatin motion in the gelatin phantom

Motion trajectories at four points on the case (estimated from accelerometer measurements) were compared to trajectories at four material points inside the gelatin (estimated from MRE measurements). These comparisons were characterized by relative amplitude, orientation, and phase (Figure 3.5). The rigid-body motion of the gelatin and case were similar in amplitude, particularly the dominant components of rotation (θ_{RL}) and translation ($\bar{u}_{AP}^{O}$). The spatial angle between rigid-body motion of the gelatin and rigid-body motion of the case indicated high alignment of gel and case motion (Table 3.2). The phase shift between case and gelatin rigid-body motion was consistently low.

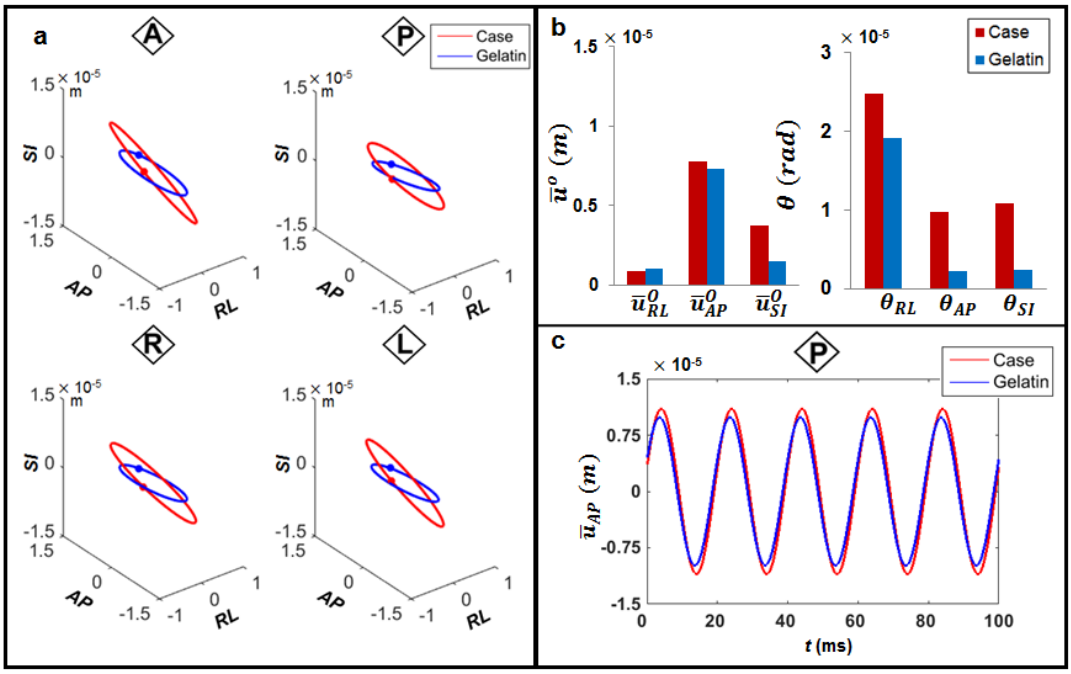

Figure 3.5: Rigid-body motion of the gelatin phantom (estimated from MRE measurements) compared with motion of the case (reconstructed from accelerometer data). a) Motion reconstructed at individual points on the case anterior (A), right (R), left (L), and posterior (P) are compared with corresponding material points within the outermost shell of corresponding gelatin regions. Red and blue dots on the elliptical trajectory indicate the reference time, t=0. b) Rigid-body motion coefficients for translation and rotation about the gelatin phantom origin are compared between the phantom case and gelatin. c) The component of displacement in the AP direction for the case and gelatin posterior reconstruction points is shown as a function of time.

Position	Phantom Case/Gelatin	
	β (rad)	ϕ (rad)
Anterior	0.50	0.26
Right	0.27	0.22
Left	0.32	0.14
Posterior	0.05	0.12

Table 3.2: Spatial angle (β) and temporal phase delay (ϕ) between harmonic motion of the gelatin phantom case and harmonic, rigid-body motion of gelatin.

The magnitudes of wave displacement in gelatin were larger than the amplitudes of rigid-body motion of both the case and gelatin (Figure 3.6). No qualitative differences in curl, displacement, or strain amplitudes were seen between shells or quadrants.

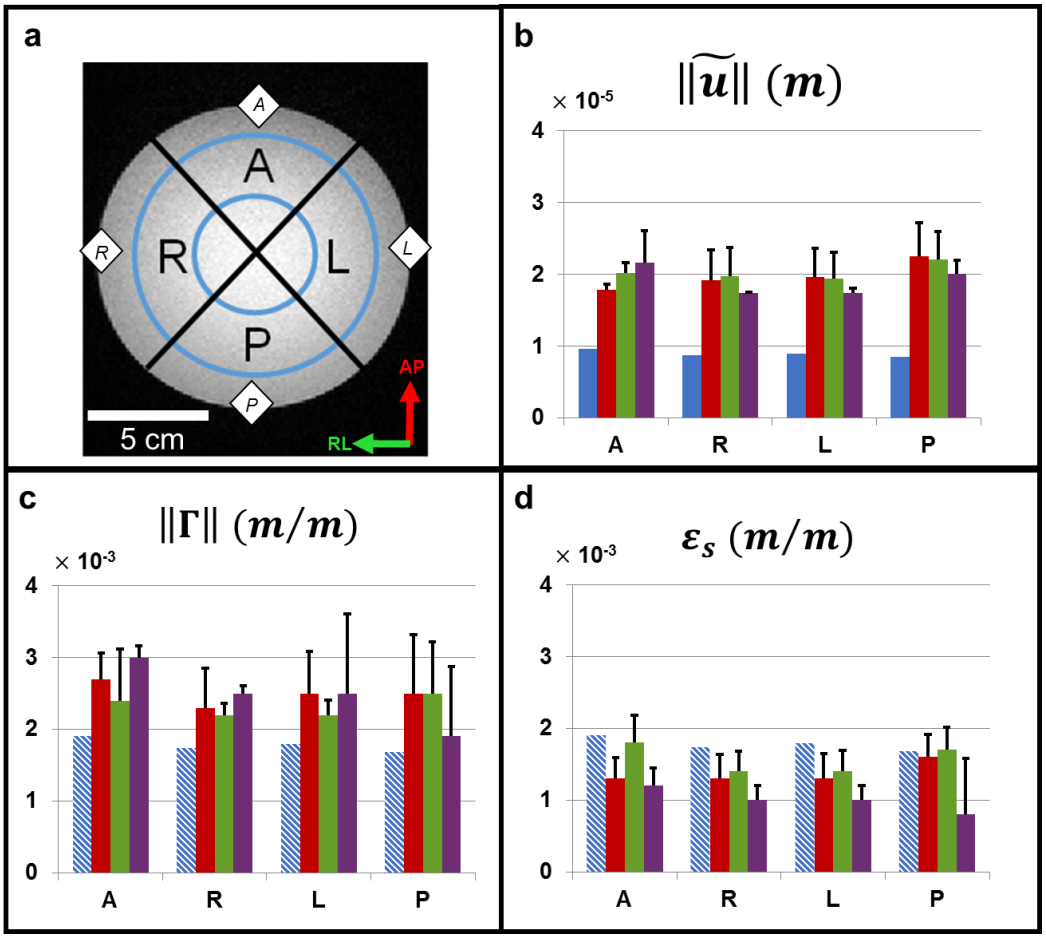

Figure 3.6: Magnitudes (RMS) of (b) wave displacement; (c) curl; and (d) octahedral shear strain in the gelatin phantom. Values are shown for each quadrant-shell ROI (a). For comparison to curl and strain (dimensionless measures of displacement/length), the case displacement magnitude is normalized by the radius of the case (striped). Error bars in all three plots represent the standard deviation of each quantity within the shell ROI.

3.3.4 Comparison of skull and brain motion in human subjects

Brain motion (estimated from MRE measurements) and skull motion (reconstructed from accelerometer measurements) were compared for six subjects. As in the gelatin phantom, elliptical trajectories of neighboring material points were used to compare brain and skull rigid-body motion (Figure 3.7). In contrast to the gelatin phantom, the amplitude of rigid-body motion in the brain differed from the amplitude of nearby skull motion. At each of the brain material points, the AP component of translation was consistently the highest amplitude, while the skull experienced high amplitudes in both AP and SI directions. Rigid-body motion of the brain and skull exhibited greater differences in spatial angle than were seen between the case and contents of the gelatin phantom (Table 3.3). The phase shift between rigid-body motion in brain and skull was consistently longer than between case and gelatin in the gelatin phantom.

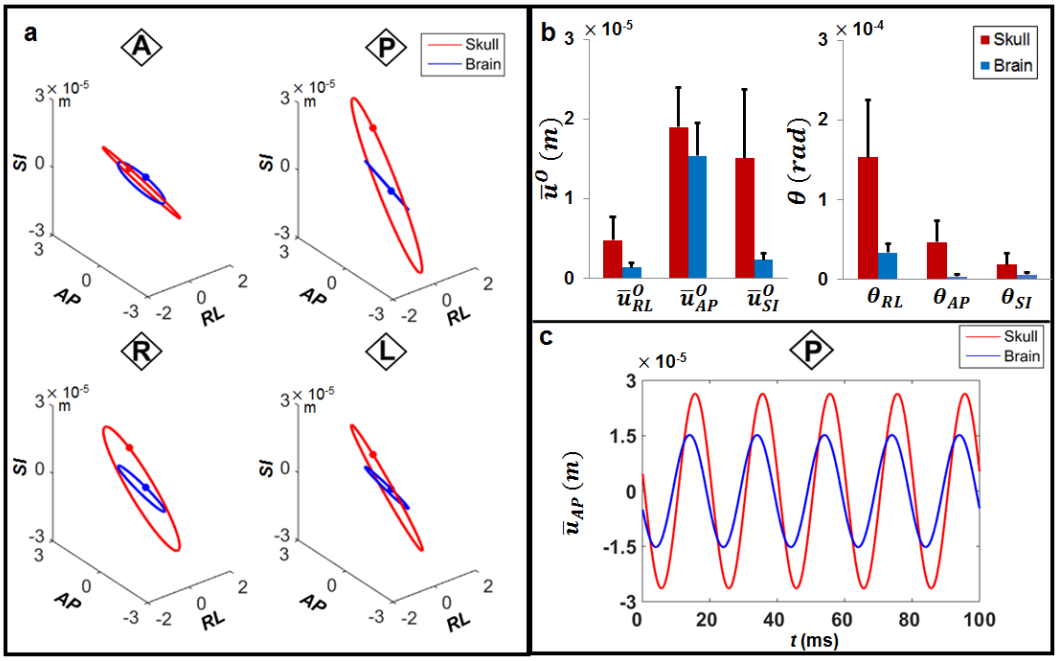

Figure 3.7: **Rigid-body motion of human brain tissue estimated from MRE measurements, compared with skull motion reconstructed from accelerometer data. a) Trajectories at individual reconstruction points on the skull anterior (A), right (R), left (L), and posterior (P) are compared with analogous trajectories of neighboring brain tissue material points selected from the outer shell ROI. Red and blue dots in the elliptical trajectories indicate the reference time, t=0. b) The amplitude of the rigid-body motion coefficients for translation and rotation about the skull origin are compared between the skull and brain (n=6). Error bars indicate standard deviation between subjects. c) The component of displacement in the AP direction is plotted for the skull and brain posterior reconstruction points.**

Position	Human Skull/Brain (n=6)	
	β (rad)	ϕ (rad)
Anterior	0.55 ± 0.30	5.16 ± 1.12
Right	0.59 ± 0.32	5.13 ± 1.22
Left	0.69 ± 0.51	5.13 ± 1.13
Posterior	0.97 ± 0.37	5.09 ± 1.18

Table 3.3: **Spatial angle (β) and temporal phase delay (ϕ) between harmonic motion of the human skull and harmonic, rigid-body motion of brain tissue.**

The amplitude of wave motion in brain tissue was lower than the amplitude of reconstructed skull motion (Figure 3.8) in all quadrants and shells. The displacement amplitudes in the outer and middle shells were typically higher than in the inner shell. The amplitudes of curl and strain also decreased progressively in regions closer to the center of the brain.

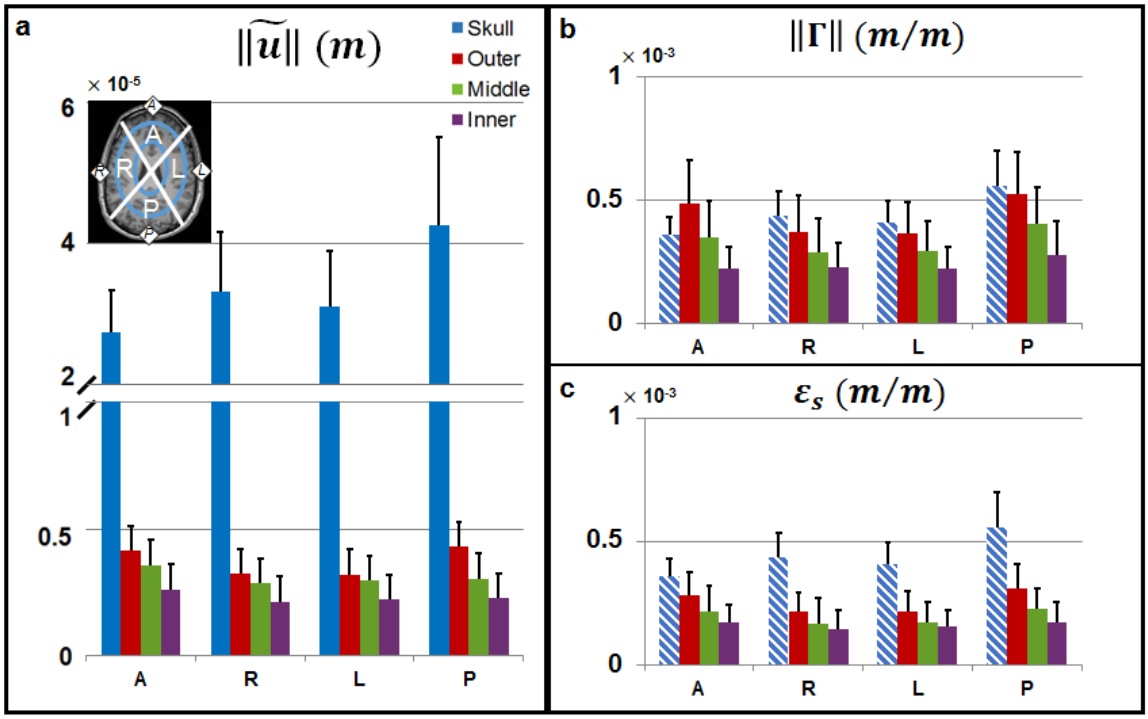

Figure 3.8: Magnitudes (RMS) of (a) wave displacement; (b) curl; and (c) octahedral shear strain, in the human brain. Values are shown for each quadrant-shell ROI. For comparison with curl and strain (dimensionless measures of displacement/length), skull displacement magnitude is normalized by the major semi-axis of the skull (striped). Error bars in all three plots show the standard deviation among subjects (n=6).

3.4 Discussion and Conclusions

In this study I directly characterized skull kinematics using accelerometers in order to relate skull motion to brain tissue motion. To describe brain tissue motion, MRE measurements of displacement were decomposed into wave motion and rigid-body motion. Comparing skull kinematics with brain tissue motion *in vivo* enables assessment of relative motion and deformation. Furthermore, comparison of data from human subjects to data from a gelatin phantom (in which the gelatin adheres to the cylindrical case) provides insight into how the skull-brain interface (a more complex material interface) affects motion transmission.

The effects of the skull-brain interface are illuminated by comparison to the coupling of case to gelatin in the gelatin phantom. In the phantom, harmonic, rigid-body displacements of both gelatin and case were similar. Material points in the case and material points in gelatin exhibited elliptical trajectories due to rigid-body motion. The elliptical trajectories of neighboring points on opposite sides of the adherent interface exhibited similar amplitude, direction (spatial angle), and temporal phase. While I expect particles in the case and in the gelatin at the interface to have almost identical trajectories, discrepancies in the rigid-body motions are apparent (Figure 3.5, e.g.). There are several likely reasons: (i) gelatin motion includes both rigid-body and wave motion; (ii) the case is not perfectly rigid (which introduces some error into the estimate of case motion); (iii) motion estimates from MRE are average values within a finite region of interest. Displacements in the gelatin due to waves were consistently higher than the displacements due to rigid-body motion of the gelatin and case. It is likely that harmonic excitation at 50 Hz induces

constructive wave interactions in the weakly-dissipative gelatin, causing higher displacement fields in the interior.

In contrast, displacement fields in the human brain exhibited higher amplitudes of rigid-body motion than wave motion. Furthermore, rigid-body motion of the brain differed strongly from rigid-body motion of the skull. Considering first the rigid-body components of motion, elliptical trajectories of material points in the brain exhibited significant differences in amplitude, orientation (spatial angle), and temporal phase compared to elliptical trajectories of neighboring points on the skull. Wave components of displacement in the brain were even smaller relative to skull motion; displacements due to waves at material points in the brain were an order of magnitude smaller than displacements of neighboring material points in the skull. In addition, waves were attenuated significantly as they propagated inward from the outer cortical surface toward the midbrain.

These results indicate significant mechanical compliance and dissipation at the skull-brain interface. These properties are attributable to the dural membranes, blood vessels, and fluids that comprise the interface. In contrast, the gelatin phantom has none of these structures, and the adherent interface between gelatin and case exhibits dramatically simpler behavior.

Some experimental limitations are acknowledged. All analyses performed in this study assumed perfect coupling between the accelerometers and the skull. In practice, this is unlikely; slip or compliance will affect the transmission of motion from the jaw, via the commercial mouth guard,

to the accelerometer array. Accelerations were assumed to be harmonic; Fourier components at a single frequency were converted to displacement in the frequency-domain for comparison with MRE measurements. As noted in the description of experimental methods, and in the Appendix, the methods for measurement and reconstruction of skull kinematics from accelerometer data were validated in separate experiments.

Substantial variation in acceleration (Table 3.1) and spatial angle (Table 3.3) between skull and brain motion is seen over the cohort of six subjects. These variations likely reflect inter-subject differences in head size, shape, and anatomy, as well as individual responses to actuation and variations in subject and actuator positioning. Despite inter-subject variability, subjects consistently showed higher amplitudes of skull translation in the AP and SI directions, relative to RL translation, and higher amplitudes of rotation about the RL axis, relative to other rotation components. Additionally, recorded human MRE data is consistent with results reported by other groups using a similar actuation system [56].

3.5 Summary

This study demonstrates that the skull-brain interface is a critical determinant of brain tissue deformation due to skull loading, and thus is a major factor in TBI. The properties of this interface are measurable; the quantitative data from this study should be of immediate use in the parameterization and validation of computer models and simulations of TBI. The properties of the skull-brain interface are also critical to the development of strategies for MRE of the brain, in which enhanced transmission of waves into the brain is desirable. The compliant and dissipative nature of the skull-brain interface protects the brain during mild skull accelerations.

While work in this section demonstrates that it is possible to acquire full, 3D kinematics estimates of skull and brain motion *in vivo*, accelerometer data acquisition is cumbersome and susceptible to inter-subject variation. Finding surrogate measures of skull motion so that only a single MRE scan is required would greatly facilitate estimation of simultaneous head excitation and resulting brain tissue deformation.

Chapter 4: Estimation of Simultaneous Scalp, Skull, and Brain Displacements with MR Elastography

4.1 Overview

Studies described in the previous chapter demonstrated the ability to comparing MRE estimates of brain tissue displacement with direct mechanical characterization of skull motion using MRI-safe tri-axial accelerometers. In order to provide similar characterization without the need for an accelerometer array, this work considers using MRE to provide simultaneous estimates of head and brain motion.

Challenges to imaging skull motion include phase wrapping, voxel resolution, and low signal magnitude in bone. Alternatively, the motion of soft tissue surrounding the skull (scalp) can be measured and may enable estimation of skull motion. To assess the relationship between brain, skull, and scalp motion, I estimated rigid-body displacements of brain and scalp from MRE with low motion-encoding gradient (MEG) amplitudes and compared with skull displacements estimated from an instrumented mouth guard containing three tri-axial accelerometers.

The material presented in this chapter has been submitted as a manuscript to the Journal of Biomechanics.

4.2 Methods

4.2.1 MRE imaging procedures and instrumentation

MRE was performed on 6 adult human subjects (5 males and 1 female; median age 28 years) on a Siemens Trio® 3T MRI scanner located at the Center for Clinical Imaging Research at Washington University in St. Louis. All studies were approved by the Institutional Review Board (IRB). The subject was positioned supine within a 12 channel head coil. Skull vibrations were induced at a frequency of 50 Hz through a commercially available system using a "pillow" actuator (Resoundant, Rochester, MN) positioned at the back of the head (Figure 4.1a,c). The subject's head rested on the inflatable portion of the actuator and was stabilized by padding at the temples. Skull kinematics were estimated using three MRI-safe, tri-axial accelerometers (TSD109C2-MRI, BIOPAC©, Goleta, CA) embedded in a mouth guard array (MGA) based on a commercial sports mouth guard and 3D-printed interface (Figure 4.1b).

MRE displacement data was acquired using an echo-planar imaging (EPI) sequence augmented with two bipolar MEGs. Images were acquired with 3 MEG directions at four MEG strengths and with 8 phase offsets. MEGs were flow-compensated, applied bilateral to the RF refocusing pulse, and had duration matched to the period of vibration [70]. Additional parameters included: TR/TE = 2880/63 ms; GRAPPA = 3; FOV = 240x240 mm^2; matrix = 80x80 matrix; 24 axial slices; and 3 mm isotropic voxels. Initially, MEG strengths of 8, 10, 16, and 26 mT/m were selected for this study (1 subject); however some phase wrapping was still observed in scalp tissue voxels at 8 mT/m so the remaining scans (5 subjects) were done with a lower range of MEG strengths: 4, 7, 10, and 26 mT/m. Comparison between data obtained with 4 mT/m and 7

mT/m MEGs in the remaining subjects indicated that 7 mT/m was the best choice for encoding scalp and brain motion without phase wrapping. The highest MEG strength of 26 mT/m was used to quantify brain dynamic deformation for all six subjects. MRE phase data was filtered using the medfilt3 command in MATLAB® (2014a, MathWorks®, Natick, MA). Due to field inhomogeneity artifact in both the brain and scalp at the bottom of the slice volume, only the central 20 slices were used for analysis (Figure 4.1d).

While the accelerometers are MRI-safe, they can induce imaging artifacts, thus the scanning protocol began with a truncated, six-slice version of the EPI sequence with duration of approximately 40 s in order to record both skull accelerations and signal landmarks during the MRE sequence [64]. Skull accelerations and MRE sequence triggers were recorded at 10,000 samples/sec. Following this scan, the accelerometer array was removed while the subject's head remained in the head coil. Next, a T1-weighted 3D MP-RAGE sequence with 0.9 mm isotropic voxel resolution was performed followed by four 24 slice EPI-MRE scans, each with increasing MEG strength. The duration of each 24 slice MRE scan was 2.5 minutes; the total time of the scanning procedure was 35–45 minutes.

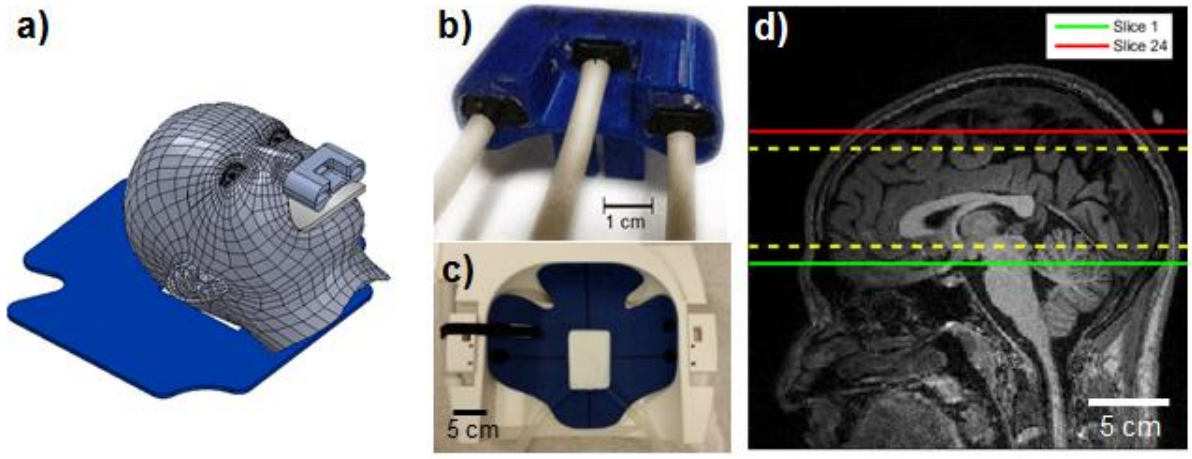

Figure 4.1: Overview of human EPI-MRE data collection setup. a) Schematic rendering of the accelerometer mouth guard array (MGA) and its positioning for a human subject lying on the pillow actuator. (b) Three tri-axial accelerometers are embedded within the MGA. (c) The pillow actuator is placed within the 12 channel head coil and the subject's head is placed on the actuator and preloaded with padding (not shown). (d) Twenty-four axial EPI-MRE slices with 3 mm voxel resolution were acquired with a slice volume centered on the corpus callosum. Due to artifact in the lower slices, only the central twenty slices (outlined by the dotted yellow) were analyzed in this study.

4.2.2 Estimation of 3D skull, scalp, and brain motion

Skull kinematics were estimated from accelerometer recordings using the methods detailed in previous chapters. As with the previous study, motion-induced MRE phase contrast ($\boldsymbol{\Phi}$), is proportional to the component of the oscillatory displacement in the direction of the gradient [34], [71]. The sensitivity of phase measured by an MRE sequence depends on the strength, shape, and number of the MEGs [64], [71]. For this study, displacement conversions were 10.47 μm/rad (7 mT/m), 9.17 μm/rad (8 mT/m), and 2.82 μm/rad (26 mT/m). By successively applying motion-encoding gradients in three orthogonal directions, an oscillatory displacement field ($\boldsymbol{u}$) is obtained; this field captures the effects of rigid-body motion, longitudinal wave motion, and shear wave motion. MRE displacements are acquired at 8 time points for a single cycle.

Phase wrapping occurs when the phase contrast in a displacement component exceeds the range $-\pi$ to π (Figure 4.2). During MRE, the magnitude of motion-encoded phase measured from scalp voxels was typically larger than the phase measured in brain voxels. With the actuator type and placement used in this study, scalp motion was usually phase-wrapped at higher MEG strengths (10 mT/m or 26 mT/m). Unwrapped scalp displacements were found by using data obtained at a lower MEG strength of 7 mT/m (in five subjects) and 8 mT/m (in one subject). Similarly, the anterior-posterior (AP) component of brain motion may also be wrapped (Figure 2d) at higher MEG strengths. Wrapped brain AP displacement data obtained at 26 mT/m MEG strength were spatially unwrapped using FSL PRELUDE [72] and then temporally unwrapped by comparing to MRE data at the same time points obtained at 7 or 8 mT/m MEG strength for the same subject (Figure 4.2b-c).

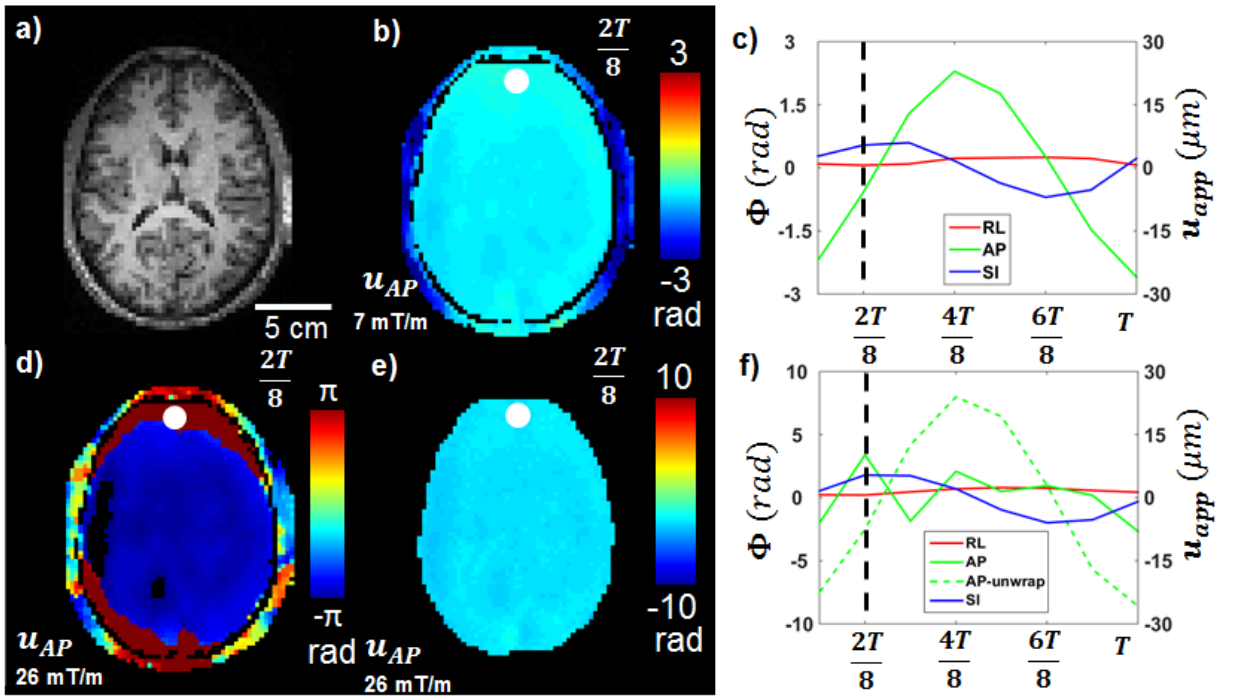

Figure 4.2: Phase wrapping is a challenge for capturing large motion in an MRE sequence. a) Anatomical T1W image of the central slice of the MRE slice volume. Anatomical data is interpolated to have the same voxel resolution (3 mm) as MRE images. b) MRE data acquisition at a lower MEGS of 7 mT/m provides original unwrapped signal with a lower resulting phase. c) RL (red), AP (green), and SI (blue) components of MRE phase contrast at a single brain voxel in Figure 4.2b (white circle) are shown with a period of 8 time points. MRE phase contrast is converted to an apparent displacement estimate (u_{app}) using a phase-to-displacement calibration factor based on the MEGS. d) AP component of MRE phase contrast acquired at 26 mT/m exceeds the principal range of $-\pi{:}\,\pi$ and is wrapped in some scalp and brain regions. e) Brain displacement encoded at 26 mT/m is spatially and temporally unwrapped. f) Phase wrapping is predominantly found in the AP component of brain displacement (solid green) at a single brain voxel in Figure 4.2d. After unwrapping, the original AP component of displacement (dotted green) is recovered for the same brain voxel. MRE phase contrast acquired at 7 mT/m is lower than at 26 mT/m, however apparent displacement is proportional after unwrapping.

Scalp and brain regions were isolated by thresholding MRE signal magnitude (S) (Figure 4.3d-e). These regions were validated through comparison with T1-weighted images interpolated onto the MRE slice planes. The scalp is deformable and heterogeneously coupled to the skull. I postulated that scalp voxels with higher amplitudes of harmonic motion are more closely coupled to the skull, and more representative of skull motion. Accordingly, scalp voxels with high motion amplitude and dominant contributions at the fundamental frequency of 50 Hz were selected from

MRE data obtained at 7 mT/m and 8 mT/m. First, the head was divided into four quadrants, anterior (A), right (R), left (L), and posterior (P) (Figure 4.3a); second, scalp voxels in each quadrant were given a composite score (β) as calculated in Equation 4.1a-c:

$$\bar{\Phi} = \|\boldsymbol{\Phi}\| / \|\boldsymbol{\Phi}_{max}\| \tag{4.1a}$$

$$\bar{c} = \|\boldsymbol{c}\| / \|\boldsymbol{c}_{max}\| \; ; \; c_i = \frac{|c_{1i}|}{\sum_{n=0}^{7} |\boldsymbol{c_{ni}}|} \tag{4.1b}$$

$$\beta = 0.5\bar{\Phi} + 0.5\bar{c} \tag{4.1c}$$

Here, MRE phase contrast amplitude ($\bar{\Phi}$) at each voxel is calculated as the amplitude of phase contrast ($\|\boldsymbol{\Phi}\|$) scaled by the maximum phase contrast amplitude among all scalp voxels ($\|\boldsymbol{\Phi}_{max}\|$) (Eq. 4.1a). The normalized amplitude of the fundamental harmonic ($\bar{c}$) at each voxel is then calculated as the relative amplitude at the fundamental frequency ($\|\boldsymbol{c}\|$) scaled by its maximum among the scalp voxels ($\|\boldsymbol{c}_{max}\|$). For each component, c_i, the contribution of the fundamental frequency is calculated from amplitude of the FFT at the fundamental frequency ($|c_{1i}|$) divided by the sum of the FFT amplitudes at all frequencies ($\sum_{n=0}^{7} |c_{ni}|$) (Eq. 4.1b). The composite score, β, is then calculated from the sum of the two measures (Figure 3b; Eq. 4.1c). The N voxels in each quadrant with the highest scores were selected to give a total of $4N$ scalp voxels (Figure 4.3c). For the current study, N=100 voxels were chosen per quadrant. MRE data from the brain and selected scalp voxels were then separately fitted to a model of rigid-body motion to find expressions for rigid-body translation ($\bar{\boldsymbol{u}}$) and rotation ($\boldsymbol{\theta}$) about a common origin located at the posterior clinoid process.

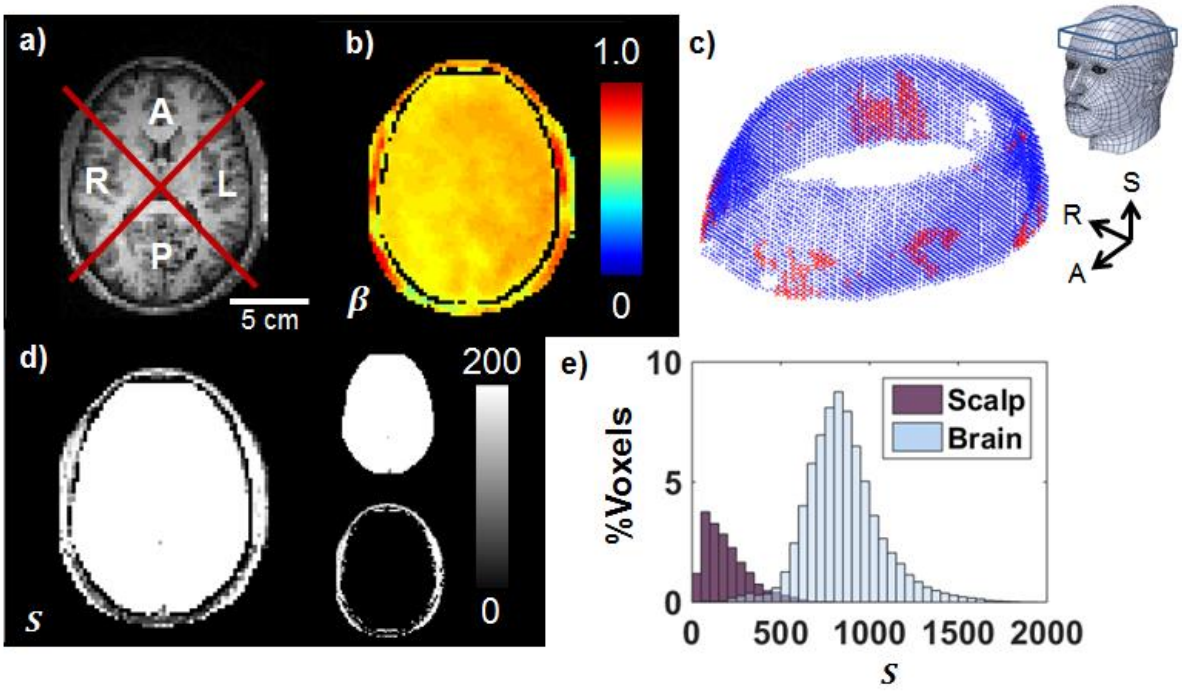

Figure 4.3: Scalp voxels for estimation of rigid-body motion are selected by identifying voxels with high MRE phase contrast amplitude and coherent harmonic motion. a) MRE slices are divided into four quadrants to ensure that selected voxels are spatially distributed throughout the scalp. These four quadrants are also used for later analysis of skull, scalp, and brain motion. b) Scalp voxel score β is shown for central MRE slice. Score is computed by equally weighting MRE phase contrast amplitude and the relative power at the fundamental frequency (50 Hz). c) All scalp voxels are shown as 3D points surrounding the MRE slice volume. Voxels selected for scalp rigid-body motion estimation are outlined in red. d) MRE signal magnitude (S) is higher in brain tissue than in scalp. Thresholding the image by signal magnitude enables creation of brain and scalp region-of-interest (ROI) masks. e) Histogram of signal distribution for both scalp (purple) and brain (gray) voxels.

Estimates of skull displacement (reconstructed from accelerometer measurements) were compared to analogous estimates of rigid-body displacement within the brain and scalp (estimated from MRE measurements). In harmonic motion, where the three components of motion are not in phase, the 3D trajectory of each point in the skull, scalp, and brain is an ellipse, which can be represented as a complex coefficient vector, $\boldsymbol{u}_0$, multiplied by a complex exponential in time, $\boldsymbol{u}(t) = \boldsymbol{u}_0 \exp(i\Omega t)$. The elliptical trajectories of material points in skull,

scalp, and brain were described by their relative amplitudes and temporal phase. The amplitude of each elliptical trajectory is reported as its mean radius: the circumference of the ellipse divided by 2π.

To describe temporal relationships, consider two 3D complex coefficient vectors $\boldsymbol{u}_0$ and $\boldsymbol{v}_0$, corresponding to elliptical trajectories of skull motion and brain rigid-body motion, respectively. As shown in Equation 4.2, the dot product of the two complex coefficient vectors can be used to calculate temporal phase shift, ϕ [69].

$$\phi = \angle(\boldsymbol{u}_0{}^* \cdot \boldsymbol{v}_0) \tag{4.2}$$

Similarly, the temporal phase shift between scalp and brain rigid-body motion can be calculated. For this analysis, phase and amplitude differences between the skull, scalp, and brain were compared by analyzing the elliptical trajectories of voxels within corresponding quadrants (Figure 4.3a). In order to compare phase delay between accelerometer estimates of skull motion and MRE estimates of rigid-body motion, both sets of measurements were synchronized with respect to the EPI refocusing gradient [64].

4.3 Results

4.3.1 Comparison of total displacement of the skull, scalp, and brain

One period of harmonic motion (period T) is described by eight temporal samples (at $t = T/8, 2T/8, \ldots, T$). In Figure 4.4, total displacement in the AP direction (the dominant direction of translation) is shown in the skull, scalp, and brain for a representative subject at four time points (an approximate skull "shell" was created from the region between the scalp and brain masks). Here, total displacement in the skull is simply the rigid-body motion estimated from accelerometers. In the scalp and brain, total motion includes contributions from both dynamic deformation and rigid-body motion.

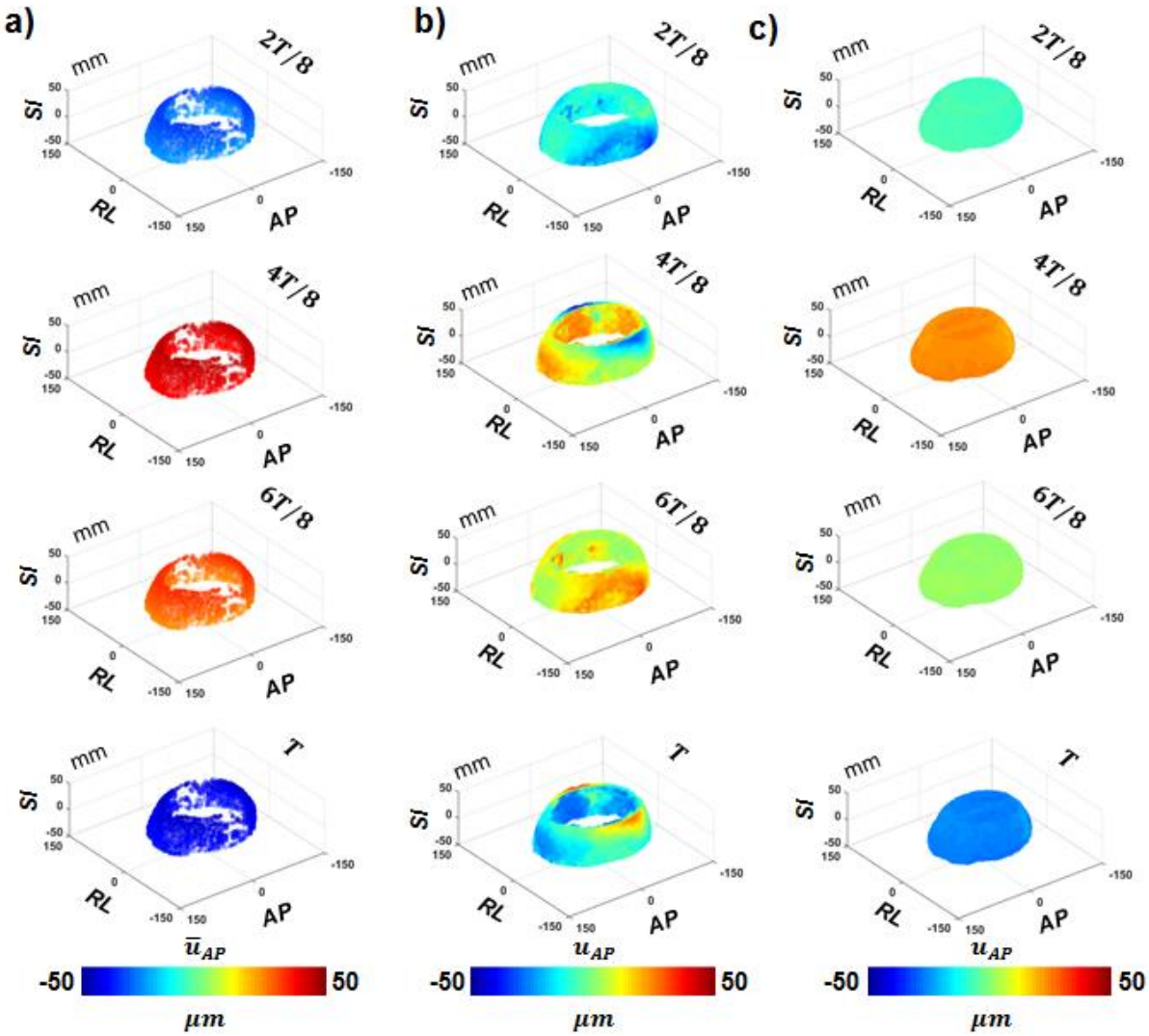

Figure 4.4: Total displacements (AP-component) of the a) skull, b) scalp, and c) brain for a single subject are shown at four equally-spaced time points within one cycle of harmonic excitation.

4.3.2 Comparison of rigid-body displacement of the skull, scalp, and brain

Rigid-body motion of the scalp and brain were extracted from 7-8 mT/m MRE data and compared with rigid-body motion of the skull estimated from accelerometers (Figure 4.5). The skull typically has the largest estimates of rigid-body motion amplitude, followed by the scalp and the brain, respectively. Significant phase differences exist between rigid-body motion of each region.

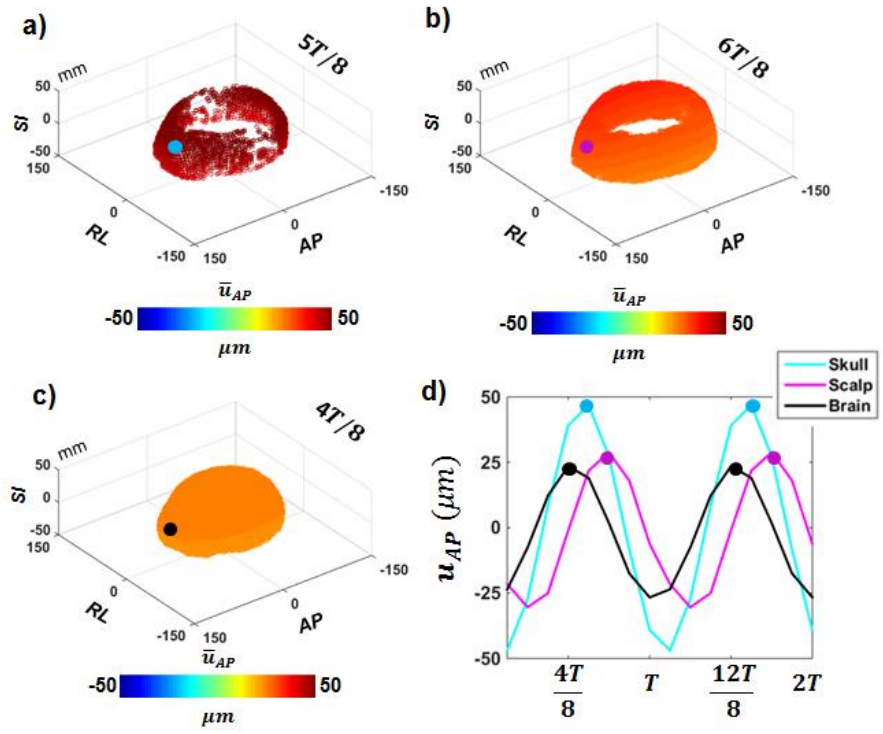

Figure 4.5: Rigid-body displacements (AP-component) for a single subject are shown at the time point corresponding to the maximum displacement of the a) skull (t=5T/8), b) scalp (t=6T/8), and c) brain (t=4T/8). d) Time course of representative voxels in each region near the anterior of the head (Skull-cyan, Scalp-magenta, Brain-black) shows differences in amplitude and phase of AP rigid-body motion. The location of the representative voxels are shown on panels a), b), and c) respectively.

The amplitude and phase of rigid-body motion across all six subjects are compared in Figure 4.6. The largest component of translation for all three regions is in the AP direction, though the skull often exhibits a relatively large SI component of translation. The highest component of rotation is typically about the RL axis. The brain exhibits lower rotations than the skull and scalp. As shown in Figure 4.6c, the mean temporal phase shift between skull and brain motion ($\phi_{Sk/Br}$) is similar to the phase shift between scalp and brain motion ($\phi_{Sc/Br}$), however there are much larger variations in estimated phase shift between skull and brain motion compared to the variations of estimates of phase shift between the scalp and brain. Table 4.1 lists the mean and standard deviation for $\phi_{Sk/Br}$ and $\phi_{Sc/Br}$ across each of the four quadrants.

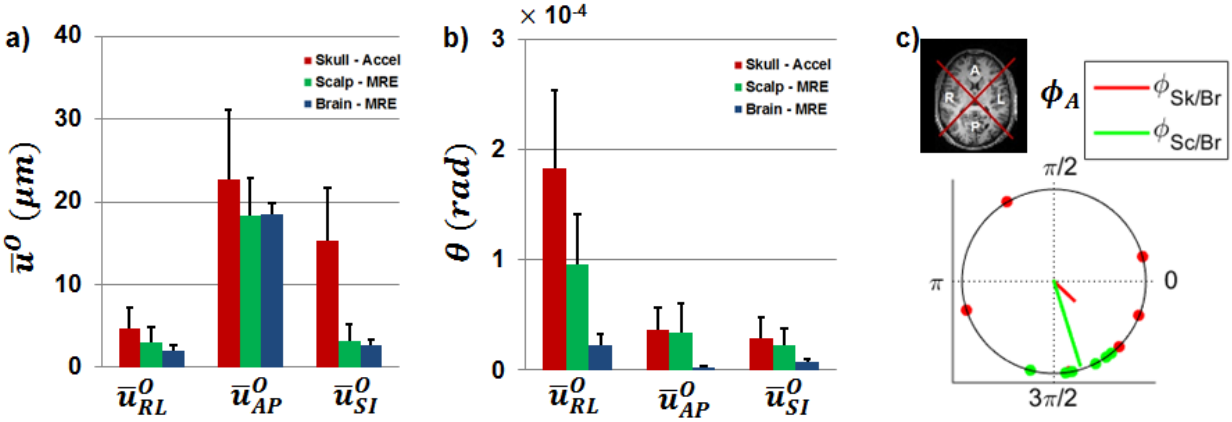

Figure 4.6: Comparison of RMS amplitude of rigid-body motion: a) translation and b) rotation for the skull (red), scalp (green), and brain (blue) at the posterior clinoid process. Error bars indicate standard deviation (n=6). C) Phase shift [$\phi_{Sk/Br}$] between harmonic displacements of anterior points on the skull and brain (red); phase shift [$\phi_{Sc/Br}$] between harmonic displacements of anterior points on the scalp and brain (green). Mean phase delay is plotted as a vector and scaled by deviation. Individual observations are shown for each subject.

	$\phi_{Sk/Br}$ (rad)	$\phi_{Sc/Br}$ (rad)
Ant.	5.52 ± 1.18	5.02 ± 0.32
Right	5.51 ± 1.20	5.00 ± 0.30
Left	5.49 ± 1.19	5.08 ± 0.38
Post.	5.48 ± 1.20	5.03 ± 0.34

Table 4.1: (i) Temporal phase shift, $\phi_{Sk/Br}$, between harmonic motion of the skull (estimated by accelerometers and brain (estimated by MRE) and (ii) phase shift, $\phi_{Sc/Br}$, between scalp and brain motion (both estimated from MRE). Results are shown for each of the four quadrants.

4.3.3 Comparison of wave displacement of the scalp and brain

Dynamic deformation, $\tilde{\boldsymbol{u}}$, in the scalp and brain was estimated from the difference between total motion and rigid-body motion at 7 mT/m for scalp data and 26 mT/m for brain data. Figure 4.7 shows each component of dynamic deformation for the full scalp region and a single slice of brain tissue at a single time point.

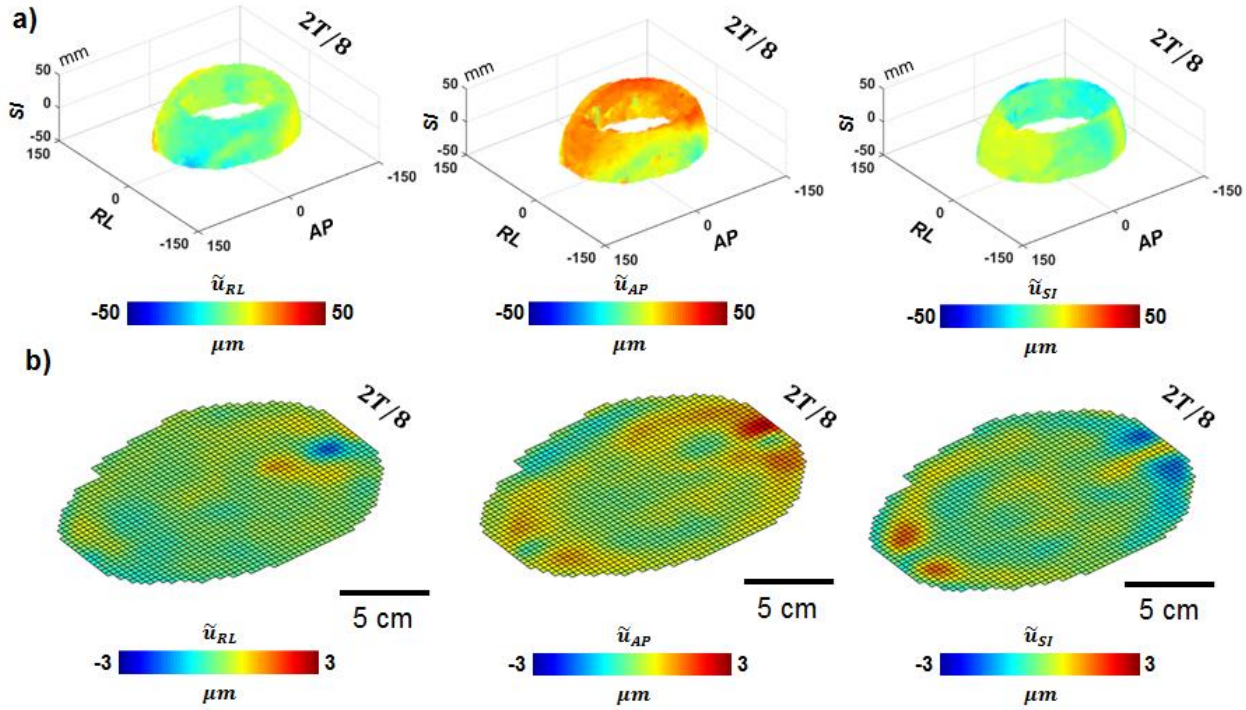

Figure 4.7: RL, AP, and SI components of dynamic deformation for a) scalp and b) central slice of brain tissue. Note difference in color scale between scalp and brain figures, reflecting the difference in deformation amplitude.

4.3.4 Comparison of rigid-body and deformation amplitudes in the skull, scalp, and brain

Amplitudes of displacements due to rigid-body motion (skull, scalp, and brain) and deformation (scalp and brain) were calculated from the mean elliptical radius for voxels within the four quadrants shown in Figure 4.3a. All available voxels were used for both the skull and brain while for the scalp only the 400 voxels with the highest β scores were used. Scalp and brain rigid-body and deformation amplitudes were compared across the six subjects for each quadrant (Figure 4.8). Estimated rigid-body displacements of the skull are larger than those of the scalp or brain. Dynamic deformation is larger in the scalp than in the brain (Figure 4.7). Brain tissue displacement due to deformation was consistently smaller than both skull rigid-body displacement and scalp rigid-body displacement.

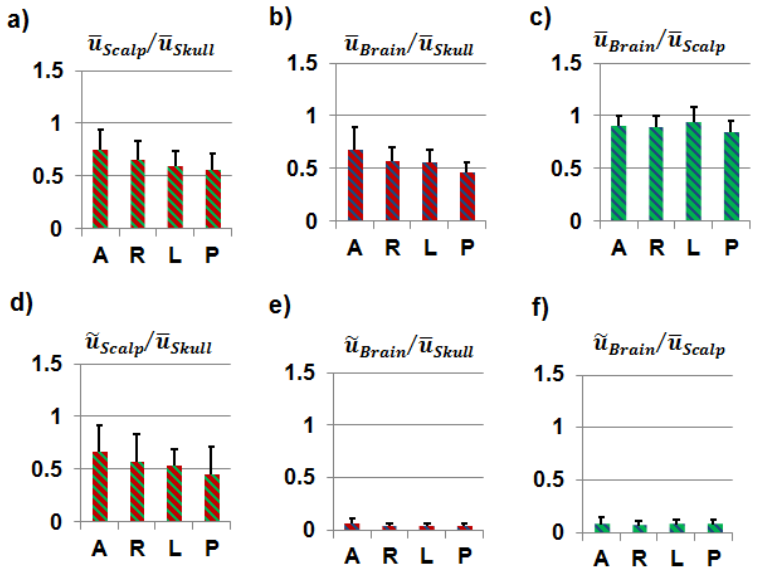

Figure 4.8: Ratios of rigid-body displacement amplitude for the a) scalp and skull, b) brain and skull, and c) brain and scalp followed by ratios of dynamic deformation amplitude to rigid-body displacement amplitude for the d) scalp and skull, e) brain and skull, and f) brain and scalp.

4.4 Discussion and Conclusions

In this study, MRE estimates of scalp and brain tissue motion were compared to accelerometer-derived estimates of skull motion to illuminate the relationship between scalp motion (which can be measured readily with external sensors in a variety of situations) and brain motion (which can only be measured with sophisticated imaging technology under controlled conditions). Under excitation at 50 Hz using the pillow actuator, rigid-body translation in the AP direction was dominant for all three anatomical regions. Rigid-body displacements of the brain and scalp, estimated by MRE, are smaller than skull displacement estimated from accelerometers (Figure 4.5). The scalp appears to experience relatively high dynamic deformations. In contrast, the brain experiences low amplitudes of dynamic deformation compared to its rigid-body displacement.

The motions of scalp and skull are qualitatively similar, with large AP translations and large rotations about the RL axis relative to other components of displacement. In contrast, while the brain experiences high AP translation (Figure 4.6), it undergoes relatively little rotation. The average estimated phase shift between skull and brain is similar to the phase shift between scalp and brain, though the former has a larger variability across subjects. The large phase shifts indicate that the skull-brain interface is quite compliant. The higher variability between skull and brain phase shift may arise because skull motion is measured with a different sensor (scalp and brain are both measured by MRE), and the coupling between the accelerometer array and skull is more variable from subject-to-subject.

Significant attenuation of motion transmitted from the skull to brain was observed, which was mirrored by the ratio between scalp and brain motion. The relatively consistent ratio between the amplitude of rigid-body displacement of the scalp (from MRE) to the amplitude of deformation in brain tissue (from MRE) indicates that MRE alone can be used to quantify head biomechanics.

Data from this study indicate attenuation of motion imparted from the skull to the scalp. Dynamic deformations, comparable in amplitude to rigid body motion, are also seen in the scalp. In monitoring athletes for head impact, sensors may be embedded in helmets [73], attached to mouthguards [74], or mounted to the scalp, [75], [76]. When estimating skull motion or brain motion from such sensors, it is important to know that scalp-based measurements are not precise measurements of the underlying skull motion, but that consistent relationships between scalp motion, skull motion, and brain deformation may be obtained from multiple, spatially-distributed scalp sensors.

Some experimental limitations are acknowledged. Estimates of skull motion assume perfect coupling between the skull and accelerometers. Additionally, the spacing between accelerometers is small compared to the size of the head, which can limit the precision of rigid-body motion estimates in the skull. Large deformations in the scalp might distort estimates of rigid-body motion, though scalp voxels for rigid-body motion estimation are selected from areas postulated to be best coupled to the skull. The MRE sequence used in this study is not optimized for imaging the scalp; some measurement uncertainty may arise due to lower signal-to-noise.

4.5 Summary

This study demonstrates the feasibility of using MRE to simultaneously measure scalp motion and brain tissue deformation in order to characterize the biodynamics of the human head. Results suggest that reasonable estimates of skull motion and brain deformation can be obtained from arrays of scalp-mounted sensors, although such arrays must be designed appropriately and data must be interpreted with care [75]. The current measurements of simultaneous skull, scalp and brain motion *in vivo* will enhance future experimental studies of head kinematics and simulations of TBI biomechanics.

Chapter 5: Physical and Computational Modeling of the Mechanical Behavior of the Skull-Brain Interface

5.1 Overview

While other parts of this project have focused on characterizing the dynamic response of the human head *in vivo*, this section focuses on the creation of physical analogs, or phantoms, to model skull-brain interactions. In Chapter 3, a glycerol-gelatin phantom was used for comparison with human data. While the glycerol-gelatin experienced high wave motion, a tissue surrogate composed of a permanent material that has more damping, greater elasticity, and is less sensitive to temperature would be preferred. Previous studies on soft tissue mimics indicated that Sylgard® 527, a two-part dielectric gel with tunable material stiffness, fit these criteria and could serve as a useful surrogate for brain tissue.

In this study, three cylindrical phantoms and three cranial Sylgard® 527 phantoms of varying complexity were fabricated to simplify and capture the mechanical contributions of the skull-brain interface. I created and tested three cases for the cylindrical and cranial phantom series: (i) a homogeneous phantom with only cured Sylgard® 527, (ii) an interface phantom, with cured Sylgard® 527 separated from the phantom case by a thin layer of liquid Sylgard® 527 base, and (iii) an interface phantom with 3D printed polyvinyl alcohol (PVA) membranes extruding from the interior of the phantom case into the cured Sylgard® 527. Finite element simulations of the cylindrical models were created to provide further insight into the MRE experiments.

5.2 Methods

5.2.1 Sylgard® 527 curing and mechanical testing

The mechanical properties of Sylgard® 527 depend on the ratio of base (Sylgard® 527 Part A) and catalyst (Sylgard® 527 Part B) combined to form the mixture. After Sylgard® 527 is mixed, it can be cured at a temperature anywhere between -45 to 150℃ with a higher temperature increasing the rate at which it cures. For the presented in this work, Sylgard® 527 samples were cured at room temperature. Sylgard® 527 is a non-toxic substance; however, curing at high temperatures can release hazardous products such as formaldehyde.

Dynamic shear testing (DST) is a method used to determine the shear modulus of a material at specified frequencies (Figure 5.1). In these DST experiments, a small cylindrical sample is punched out and placed on the DST flexure, which is then displaced horizontally by a voice coil, causing the lower surface of the sample to undergo small horizontal oscillations. The voice coil is excited through a “chirp” sweeping through a frequency range of 0-100 Hz. Storage modulus can then be calculated through vibrating a material at different levels of compression. Samples for this study were ~15 mm in diameter and ~3-4 mm thick.

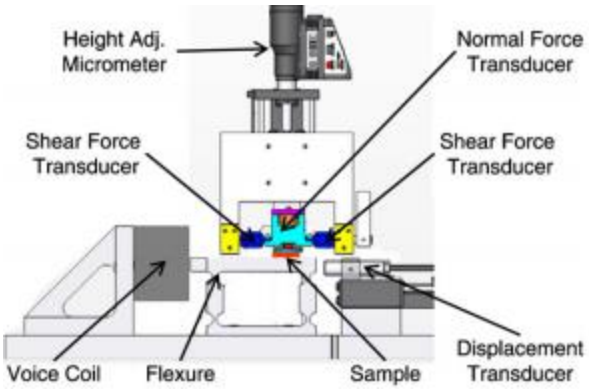

Figure 5.1: Dynamic Shear Testing (DST) apparatus. Samples were placed on a testing surface on the flexure and underwent small amplitude vibrations ranging from 0-100 Hz. Reprinted from [66]**.**

DST was performed on three 15 mm diameter cylindrical samples of Sylgard® 527 cured with the following ratios of base (A) to catalyst (B): 1) 1A : 1B, 2) 1A : 1.1B, and 3) 1A : 1.25B (Figure 5.2). These samples were tested to determine an appropriate mixture approximating the storage modulus of brain tissue at 50 Hz (~2-3 kPa) [66][35]. Testing Sylgard® 527 becomes increasingly difficult as the ratio of the base to the catalyst increases. The resulting cured Sylgard® 527 is very soft and adhesive, giving it difficult handling properties.

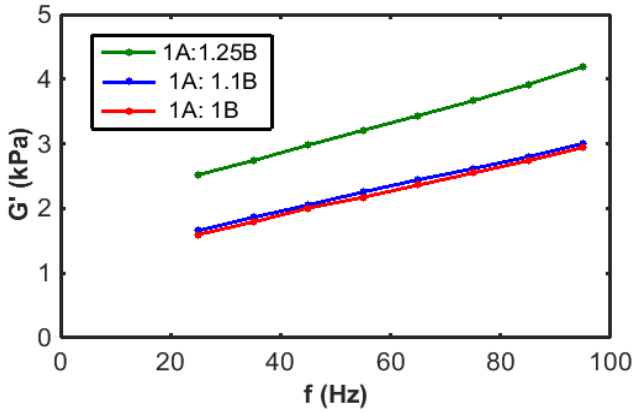

Figure 5.2: Frequency-dependent storage modulus of different ratios of Sylgard® 527 base (A) and catalyst (B) estimated from DST. Ratios tested include 1A:1.25B (green), 1A:1.1B (blue), and 1A:1B (red).

Sylgard® 527 samples created with a lower concentration of catalyst were estimated to have lower stiffness. The sample of 1:1.25 ratio of base to catalyst appeared to approximate previous values of brain tissue storage modulus at 50 Hz. As a result, a ratio of 1:1.25 Part A to Part B was chosen to construct the phantoms.

5.2.2 Cylindrical phantom fabrication

Homogeneous Cylindrical Phantom

Sylgard® 527 cylindrical phantoms were enclosed in an acrylic cylinder (McMaster-Carr Part No. 8486K581) with an inner diameter of 114 mm, an outer diameter of 127 mm, and a height of 152 mm. The bottom face was sealed using an acrylic disc with a thickness of 3.18 mm (McMaster-Carr Part No. 1221T75) that was adhered using SCIGRIP acrylic cement (McMaster-Carr Part No. 10308). The homogeneous cylindrical phantom was fabricated with a free surface near the top of the container (Figure 5.3). In order to keep a 1:1.25 base-catalyst ratio of the cured Sylgard® 527 contents, 645 grams of part A and 805 grams of part B were poured and mixed together. After stirring the mix thoroughly, the Sylgard® 527 was poured into one of the acrylic cylinders and placed into a vacuum chamber at a 75 cm Hg pressure difference for 4.5 hours. After degassing, the homogeneous phantom was set aside to cure at room temperature for ~1 week. Another acrylic disc was then glued to the top of the phantom, sealing the cylinder.

The homogeneous cylindrical phantom was later modified to have no free surface at the top of the phantom. This phantom was created by replacing the top disc with another disc with a filling hole and then pouring additional 1:1.25 ratio Sylgard® 527 on top of the original contents. Once the container was filled, the phantom was cured at room temperature for 5 days.

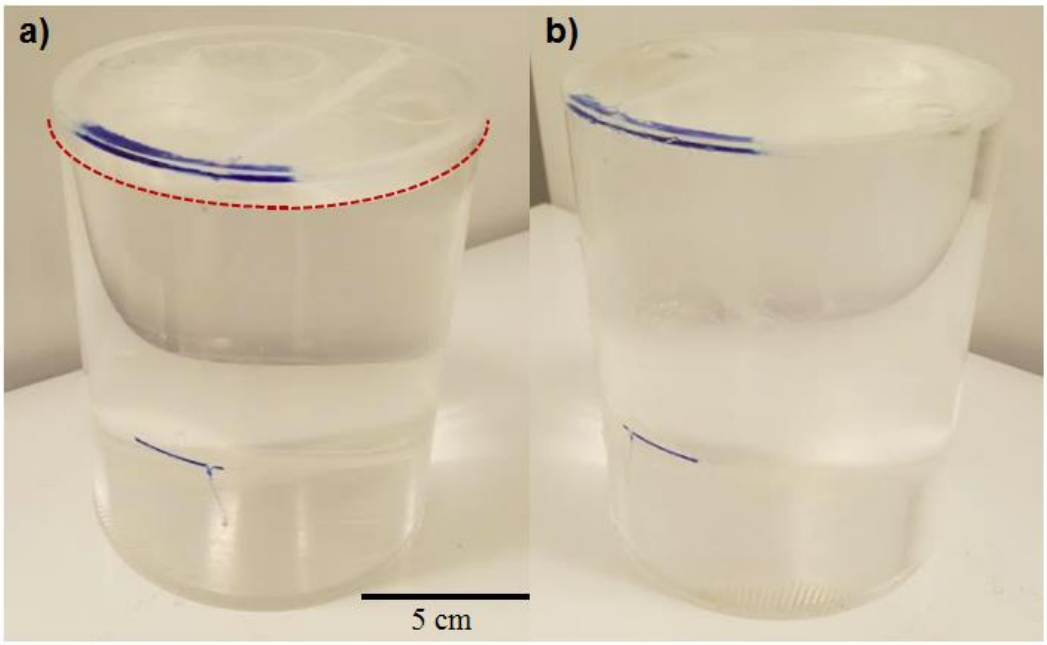

Figure 5.3: Completed homogenous cylindrical phantom fabricated with a 1:1.25 base-catalyst ratio. A) Homogeneous cylindrical phantom with a free surface at the top (dotted red). B) Same homogeneous cylindrical phantom with no free surface. The case is made of acrylic and is adhered together using acrylic cement.

Interfacial Cylindrical Phantom

The procedure for constructing the interface cylindrical phantom was similar to the homogenous phantom except it was fabricated with a smaller volume of cured Sylgard® 527 in order to accommodate a liquid interface of Sylgard® base (Part A).

For this phantom, 533 grams of part A and 667 grams of part B were used to create the contents. In order to have a smaller diameter cylinder for the cured Sylgard® 527 than the acrylic cylinder, the Sylgard® 527 was poured and cured inside of a cardboard shipping tube coated with Vaseline® to serve as a release agent. Due to the smaller diameter of the shipping tube, the mixture initially overflowed during degassing at 75 cm Hg. The pressure difference was thus

lowered and the overall degassing time was increased to compensate. The tube was left in the vacuum chamber at 60 cm Hg for 6.5 hours on the first day of degassing and at 72 cm Hg for 5 hours on the second day of degassing. After curing, the shipping tube was peeled away, leaving behind a cured Sylgard® 527 cylinder to be placed in the acrylic case. The acrylic case was assembled with a single lid placed on the bottom face, leaving the top open. The interface cylindrical phantom case was modified with a removable lid of larger diameter. On the open side of the assembly, a removable lid was constructed using two more acrylic disks and plastic screws. To accomplish this, a 114 mm diameter hole was cut into a 152 mm diameter acrylic disk with a thickness of 3.18 mm. Next, eight threaded holes were made in the disk at a radius of 69.9 mm and the disk was adhered to the phantom using acrylic cement. An identical disk was made, with the exception of omitting the 114 mm diameter hole, and was attached to the other disk using plastic screws.

The cured Sylgard® 527 cylinder was then centered and attached to the bottom of the acrylic case with epoxy. Due to the softness of the cured cylinder, flexible plastic tubes (drinking straws) were inserted at 6 locations which maintained even spacing between the cured Sylgard® 527 and case. Interface fluid was then poured into the phantom and the lid was sealed. (Figure 5.4b). The O-ring was compressed when the screws were tightened, preventing any exposure to air or leakage of interface fluid.

Initially, water was used as the interface fluid in order to simulate cerebrospinal fluid (CSF). After preliminary testing, however, it was found that a substantial chemical shift artifact occurred during the EPI MRE sequence due to the vastly different T1 signal from the cured Sylgard® 527 relative to water (Figure 5.4c). As a result, the water interface was replaced with liquid Sylgard® 527 base (Part A). The liquid Sylgard® 527 base could still be distinguished from the cured cylinder due to its higher MRE signal magnitude, but the chemical shift was eliminated (Figure 5.4d).

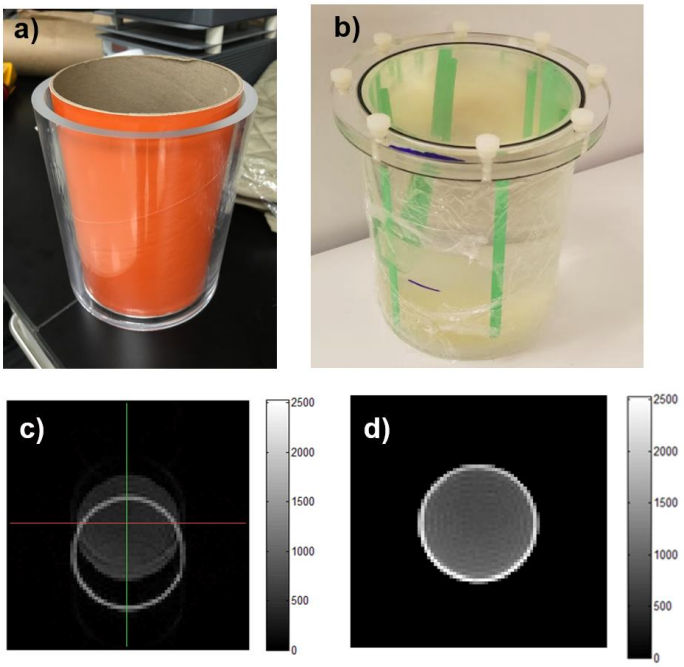

<u>Figure 5.4:</u> Interface phantom fabrication and preliminary testing. a) A shipping tube with a smaller diameter than the acrylic case was used to create inner Sylgard® contents. b) Assembled interface phantom with larger diameter, removable acrylic lid and O-ring to prevent leaking. c) Large chemical shift artifact present in MRE magnitude image of interface phantom with water boundary. d) Interface phantom with liquid Sylgard® Part A appears with high signal magnitude and does not cause a chemical shift.

Membranous Cylindrical Phantom

The cylindrical, membrane phantom was created in a similar fashion to the cylindrical, interface phantom. The primary difference during phantom fabrication was the inclusion of a 3D printed polyvinyl alcohol (PVA) "falx" membrane attached to inside of the acrylic case lid. In order to easily introduce this membrane into the cured Sylgard® 527 phantom contents, a 3D printed polyvinyl alcohol (PVA) insert was introduced into the shipping tube mold during curing (Figure 5.5a). This insert was designed with the same dimensions as the final PVA falx so that it could serve as a placeholder during curing. After curing, the cardboard was peeled away leaving a cylinder of cured Sylgard® 527 with a plastic insert. The plastic insert was removed and the cured cylinder was adhered to the bottom of the acrylic casing using epoxy. A PVA rectangular insert was made to represent the falx and was adhered to the top acrylic disk using epoxy. Next, the phantom was filled with Sylgard® 527 Part A to represent an interface. Six, plastic straws were placed to maintain an even spacing between the cured, Sylgard® 527 cylinder and the acrylic casing. Finally, the lid was placed so that the PVA insert filled the premade gap and the screws were tightened to seal the phantom (Figure 5.5b).

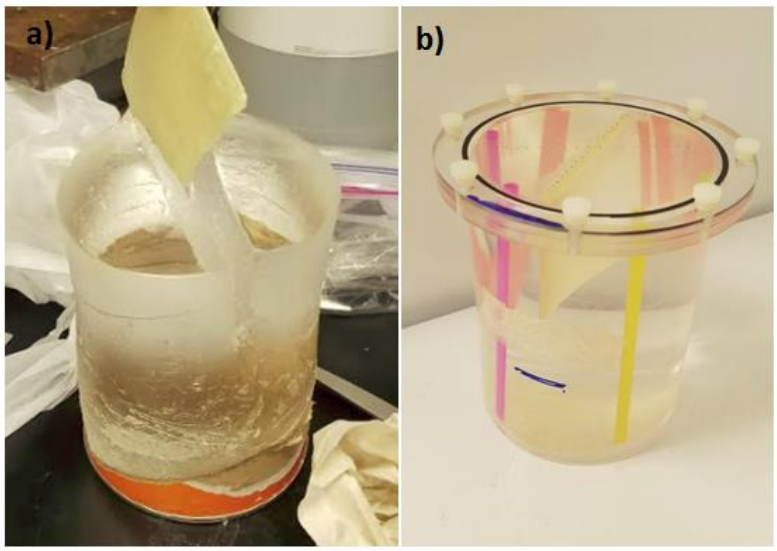

Figure 5.5: Membranous cylindrical phantom fabrication. a) A 3D printed polyvinyl alcohol divider was introduced into the Sylgard® 527 contents during curing to serve as a placeholder for the falx. b) Completed membranous cylindrical phantom with removable acrylic lid and the PVA membrane adhered to the underside of the lid.

5.2.3 Cranial phantom fabrication

Cadaveric Anatomical Data Segmentation

In order to create an anatomically accurate cranial phantom, a T1 MPRAGE of a cadaveric specimen was provided by collaborators at the Henry Jackson Foundation. Cadaveric anatomical data was segmented to identify the total brain volume and its surrounding cranial bone (anterior facial features were abraded during this process to simplify later 3D printing) [67]. Both dural membranes, the falx cerebri and tentorium cerebelli, were then manually segmented using ITK-SNAP [77], [78] (Figure 5.6). Printable stereolithography (.stl) models of the skull, brain, and dural membranes were then created and smoothed in Slicer3D, an open-source, medical image processing software [79] (Figure 5.7).

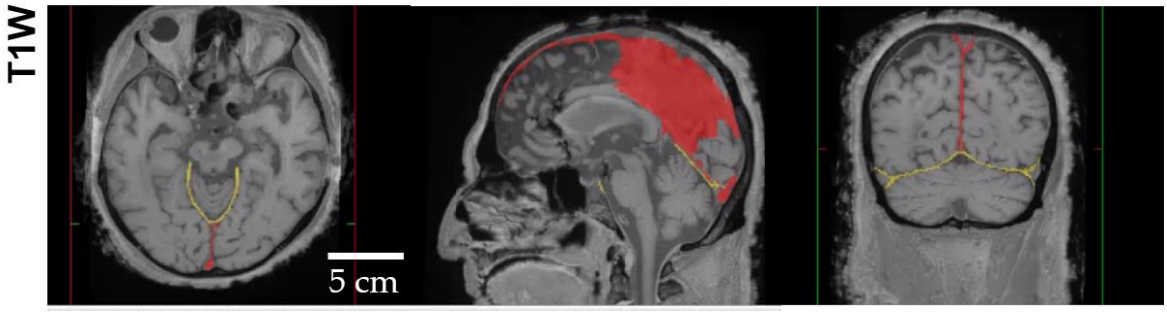

Figure 5.6: T1W anatomical images of cadaveric head specimen processed in ITK-SNAP. Voxels corresponding to approximate location of the falx cerebri (red) are found through boundary labeling between the right and left hemispheres of the cerebrum. Tentorium cerebelli (yellow) is identified as the boundary between cerebrum and cerebellum.

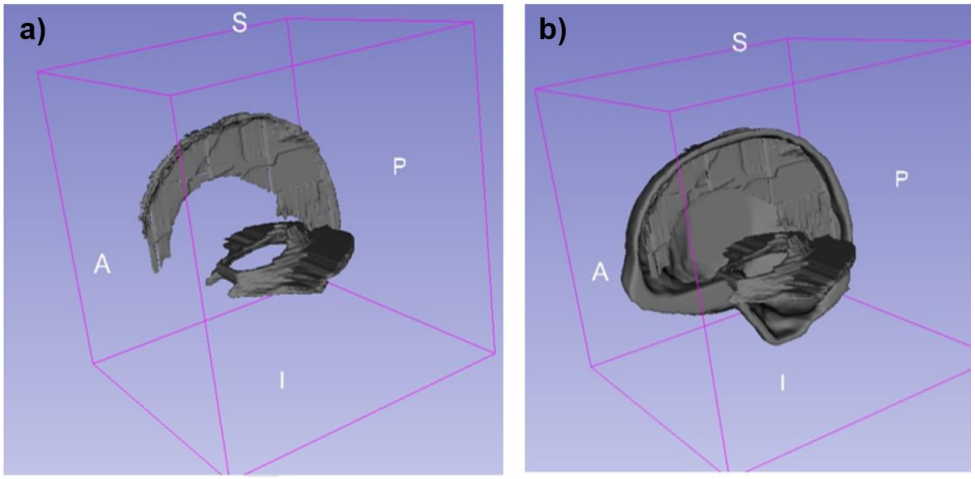

Figure 5.7: Physical model creation in Slicer3D. a) Falx cerebri and tentorium cerebelli identified in Figure 5.6 are rendered and smoothed before exporting. b) Dural membranes are anchored to the inside of a sagittal sliced skull model.

Homogenous Cranial Phantom

The homogeneous cranial phantom was constructed by separately fabricating superior and inferior skull halves from Smooth-Cast® 380 resin and making a brain from 1:1.25 base-catalyst ratio of Sylgard® 527. A negative-mold of a cadaveric brain was constructed in Slicer3D and Blender then 3D printed with polylactic acid (PLA) filament (Figure 5.8b-c). This mold was printed in two halves, one containing the superior region and the other containing the inferior region. A hole with a diameter of 9 mm was drilled in the superior half to allow for the filling of the mold. After coating the inside of each half with petroleum jelly (to serve as a release agent), the two halves were adjoined and sealed with silicone sealant. After giving the sealant sufficient time to set, a volume of approximately 1250 cm^3 Sylgard® 527 (1:1.25 ratio) was poured into the mold through the 9 mm hole. Next, it was set aside for approximately one week to cure at room temperature. Following the curing process, the two halves were disjointed by cutting through the silicone seal and the cured Sylgard® 527 brain was removed.

Each half of the resin skull had four flanges so that the two halves could be connected using plastic screws and nuts. The superior skull half also had a hole with a diameter of 8 mm drilled into the top face. Once the brain was placed inside the halves, the screws were put in place and epoxy was used to fill the gaps between the two halves of the resin skull. In order to fill the space between the cured Sylgard® 527 brain and resin skull, additional 1:1.25 base-catalyst ratio Sylgard® 527 was poured into the skull and allowed to cure for an additional five days.

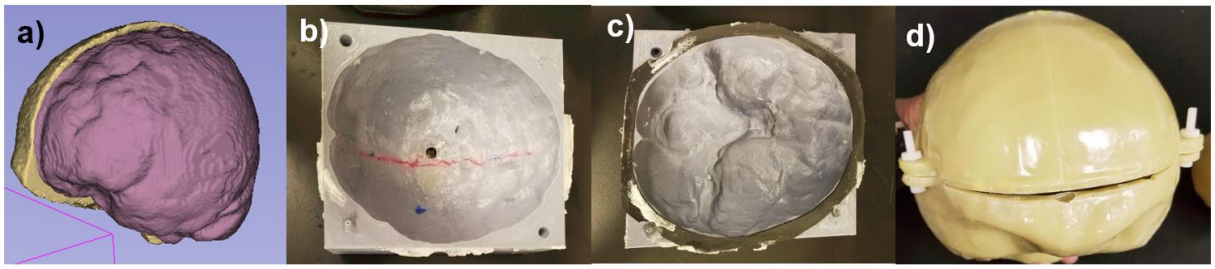

Figure 5.8: Fabrication of the homogeneous cranial phantom. a) Rendering of the expanded brain volume within the resin skull in Slicer3D (skull is split into lateral halves for visibility). b) Top half of 3D printed brain mold with a filling hole on the top face. c) Bottom half of the 3D printed brain mold has inferior anatomical features to shape cerebellum and midbrain structures. d) Completed homogeneous cranial phantom has flanges to fasten together both halves. Space between top and bottom skull halves is later filled with epoxy.

Interfacial Cranial Phantom

The Sylgard® 527 brain used in the cranial, interface phantom was created in the same 3D printed, PLA negative-mold as the cranial, homogenous phantom (Figure 5.8b-c). The process for making the cured Sylgard® 527 brain was the same. After the brain was made, the Sylgard® 527 brain was placed in a resin skull identical to the cranial, homogenous phantom. In addition, a rubber gasket was cut, placed, and adhered using epoxy between the two resin skull halves to prevent leaking of any interface fluid. After the Sylgard® 527 brain was placed and sealed within the resin skull, Sylgard® 527 part A was poured into the filling hole (Figure 5.9b). Once the skull was completely filled with the Sylgard® 527 brain and the interface fluid, rubber corks were used to seal the holes at the top.

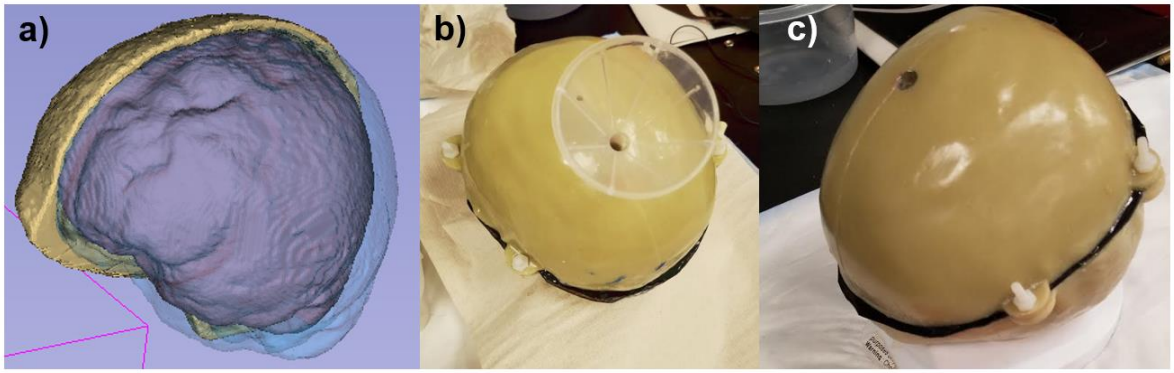

Figure 5.9: Fabrication of the interface cranial phantom. a) Rendering of the normal brain volume with a fluid interface separating it from the resin skull. b) After placing the cured Sylgard® brain into the resin skull, a funnel is placed into the filling hole and liquid Sylgard® 527 part A is poured in to fill the remaining space. c) Completed interface phantom with a rubber gasket separating both skull halves to prevent leaking.

Membranous Cranial Phantom

For the final cranial phantom, the Sylgard® 527 brain was again created with a negative mold, however membrane inserts, or placeholders for the falx cerebri and tentorium cerebelli were also included (Figure 5.10). The falx insert was 3D printed using PLA filament while the tentorium insert was 3D printed with PVA. Since the membranes extrude past the brain volume and connect to the skull, the inserts were scaled down to 85% volume so that they could fit inside the negative-mold. These inserts were adhered to the brain mold using epoxy before the filling process. After the Sylgard® 527 brain cured, the inserts were removed and full-size falx and tentorium membranes were 3D printed with PVA and inserted into the Sylgard® 527 brain.

As with the interfacial cranial phantom, the membranous cranial phantom used a resin skull with the same holes drilled into the superior half of the skull, another gasket separating the two halves, and four flanges on each half of the skull. The PVA membranes were rigidly attached to

the skull using epoxy (Figure 5.10e-f). After the membranes and Sylgard® 527 brain were positioned, the resin skull was sealed using epoxy and the remaining volume inside the resin skull was filled with Sylgard® 527 part A.

Table 5.1 contains the mass of each of the cylindrical and cranial phantoms created in this section.

	Homogeneous Cylinder (FS)	**Interface Cylinder**	**Membranous Cylinder**	**Homogeneous Cylinder (NFS)**	**Homogeneous Cranial**	**Interfacial Cranial**	**Membranous Cranial**
Mass (g)	1890	2160	2200	1990	2320	2310	2330

Table 5.1: Mass of the four cylindrical and three cranial phantoms fabricated in Section 5.2.3. FS: Free surface, NFS: No Free Surface.

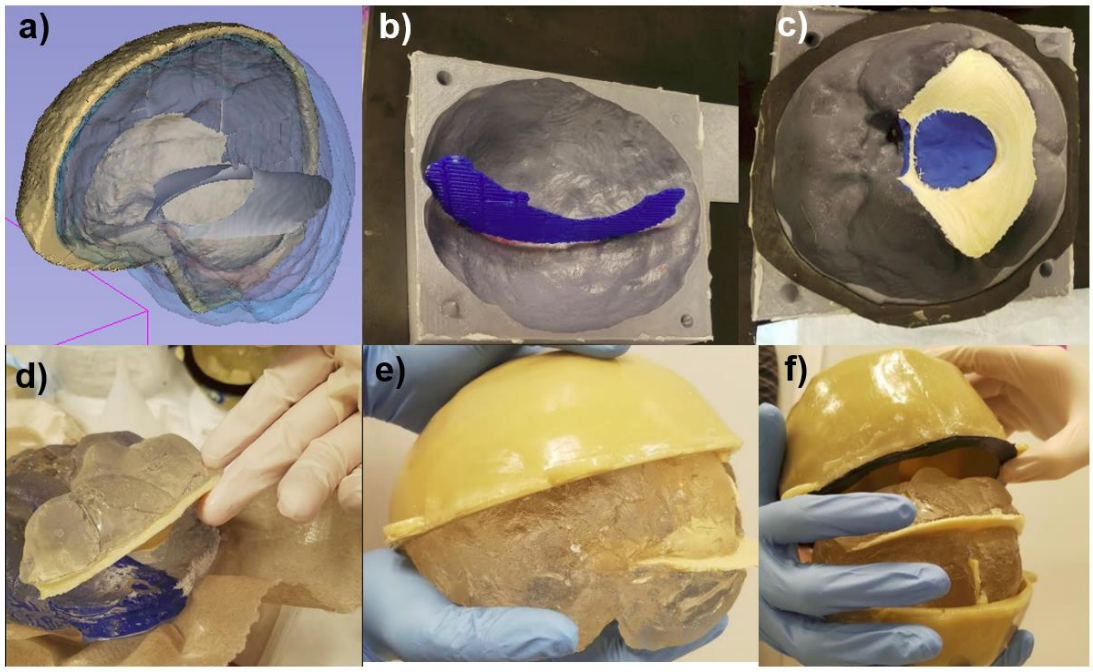

Figure 5.10: Fabrication of the membranous cranial phantom. a) Rendering of the falx and tentorium dural membranes extruding into the Sylgard® 527 brain from the resin skull. b) Top half of the brain mold contains a 3D printed PLA falx to serve as a placeholder for later introduction of the full-sized falx. c) Bottom half of the brain mold contains a 3D printed PVA tentorium with the notch filled in with modeling clay. d) After curing, the placeholder membranes are removed, leaving space for the full sized, PVA membranes. e) The top half, with the PVA falx epoxied to the inside of the skull, is placed onto the cured Sylgard® 527 brain. The full size tentorium has already been placed within the Sylgard® 527 brain. f) The bottom of the brain is then placed into the skull bottom half. The full sized tentorium is fixed to the resin skull using epoxy.

5.2.4 MRE imaging procedures and instrumentation

MRE testing was performed on all six phantoms on a Siemens Trio® 3T MRI scanner located at the Center for Clinical Imaging Research at Washington University in St. Louis. External vibrations were induced at a frequency of 50 Hz through a commercially available system (Resoundant^{TM}, Rochester, MN) using a "pillow" actuator (Mayo Clinic, Rochester, MN) positioned at the back of the cylinder/cranial phantom (Figure 5.11). The phantoms were positioned within a Siemens 12 channel head coil. The phantom posterior rested on the inflatable

portion of the actuator and was stabilized by padding placed laterally. External case or skull kinematics were estimated using three MRI-safe, tri-axial accelerometers (TSD109C2-MRI, BIOPAC©, Goleta, CA) embedded in a mouth guard array (MGA) that was adhered to the phantom face with a 3D-printed interface. Resoundant^{TM} amplitudes of 5% and 7% were used for MRE testing of the cylindrical and cranial phantoms, respectively. The actuation level was chosen to provide similar acceleration amplitudes (~1.0-1.5 m/s^2) between the cylindrical and cranial phantoms.

MRE data was acquired from an echo-planar imaging (EPI) sequence. Imaging parameters included 3 MEG directions acquired at differing MEG strengths: 7 and 26 mT/m, 8 phase offsets, and 24 axial slices with 3 mm isotropic voxels. While the accelerometers are MRI-safe, they can induce imaging artifacts in the field of view, thus a truncated, six-slice EPI sequence with duration of approximately 40s was performed in order to estimate skull motion during MRE testing. After this scan, the accelerometers and MGA were removed while the phantom remained in the head coil. After removal, T1 and T2 weighted anatomical sequences with 0.9 mm isotropic voxel resolution were performed followed by two 24 slice EPI-MRE scans at MEG strengths of 7 and 26 mT/m.

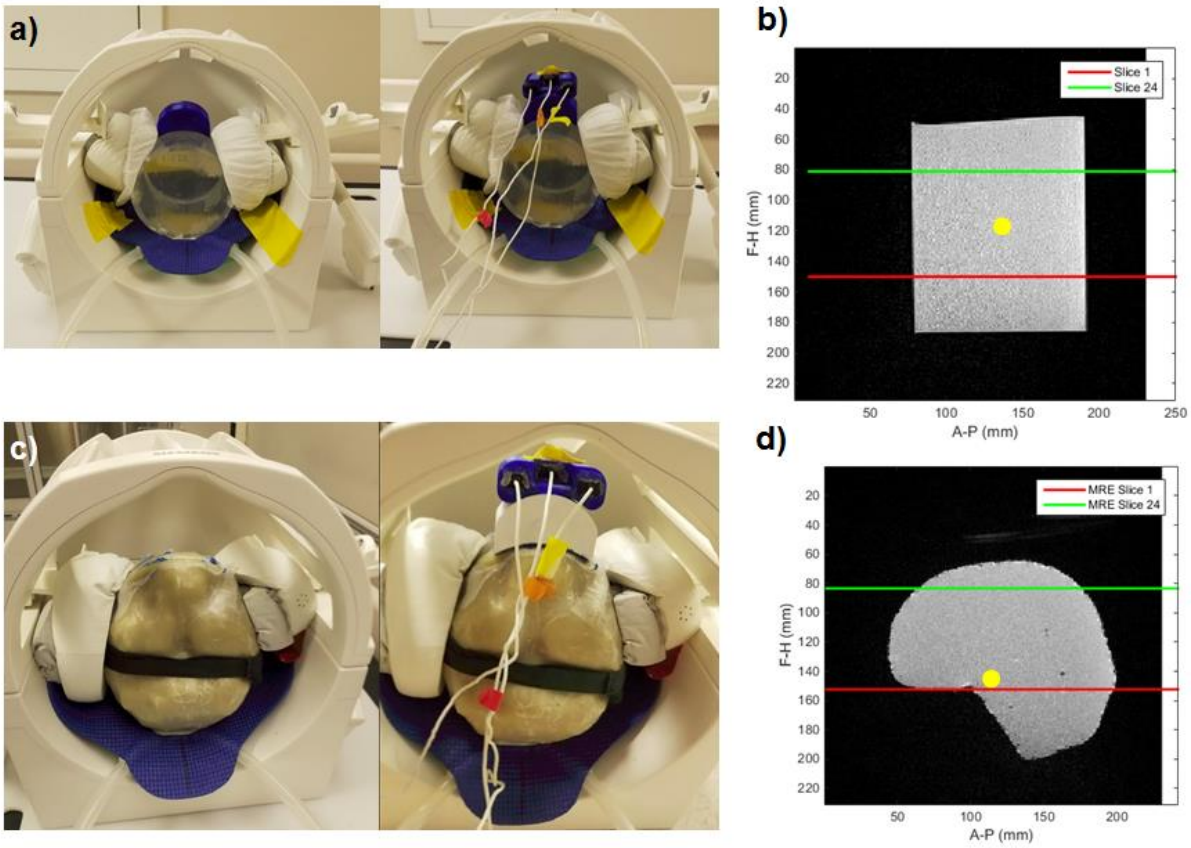

Figure 5.11: MRE and accelerometer data collection for the cylindrical and cranial phantoms. a) The cylindrical phantom is placed within a 12 channel head coil with the pillow actuator placed at the phantom posterior. A 3D printed accelerometer array holding the three tri-axial accelerometers is anchored to the anterior face of the phantom. Padding is placed laterally in order to stabilize the phantom. b) Sagittal T1-weighted image of the homogeneous cylindrical phantom showing the 24-slice MRE volume. Approximate cylindrical phantom origin is highlighted by the yellow circle. c) Similar to the cylindrical phantom, the cranial phantom is placed within the head coil with the pillow actuator positioned at the skull posterior. The accelerometer array is attached to the anterior of the cranial phantom with mounting tape and modeling clay. d) A sagittal T1-weighted image of the homogeneous cranial phantom shows the 24 MRE slices acquired during scanning. Approximate cranial phantom origin is highlighted by the yellow circle.

As shown previously, the liquid Sylgard® 527 part A interface appears with high MRE signal magnitude. A T2-weighted scan can also provide high contrast between the liquid interface and cured contents (Figure 5.12). In contrast, the PVA membranes in both the cylindrical and cranial phantoms have very low signal and thus appear dark in both anatomical and MRE images.

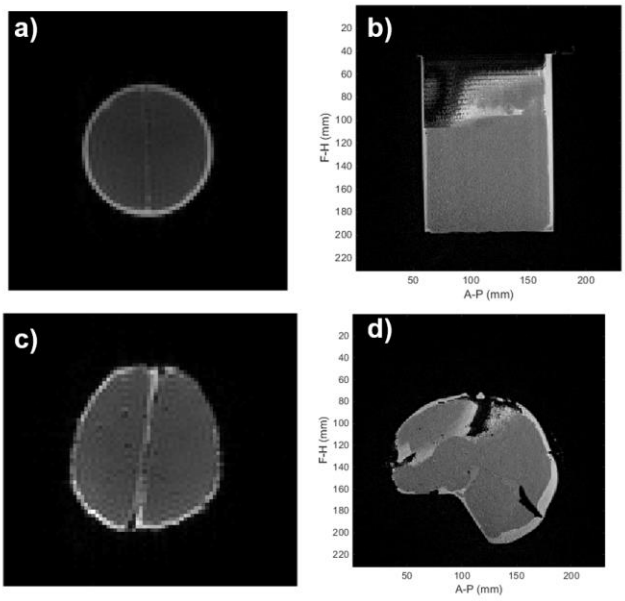

Figure 5.12: T2-weighted MR images of the cylindrical membranous phantom and cranial membranous phantom. a) Transverse slice of the cylindrical membranous phantom shows the liquid Sylgard® 527 part A interface with high signal. b) Sagittal slice of the cylindrical membranous phantom demonstrates the relative location of the PVA falx. c) Transverse slice of the cranial membranous phantom shows the liquid interface appearing with higher signal than the cured Sylgard® 527 brain. d) Sagittal slice shows the PVA falx and tentorium appear with very low signal compared to the cured and liquid Sylgard® 527.

5.2.5 Finite element modeling of Sylgard® 527 cylindrical phantoms

Finite element (FE) simulations (COMSOL^{TM} 5.2a, Burlington, MA) of the cylindrical phantom MRE experiments were performed by creating 3D models of the Sylgard® 527 contents and exciting them with AP harmonic motion (20 μm, 50 Hz). FE simulations for the three cylindrical phantom cases are shown in Figure 5.13. Cured Sylgard® 527 (brain tissue surrogate) was modeled with a storage modulus (G') of 3 kPa and loss factor (η) of 0.6. Sylgard® 527 part A (cerebrospinal fluid surrogate) was modeled with G' = 1 Pa and η = 100. The PVA membrane (falx surrogate) was modeled with G' = 1.67 MPa and η = 0. Mesh size elements were set to "Fine".

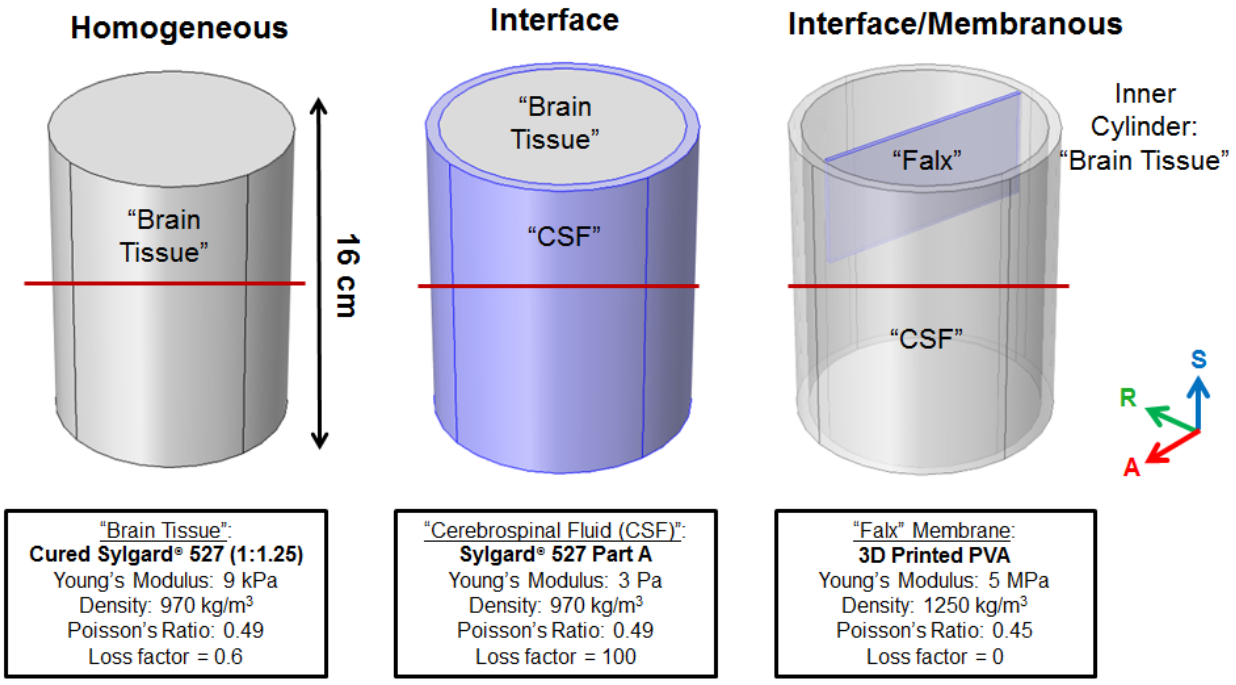

Figure 5.13: Finite Element (FE) models of the three cylindrical phantoms created in COMSOL™. Material properties are listed for the constituent materials – Cured Sylgard® 527 ("Brain tissue"), Sylgard® 527 Part A ("Cerebrospinal Fluid"), and 3D Printed PVA ("Falx"). Central axial slice corresponding to MRE slice 10 is outlined in red.

5.2.6 Rigid-body and wave displacement estimation in Sylgard® 527 cylindrical and cranial phantoms

Case and skull kinematics for the cylindrical and cranial phantoms, respectively, were estimated from accelerometer recordings using the methods detailed in previous chapters. For this study, displacement conversions were 10.47 μm (7 mT/m) and 2.82 μm (26 mT/m) per radian of MRE phase contrast. Since MRE phase contrast is a measure of total oscillatory displacement ($\boldsymbol{u}$) that captures the effects of both rigid-body motion and wave motion, rigid-body motion must be isolated and removed to capture wave displacement. Estimates of Sylgard® 527 displacement were calculated using MRE data at 26 mT/m.

As with the previous phantom studies, external displacements were reconstructed from accelerometer data at four discrete points on the cylindrical case and resin skull: anterior (A), right (R), left (L), and posterior (P). Reconstruction points and the phantom origin were located from T_1-weighted scans. The coordinate system origin for the cylindrical phantom was approximated as the center of the Sylgard® 527 cylinder volume (Figure 5.11b) while the origin for the cranial phantom was approximated at a location close to the posterior clinoid process in a human skull (Figure 5.11d). Estimates of external displacement at four material points (reconstructed from accelerometer measurements) were compared to analogous estimates of displacement at neighboring material points in the Sylgard® 527 contents (estimated from MRE measurements). Due to field inhomogeneity artifact in both the brain and scalp at the bottom of the slice volume, only the central 20 slices were used for analysis

In addition to estimating wave displacement, curl (**Γ**) was estimated through differentiation of the displacement field to provide a separate estimate of the contribution of shear waves. Strain magnitudes resulting from wave propagation are reported as octahedral shear strain (ε_s) [68].

Shear wave propagation energy can be measured by calculating the Poynting vector from the complex MRE displacement field. Poynting vectors describe the direction and rate of energy-flux crossing a wave surface [80], [81]. Here, the Poynting vector P_i is calculated as:

$$P_i = -\sigma_{ij}\dot{u}_j \tag{5.1}$$

With stress $\boldsymbol{\sigma}$ and velocity $\dot{\boldsymbol{u}}$ at each voxel. While these two quantities are not directly measured through MRE, they can be approximated with the appropriate assumptions. By assuming an isotropic, linear elastic medium for this analysis, I was able to relate deviatoric shear stress, $\hat{\boldsymbol{\sigma}}$, and deviatoric shear strain, $\hat{\boldsymbol{\varepsilon}}$, through the complex shear modulus, G^*:

$$\hat{\sigma}_{ij} = 2G^*\hat{\varepsilon}_{ij} \tag{5.2}$$

where deviatoric shear strain, $\hat{\boldsymbol{\varepsilon}}$ is calculated as:

$$\hat{\varepsilon}_{ij} = \varepsilon_{ij} - \varepsilon_{kk}\delta_{ij}/3 \tag{5.3}$$

which enables us to approximate a scaled Poynting vector as:

$$P_i = -2G^*\hat{\varepsilon}_{ij}\dot{u}_j \tag{5.4}$$

The Poynting vector approximated in this way is not calculated in units of energy-flux, but is instead scaled by the shear modulus.

Shear wave propagation was also measured through directional filtering of the propagation direction using methods described in [45]. Here, the filtered direction $\vec{\boldsymbol{d}}^{(i)}$ at each voxel is found through directional filtering of each component of curl Γ_i for each phantom. A weighted

propagation direction, $\vec{\boldsymbol{n}}$, at each voxel was then calculated by weighting each propagation direction by the sum of the squares of the corresponding component of curl. This process can be described by the following equations:

$$\vec{\boldsymbol{n}} = \sum_{\boldsymbol{i=1}}^{\boldsymbol{3}} W_i \vec{\boldsymbol{d}}^{(\boldsymbol{i})} \tag{5.5}$$

$$W_i = \sum_{\boldsymbol{Volume}} |\Gamma_i|^2 \tag{5.6}$$

5.3 Results

5.3.1 Comparison of rigid-body motion, wave motion, and octahedral shear strain in cylindrical phantoms

The three components of rigid-body translation ($\bar{u}_x^O$, $\bar{u}_y^O$, and $\bar{u}_z^O$) and rotation ($\theta_x, \theta_y,$ and θ_z) at the phantom origin measured by MRE for the contents of the homogeneous (with a free surface), interfacial, and membranous cylindrical phantoms are compared with estimates of case translation and rotation estimated from accelerometers (Figure 5.14). In these experiments, the amplitude of translational components appears to have stronger agreement between the case and contents compared to the amplitude of rotational components, particularly in the interfacial and membranous cylindrical phantoms.

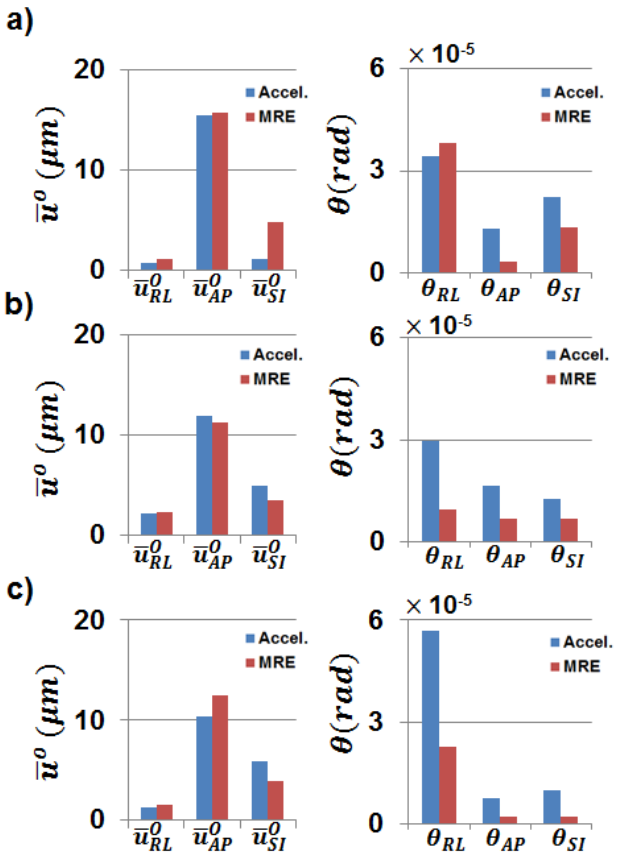

Figure 5.14: Comparison of RMS amplitude of rigid-body motion translation and rotation at the origin for the a) homogeneous cylindrical phantom with a free surface, b) interfacial cylindrical phantom, and c) membranous cylindrical phantom. Rigid-body displacement components are estimated for the case from accelerometers (blue) and for the Sylgard® 527 contents estimated from MRE (red).

The temporal phase delay between case and Sylgard® 527 motion ($\boldsymbol{\phi_{C/S}}$) for the homogeneous (with a free surface), interfacial, and membranous cylindrical phantoms are listed in Table 5.2. The calculated temporal phase delay was close to 0 or 2π for all three phantoms. Note that the relative phase in these phantoms is difficult to determine with the current level of precision.

	$Hom.Cyl$ $\phi_{C/S}$ (rad)	$Int.Cyl$ $\phi_{C/S}$ (rad)	$Mem.Cyl$ $\phi_{C/S}$ (rad)
Ant.	**0.04**	**6.25**	**6.26**
Right	**0.04**	**6.15**	**6.13**
Left	**0.08**	**0.03**	**6.20**
Post.	**0.08**	**6.22**	**6.08**

Table 5.2: Temporal phase shift, $\phi_{C/S}$, between harmonic motion of the case (estimated by accelerometers and Sylgard® 527 (estimated by MRE) for the homogeneous cylindrical phantom (with a free surface), interfacial cylindrical phantom, and membranous cylindrical phantom. Results are shown for each of the four quadrants.

Following rigid-body motion isolation and removal, wave displacement approximating Sylgard® 527 deformation in the three cylindrical phantoms can be calculated (Figure 5.15). For each cylinder, I calculated three components of wave displacement: right-left (RL), anterior-posterior (AP), and superior-inferior (SI). In the homogeneous case with a free surface, where the Sylgard® contents were attached directly to the acrylic case, the amplitude of wave displacement was found to be higher than in the interfacial and membranous phantoms. In the membranous phantom, however, higher amplitude shear waves were found in regions containing the PVA falx. In contrast, low wave displacement amplitudes were found in the interface cylindrical phantom. For all three phantoms, the amplitude of rigid-body displacement was larger than wave displacement amplitude, which is in contrast to the glycerol-gelatin phantom tested in Chapter 2.

Figure 5.16 provides comparison of wave displacement for each phantom scaled by case displacements estimated by accelerometers.

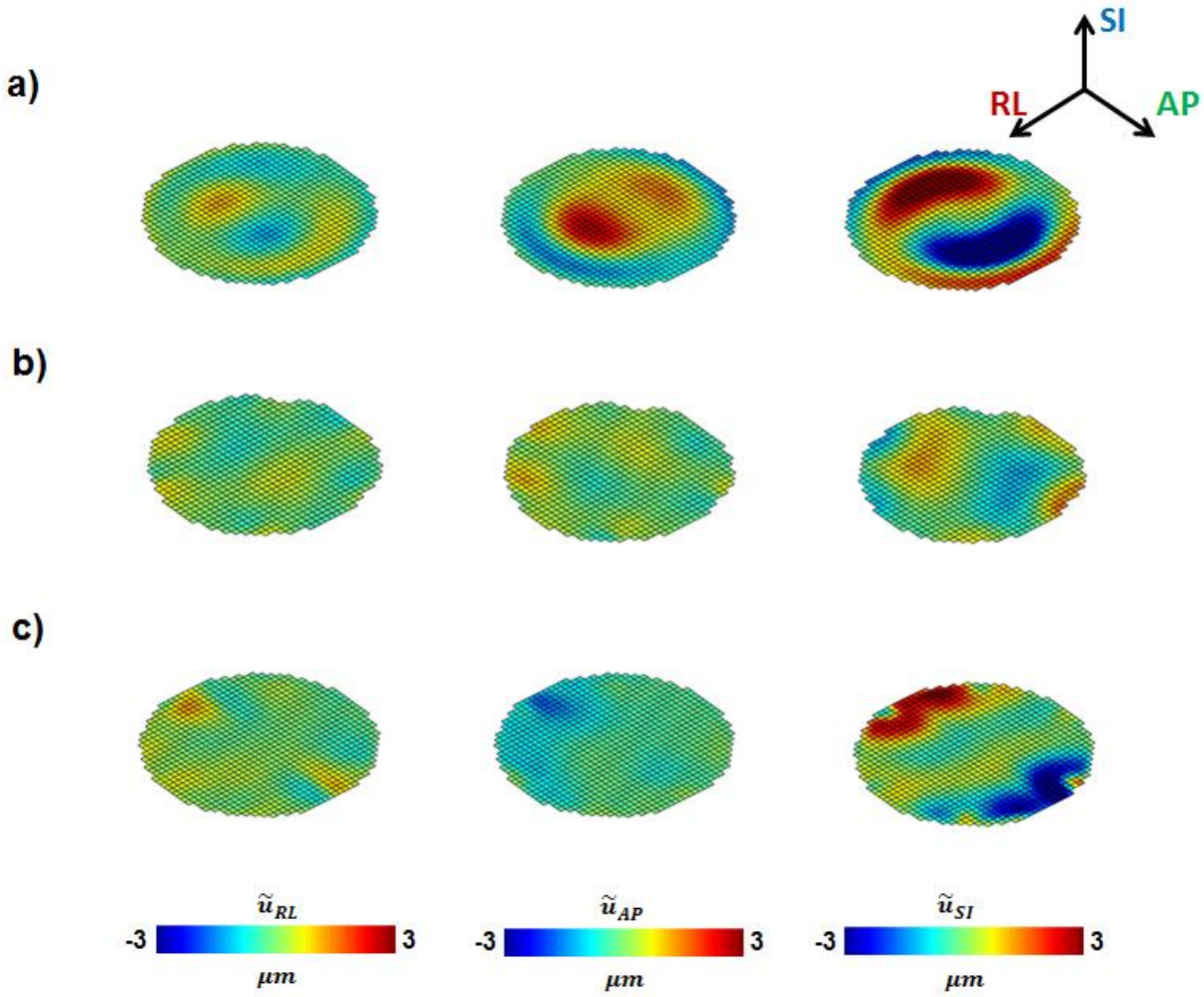

Figure 5.15: RL, AP, and SI components of the harmonic wave displacement (real part) of axial slice 10 in the a) homogeneous cylindrical phantom with a free surface, b) interfacial cylindrical phantom, and c) membranous cylindrical phantom

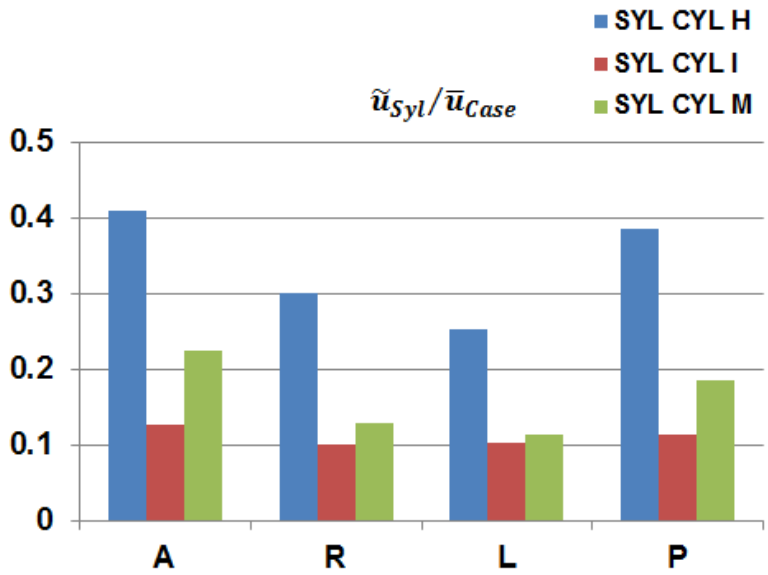

Figure 5.16: Wave displacement ($\tilde{u}$), estimated by MRE, scaled by case rigid-body displacement ($\bar{u}$) estimated from accelerometers. Mean values are shown in the anterior (A), right (R), left (L), and posterior (P) quadrants of the homogeneous cylindrical phantom with a free surface, interfacial cylindrical phantom, and membranous cylindrical phantom.

Octahedral shear strain estimates are shown in Figure 5.17. Strain amplitudes were higher in the homogeneous cylinder than in the interface phantom. In the membranous phantom, larger strain patterns emerge close to the embedded falx membrane.

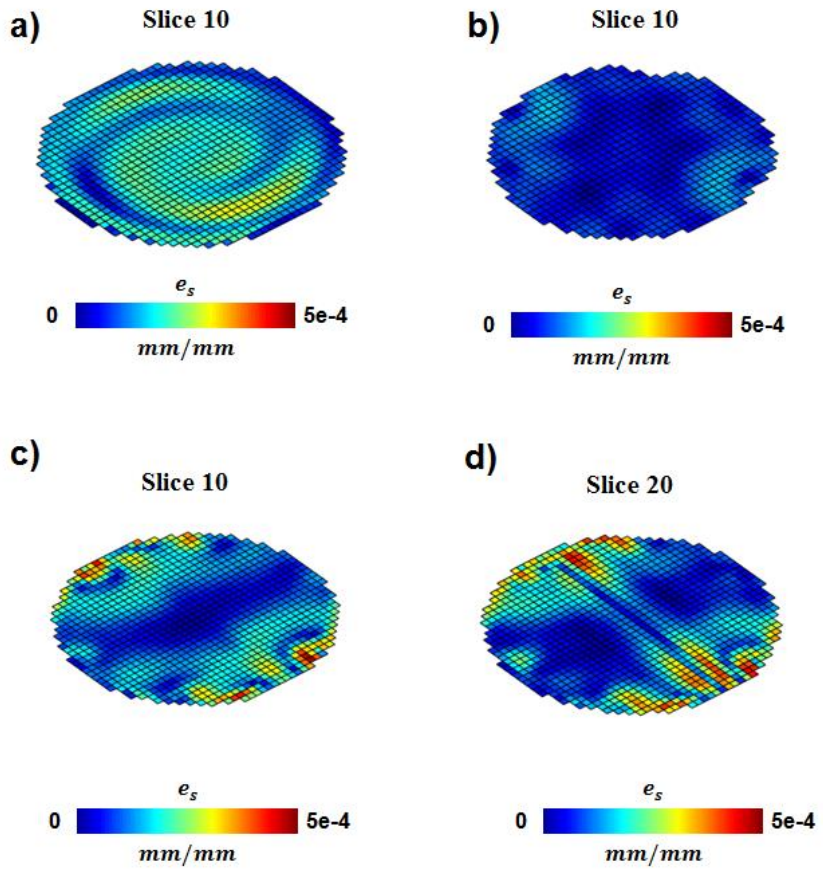

Figure 5.17: Octahedral shear strain estimates for axial slice 10 of the a) homogeneous cylindrical phantom, b) interfacial cylindrical phantom, and c) membranous cylindrical phantom and d) axial slice 20 of the membranous cylindrical phantom.

Removing the free surface in the second homogeneous cylindrical phantom resulted in much lower wave displacement and strain amplitude estimates from MRE (Figure 5.18).

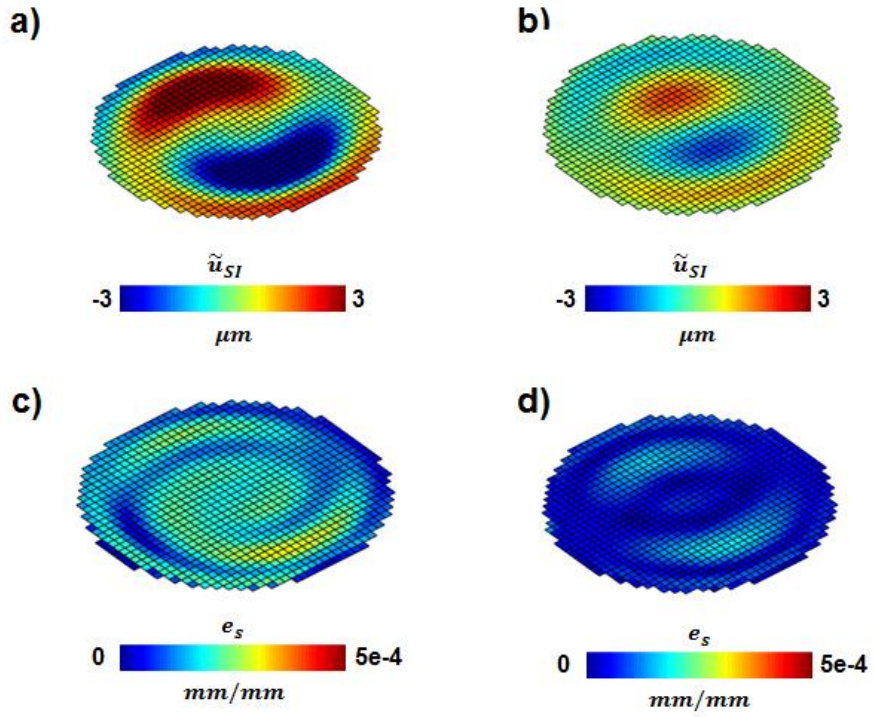

Figure 5.18: SI component of harmonic wave displacement (real part) for the homogeneous cylindrical phantom a) with a free surface and b) with no free surface. Octahedral shear strain estimates for homogeneous cylindrical phantom c) with a free surface and d) with no free surface

5.3.2 Wave motion estimates from finite element simulations of cylindrical phantoms

Experimental and simulated displacement fields due to wave motion were compared between each of the four cylindrical phantoms (Figure 5.19). In the experimental and simulated results, the homogeneous phantom with a free surface exhibited high SI wave displacement amplitude, compared to the other three cylindrical phantoms. The homogeneous cylindrical phantom with no free surface and the interfacial cylindrical phantoms had relatively low amplitude wave

motion. Experimental and simulated results for the membranous cylindrical phantom indicate higher displacement amplitudes near the embedded falx membrane.

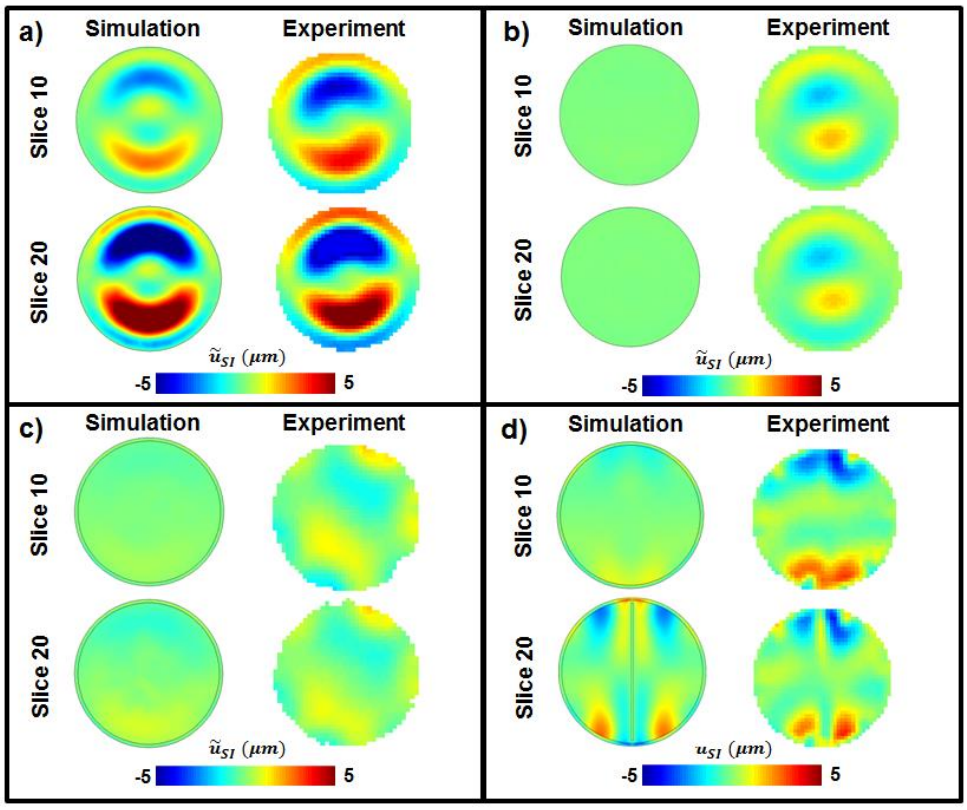

Figure 5.19: Harmonic displacement fields (real part of SI component) in finite element (FE) simulation and experiment from axial slice 10 and 20 of the a) homogeneous cylindrical phantom, b) homogeneous cylindrical phantom with no free surface, c) interface cylindrical phantom, and d) membranous cylindrical phantom

5.3.3 Comparison of rigid-body motion, wave motion, and octahedral shear strain in cranial phantoms

The three components of rigid-body translation ($\bar{u}_x^o$, $\bar{u}_y^o$, and $\bar{u}_z^o$) and rotation ($\theta_x, \theta_y,$ and θ_z) at the phantom origin measured by MRE for the contents of the homogeneous, interfacial, and membranous cranial phantoms are compared with estimates of skull translation and rotation

estimated from accelerometers (Figure 5.20). In these experiments, the amplitude of translational components appears to have stronger agreement between the case and contents compared to the amplitude of rotational components, particularly in the interfacial and membranous cylindrical phantoms.

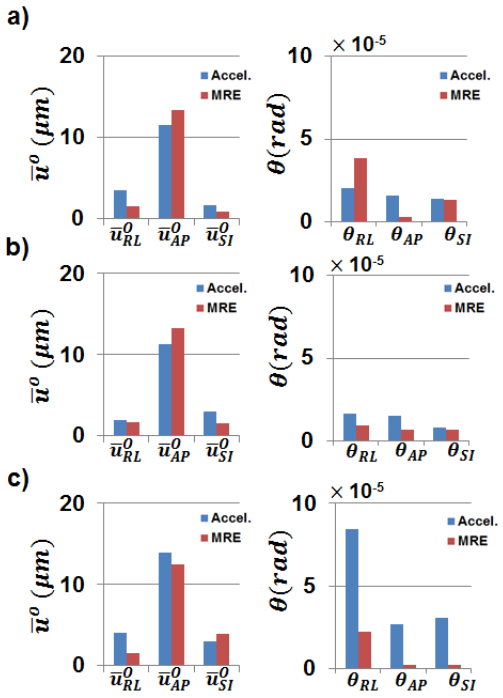

Figure 5.20: Comparison of RMS amplitude of rigid-body motion translation and rotation at the origin for the a) homogeneous cranial phantom, b) interfacial cranial phantom, and c) membranous cranial phantom. Rigid-body displacement components are estimated for the resin skull from accelerometers (blue) and for the Sylgard® 527 brain estimated from MRE (red).

The temporal phase delay between resin skull and Sylgard® 527 brain motion ($\phi_{Sk/Br}$) for the homogeneous, interfacial, and membranous cranial phantoms are listed in Table 5.3. The calculated temporal phase delay was close to 0 or 2π for all three phantoms. Note that the relative phase in these phantoms is difficult to determine with the current level of precision.

	$Hom.Cran.$ $\phi_{Sk/Br}$ (rad)	$Int.Cran.$ $\phi_{Sk/Br}$ (rad)	$Mem.Cran.$ $\phi_{Sk/Br}$ (rad)
Ant.	**0.12**	**6.16**	**0.08**
Right	**0.16**	**6.17**	**0.06**
Left	**0.07**	**6.13**	**0.01**
Post.	**0.12**	**6.15**	**0.02**

Table 5.3: Temporal phase shift, $\phi_{Sk/Br}$, between harmonic motion of the skull (estimated by accelerometers and Sylgard® 527 brain (estimated by MRE) for the homogeneous cranial phantom, interfacial cranial phantom, and membranous cranial phantom. Results are shown for each of the four quadrants.

As with the cylindrical phantoms, wave displacement in the Sylgard® 527 brain in the three cranial phantoms is shown in Figure 5.21. In the homogeneous cranial phantom, higher amplitude wave displacement was seen than in the interfacial cranial phantom. Wave displacement of comparable amplitude was estimated in the membranous cranial phantom, with even higher diplacement values seen closer to the PVA falx and tentorium. In contrast, low wave displacement amplitudes were seen in the interfacial cranial phantom. Interestingly, larger amplitude SI shear wave displacement can be seen at the interface phantom posterior, near the source of actuation. As with the cylindrical phantoms, rigid-body displacement was larger in amplitude than wave displacement. Figure 5.22 provides comparison of wave displacement for each phantom scaled by skull rigid-body displacements estimated by accelerometers.

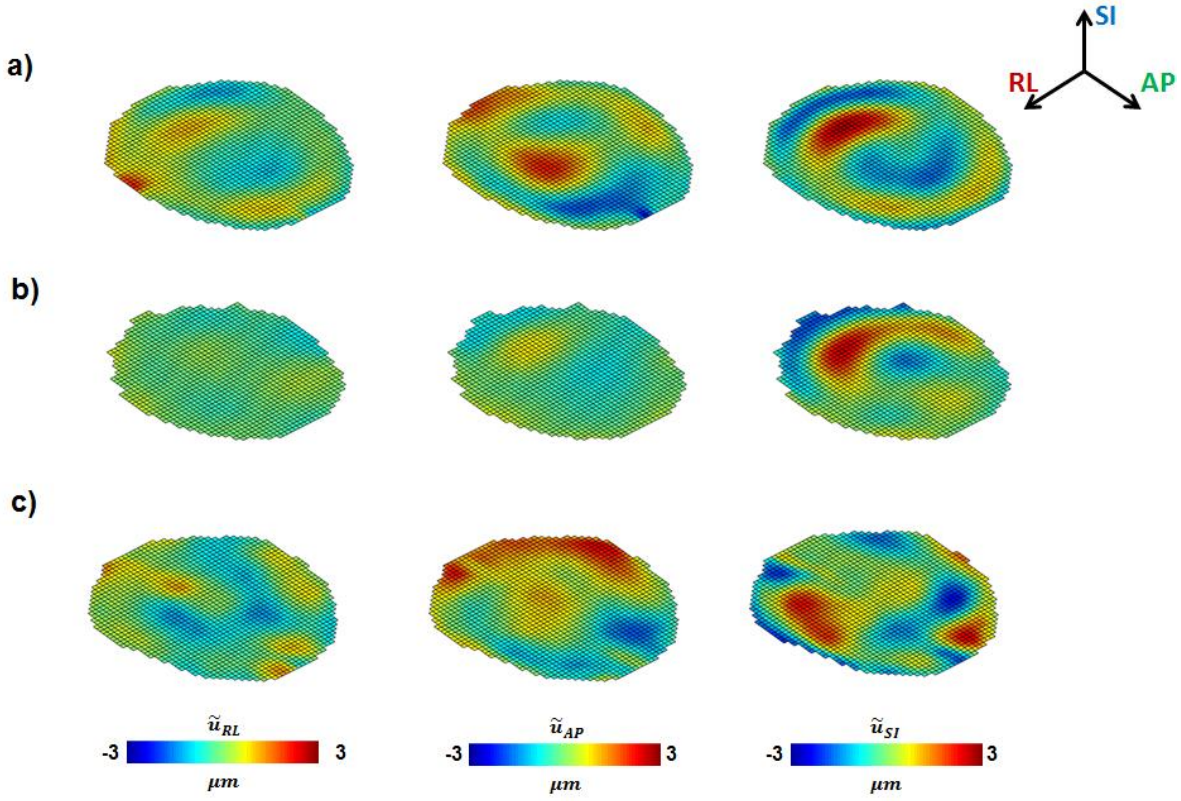

Figure 5.21: **RL, AP, and SI components of harmonic wave displacement (real part) in the a) homogeneous cranial phantom, b) interfacial cranial phantom, and c) membranous cranial phantom**

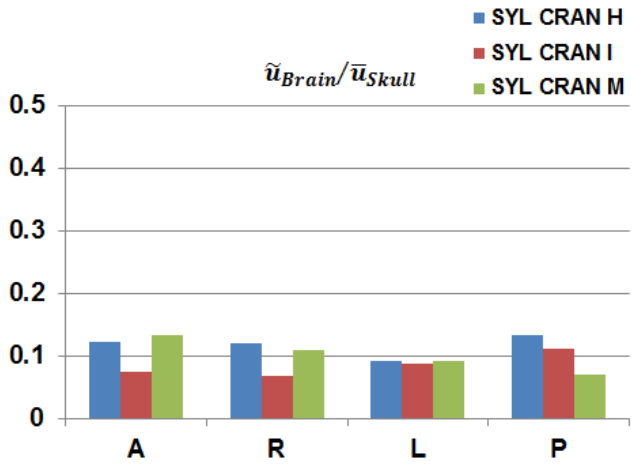

Figure 5.22: **Wave displacement ($\tilde{u}$), estimated by MRE, scaled by skull rigid-body displacement ($\bar{u}$) estimated from accelerometers. Mean values are shown in the anterior (A), right (R), left (L), and posterior (P) quadrants of the homogeneous cranial phantom, interfacial cranial phantom, and membranous cranial phantom.**

Octahedral shear strain estimates for the cranial phantoms are shown in Figure 5.23. Strain amplitudes were higher in the homogeneous cranial phantom than in the interface cranial phantom. In the membranous cranial phantom, larger strain patterns emerge close to the embedded falx and tentorium membrane. This contributions are most visible in higher slices where more of the hemispheres are divided by the falx.

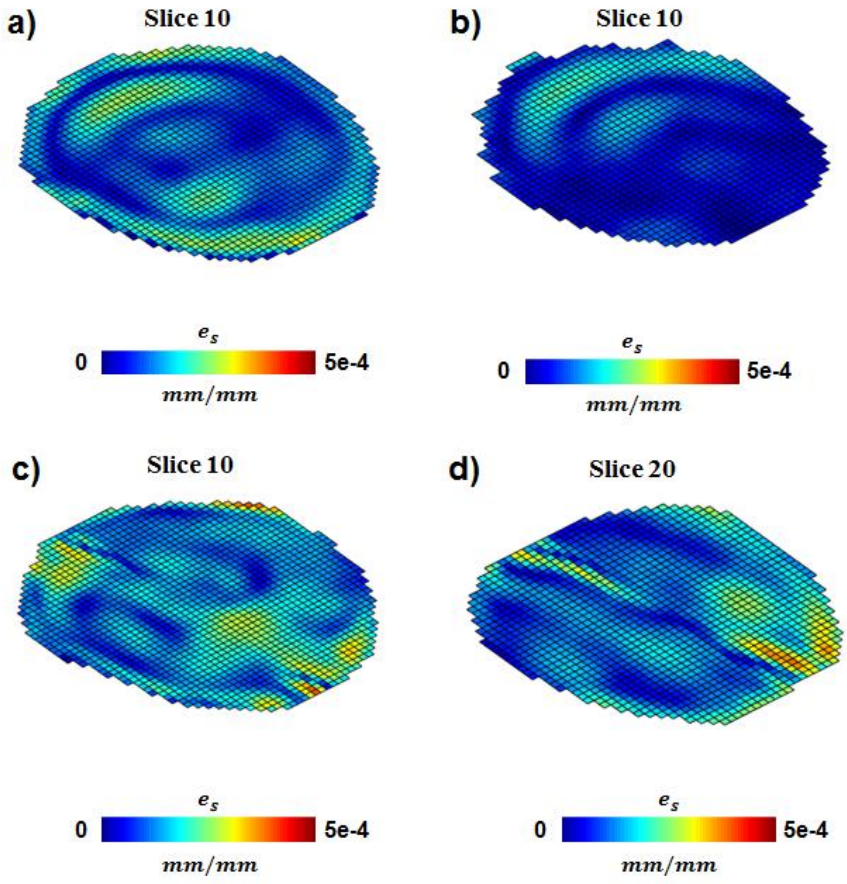

Figure 5.23: Octahedral shear strain estimates for axial slice 10 of the a) homogeneous cranial phantom, b) interfacial cranial phantom, and c) membranous cranial phantom and d) axial slice 20 of the membranous cranial phantom

5.3.4 Comparison of shear wave energy transport in cylindrical and cranial phantoms

Curl (**Γ**) at each MRE voxel was estimated for the cylindrical and cranial phantoms along with the 3D Poynting vector ($\boldsymbol{P_i}$) (Figure 5.24). In both the cylindrical and cranial phantom series, the homogeneous and membranous phantoms have larger curl amplitude estimates than the interfacial phantoms. The Poynting vectors for both the homogeneous and interfacial phantoms are mostly oriented radially from outside to inside, indicating propagation from the phantom exterior. In the membranous cylindrical and cranial phantoms, however, the Poynting vectors also originate from the embedded membranes, reflecting the important role of these membranes in inducing distortion in those areas. Energy contributions from the embedded membranes appear more obvious in higher slices in the membranous phantoms (Figure 5.25).

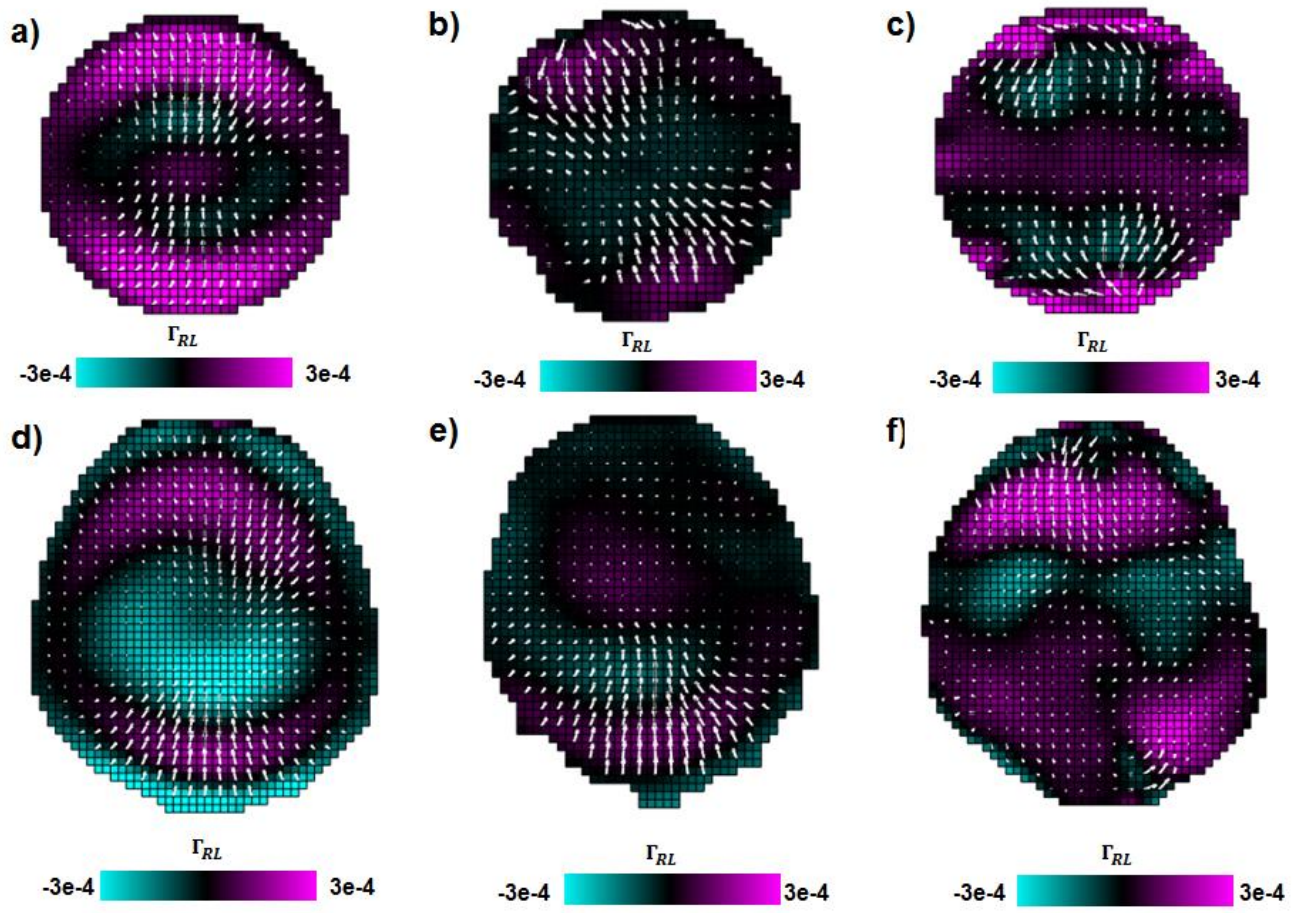

Figure 5.24: Poynting vectors (P_i) superimposed on the right-left component of curl (Γ_{RL}) at axial slice 10 for the a) homogeneous, b) interfacial, and c) membranous cylindrical phantoms and d) homogeneous, e) interfacial, f) membranous cranial phantoms.

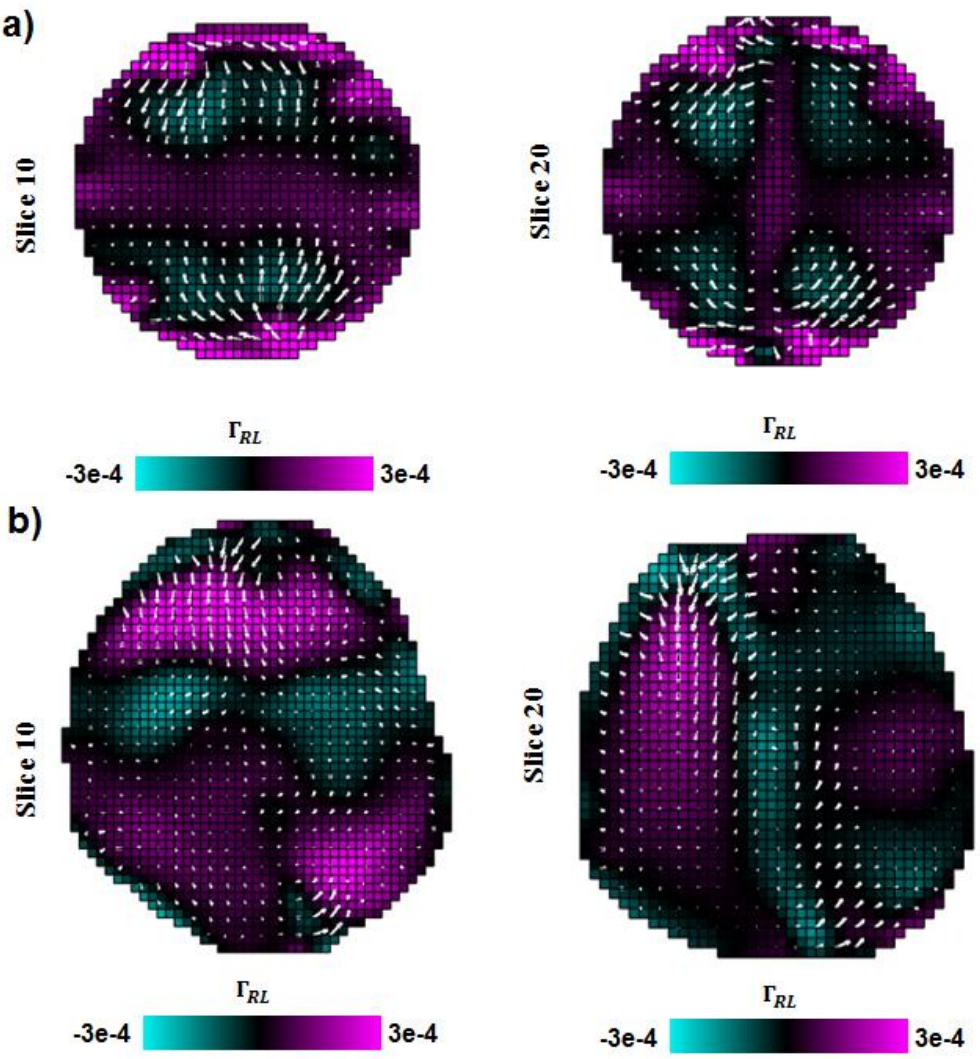

Figure 5.25: Poynting vectors (P_i) superimposed on the right-left component of curl (Γ_{RL}) for the a) membranous cylindrical phantom at axial slices 10 and 20 and b) membranous cranial phantom at axial slices 10 and 20.

Similar to the Poynting vectors, the estimated propagation direction vectors ($\vec{n}$) for both the homogeneous and interfacial phantoms are mostly oriented radially from outside to inside, indicating propagation from the phantom exterior (Figure 5.26). In the membranous cylindrical and cranial phantoms, the propagation direction vectors show distortion patterns emanating from the embedded membranes. Propagation from the embedded membranes appears more obvious in higher slices in the membranous phantoms (Figure 5.27).

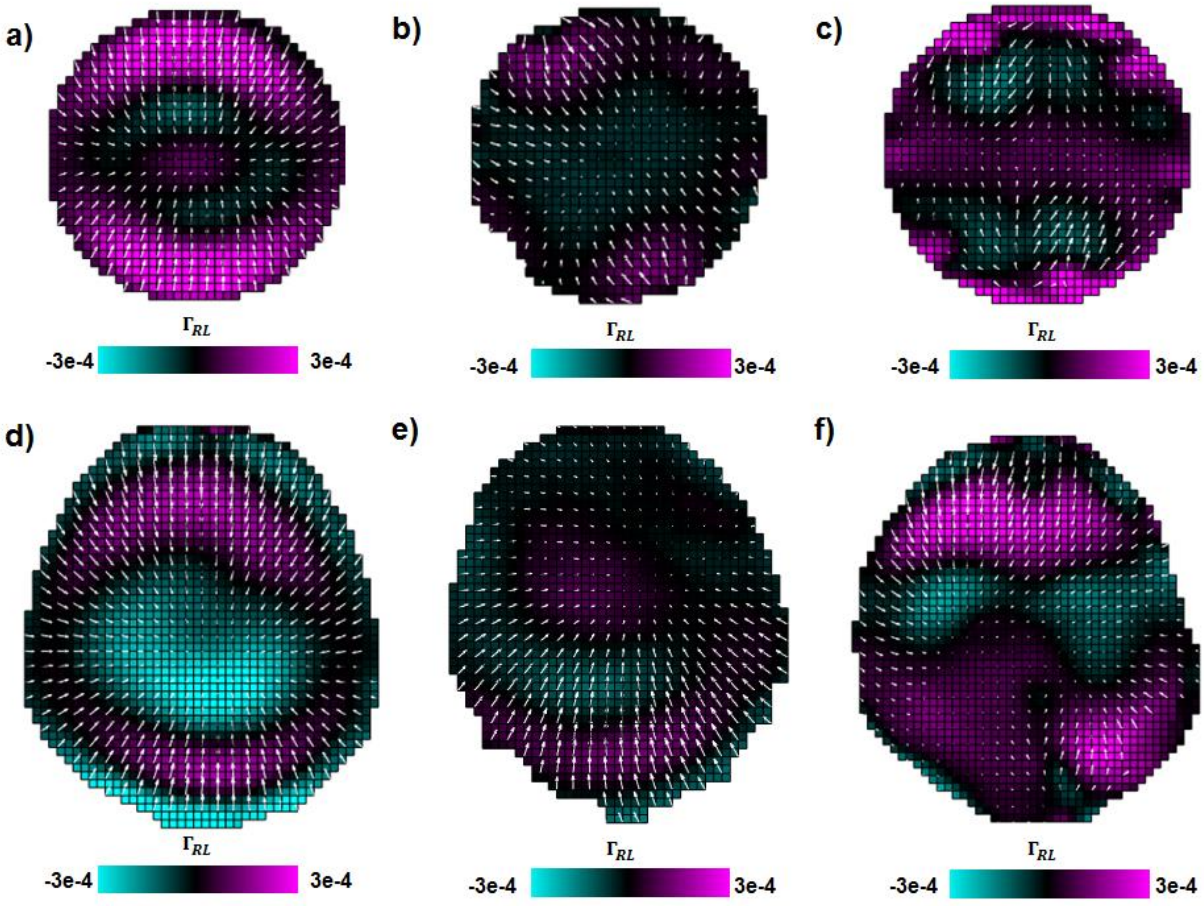

Figure 5.26: Propagation direction vectors ($\vec{n}$) superimposed on the right-left component of curl (Γ_{RL}) at axial slice 10 for the a) homogeneous, b) interfacial, and c) membranous cylindrical phantoms and d) homogeneous, e) interfacial, f) membranous cranial phantoms.

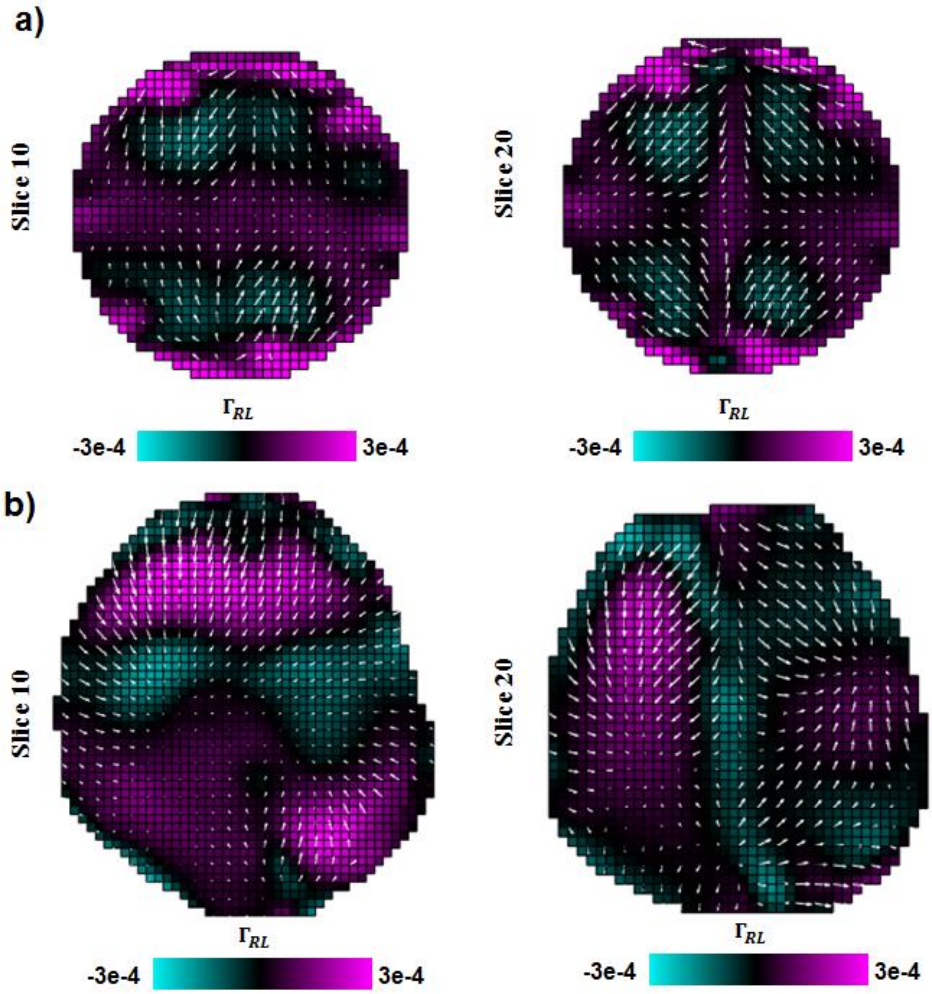

Figure 5.27: Propagation direction vectors ($\vec{n}$) superimposed on the right-left component of curl (Γ_{RL}) for the a) membranous cylindrical phantom at axial slices 10 and 20 and b) membranous cranial phantom at axial slices 10 and 20.

5.4 Discussion and Conclusions

Experimental data indicate that the presence of a soft interface alters wave motion in the Sylgard® 527 cylindrical phantoms. Additionally, the presence of flexible PVA membranes appears to increase regional shear wave displacement amplitude and affects propagation direction. For instance, in the cylindrical phantoms, waves in the homogeneous and interfacial phantoms propagate inward from the acrylic case exterior. In contrast, the membranous cylindrical phantom appears to have shear waves propagating from the PVA falx. As a result, though the membranous phantom contains a liquid interface, the presence of the falx increases shear wave motion amplitude throughout the MRE slice volume.

In the cranial phantoms, analogous differences are seen between the homogeneous, interfacial, and membranous phantoms, though the details of shear wave propagation are different from those in the cylindrical phantoms. Though shear waves propagate toward the midbrain from the skull exterior in the homogeneous and interfacial cranial phantoms, the wave motion components have markedly different propagation patterns. Differences such as the skull geometry and material likely affect how motion is transmitted from the actuator to the Sylgard® 527 brain. Additionally, a resin skull is used in the cranial phantom whereas the three cylindrical phantoms use acrylic cases. This difference of material could modify the transmission of motion to the Sylgard® 527.

Key conclusions that can be made from comparing these phantoms include 1) a liquid interface between the cranial phantom brain and skull dampens and alters the pattern of dynamic

deformation of the brain and 2) membranes and attachment points between the skull and brain increase the magnitude of wave motion and associated deformation in the brain.

Some limitations of this study are acknowledged: 1) Though degassing is performed in the cylindrical phantoms, the mode of cranial phantom fabrication made it challenging to remove air bubbles in the Sylgard® 527 brain. 2) The homogenous cylindrical phantom has a free surface at the top of the cylinder, which increases the magnitude of wave motion estimated during MRE as shown by comparison with a second version with no free surface. 3) Sylgard® 527 samples are slightly stiffer than brain tissue. 4) Only one mode of actuation (the pillow actuator) was used to excite these phantoms. Despite these limitations, it is clear that a soft interface and dural membranes play an important role in transmitting motion and imparting deformation to surrounding tissue.

5.5 Summary

By increasing anatomical complexity in three cylindrical and three cranial phantoms, this study provides insight into the mechanical contributions of the skull-brain interface. These experimental results strongly suggest that the falx cerebri and tentorium cerebelli play prominent roles in the transmission and reflection of shear waves within the brain. By testing these different cases, we are better able to decouple and quantify how these anatomical features affect motion transmitted from the skull to the brain.

Chapter 6: Conclusions and Future Directions

6.1 Summary of Work

This thesis has focused on assessing the role of the skull-brain interface in transmitting motion of the skull to the brain, particularly the dynamic deformations of the brain that are thought to cause TBI. The specific aims were:

Aim 1: *Relate 3D skull kinematics to brain tissue deformation by comparing (i) direct mechanical characterization of skull motion by an array of tri-axial accelerometers with (ii) brain displacement estimates from MRE.*

Using a mouth guard array that held three tri-axial accelerometers, I reconstructed skull motion during MRE and compared it with brain tissue displacements estimated from MRE measurements. By contrasting the transmission of motion from skull to brain in human subjects with the analogous motion transmission from case to gel in a homogenous gelatin phantom, I quantified the attenuation of motion imparted to the brain (Chapter 3).

Aim 2: *Design an acquisition and analysis protocol capable of estimating simultaneous scalp and brain displacements using MRE.*

By using lower motion-encoding gradient (MEG) strength MRE, I measured displacement fields simultaneously in both the scalp and brain of human subjects. Rigid-body displacements of the brain and scalp estimated from MRE were then compared with skull displacements estimated from an instrumented mouth guard containing three tri-axial accelerometers. These findings indicate that the scalp can serve as an adequate anatomical reference body for estimating head dynamics during MRE (Chapter 4).

Aim 3: *Model the mechanical and material properties of the skull-brain interface using simplified (cylindrical) and anatomically-accurate cranial phantoms*

I fabricated and imaged three cylindrical and three cranial Sylgard® 527 phantoms with progressively more complete representations of the skull-brain interface. Cranial phantoms were created using anatomical data of a cadaveric specimen with realistic representations of the falx cerebri and tentorium cerebelli dural membranes. Chapter 5 describes how the presence of a liquid interface alters wave motion amplitude and propagation while dural membranes facilitate shear wave propagation within brain tissue.

6.2 Limitations

6.2.1 Acceleration reconstruction from closely spaced accelerometers

I performed multiple benchtop tests to assess the validity of motion reconstruction from accelerometers embedded in the MGA under near-ideal experimental conditions (Section 2.2.3), accuracy and precision are likely not as high in human subjects. For instance, cylindrical phantoms used in Chapters 3 and 5 often have the accelerometers mounted close to the system origin while human subjects are biting down on the accelerometers at a location that is more inferior and anterior (Figure 3.2b). As a result, any artefactual differences between recorded accelerometer signals will lead to larger artifacts in rotations predicted by rigid-body motion fitting of the accelerometer data.

6.2.2 MRE signal resolution and fidelity

There is a tradeoff in signal amplitude and resolution in MR techniques such as MRE that limits the scale of observable displacement wavelength [34]. Additionally, when considering head soft tissue such as the scalp region in Chapter 4, the EPI sequence has a resolution of 3mm per voxel, thus increasing the likelihood of partial volume artifacts. This tradeoff is hard to accommodate, however, given the variability in signal in scalp voxels.

6.3 Future Directions

Though MRE has been used to provide *in vivo* estimates of brain tissue material properties, few researchers have attempted to use bulk motion recordings to characterize motion transmission from the skull to the brain. The work presented in this study can be expanded upon to provide better tools for motion correction in MR imaging, improvements in MRE data interpretation, and more comprehensive phantoms for simulating skull-brain interactions.

While the MRI-safe accelerometers used in this study have provided valuable information about head dynamics and even MRE sequence timing, further bench trials of different actuation modes and frequencies are integral for understanding the types of motion imparted to tissue during scanning. Further testing with additional accelerometers or different accelerometer positions may enable more accurate estimates of skull motion.

While multiple phantoms were created and tested in these studies, only results for an actuation frequency of 50 Hz are shown. Testing these phantoms at different frequencies may enable greater insight into the frequency-dependent properties of the skull-brain interface. Additionally, all phantoms constructed in this study are isotropic even though there is strong evidence that brain white matter has anisotropic properties [9], [11], [53].

6.4 Conclusion

Traumatic brain injury (TBI) is a pervasive neurological injury that appears with a wide spectrum of associated symptoms and pathology. Though the effects of TBI are widely documented, there remains a lack of knowledge about injury mechanisms, specifically the mechanical coupling of the brain and skull. Knowledge of relative skull and brain motion is essential for creating accurate computational models to characterize modes of TBI.

The data and methods described in this dissertation provide characterization of the mechanical contributions of the skull-brain interface in human subjects *in vivo*. Further, the effects of this interface are simulated in physical models, enabling insight into the attenuation and transmission of shear wave motion. These results confirm that the skull-brain interface plays a crucial role in brain tissue deformation during skull loading. The properties of this interface are measurable and the quantitative data presented in this work will be useful in the parameterization and validation of future computational models of TBI.

Appendix A: MRI-Safe, Tri-axial Accelerometer Setup and Data Collection

This section describes the components and set up of the accelerometer data acquisition system used for MRE experiments throughout this work. Signals from three tri-axial, MRI-safe accelerometers (TSD109C2-MRI, BIOPAC©, Goleta, CA) were recorded using a pipeline detailed in the flowchart in Figure A.1.

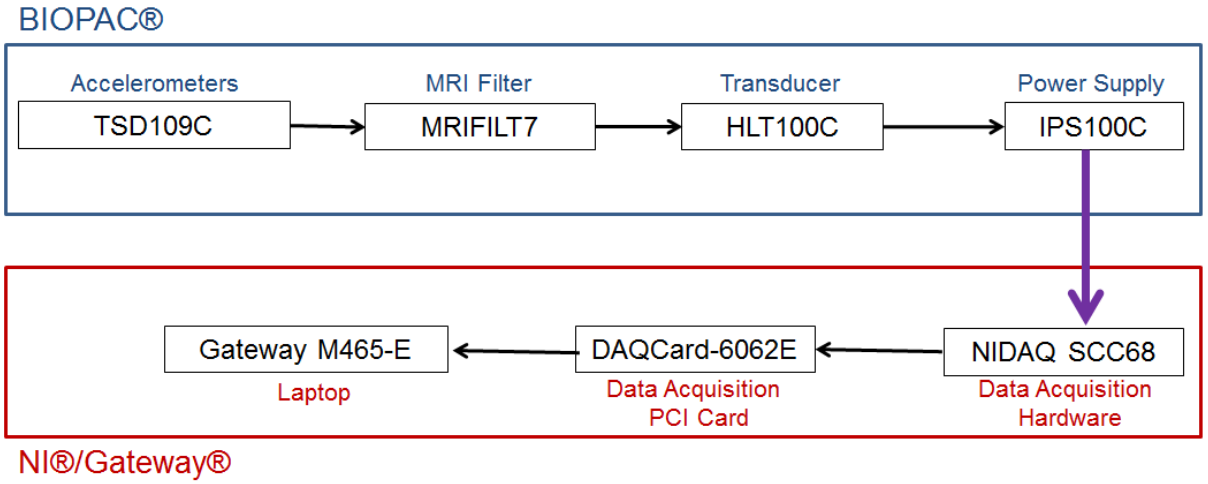

Figure A.1: Flowchart demonstrating the accelerometer data collection pipeline. BIOPAC© components are involved in data collection, filtering, and conversion while the NI® products translate analog signals into digital data for processing on a Gateway laptop.

Figure A.2. documents the hardware used for accelerometer data collection. During an MRE scan, the signals recorded by the TSD109C accelerometers is filtered by a BIOPAC© MRI filter (MRIFILT7) and then passed to an integrated transducer/power supply (HLT100C and IPS100C) hub via serial connectors. Since three tri-axial accelerometers are used, a total of 9 input serial connectors are used. The IPS100C passes 9 BNC outputs which are plugged into a NI® data

acquisition board (NIDAQ© SCC68) that has 9 female BNCs attached to the front of the board case. These nine female BNCs terminate into a protoboard within the data acquisition board sharing a common ground (Figure A3). An additional BNC input captures the MRE sequence trigger output from the 3T Trio® MRI scanner. The output from the data acquisition board is a I/O connector block which can interface with a PCI card (DAQCard-6062E) that interfaces with a Gateway Laptop (M465-E).

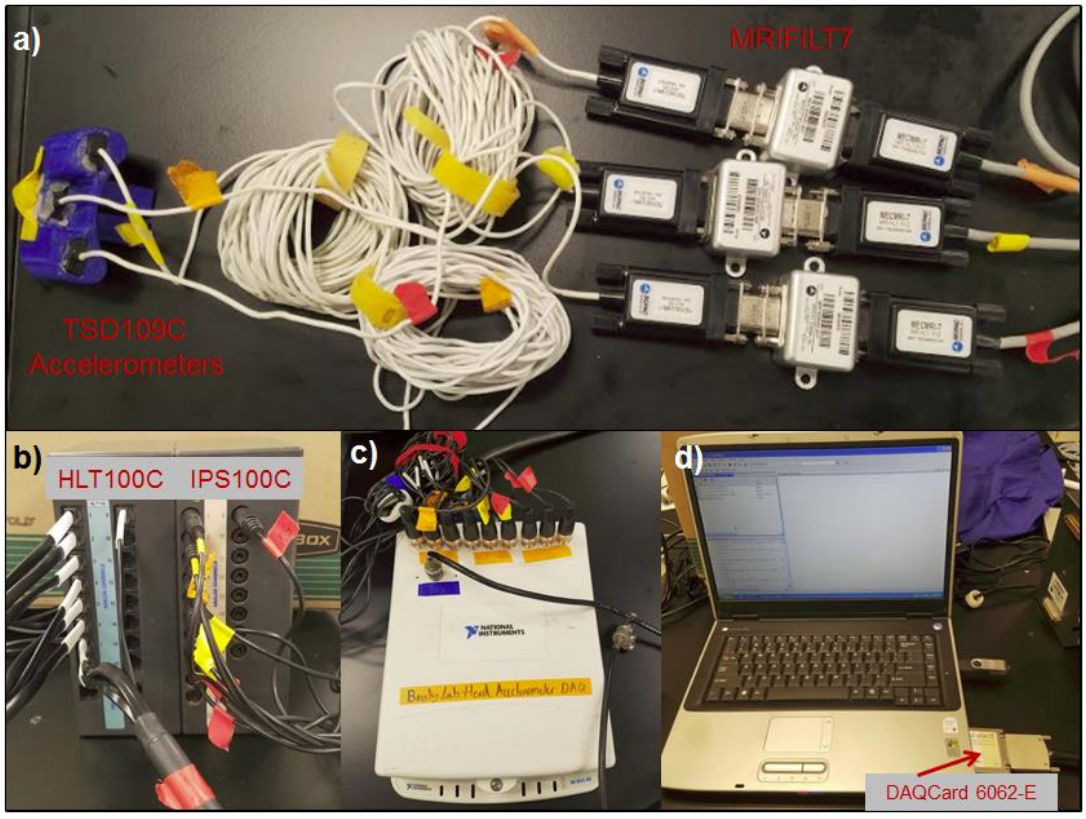

Figure A.2: Accelerometer data collection system. A) Three TSD109C tri-axial, MRI-safe accelerometers each have 30 feet of cabling that terminate into an MRIFILT7. B) MRIFILT7 cables have 3 serial outputs for each component of acceleration (9 total outputs for this system). The serial outputs are plugged into the HLT100C while the IPS100C provides output in the form of BNC cables. C) BNC cables output from the IPS100C plug into 9 female BNCs attached to the front of the SCC-68 NI® DAQ board. D) The I/O cable from the SCC-68 attaches to the DAQCard 6062-E that is placed into a slot on the side of a Gateway Laptop (M465-E).

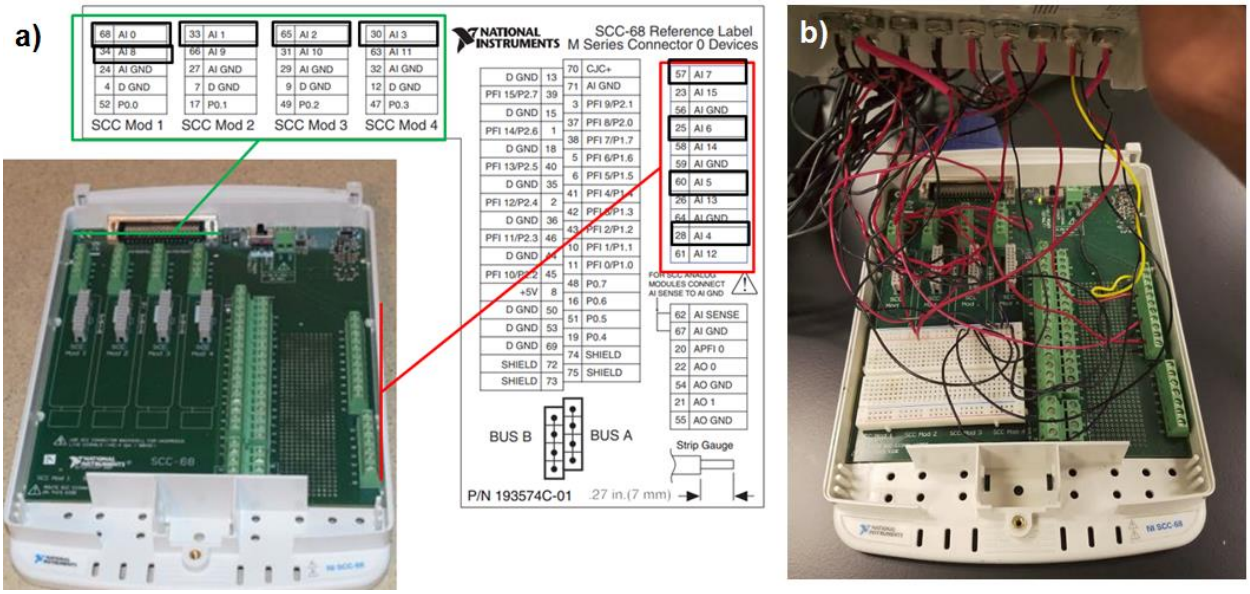

Figure A.3: NI-DAQ SCC-68 board layout. a) Picture of SCC-68 inner housing. Analog inputs 0-8 are used for the nine analog inputs from the three tri-axial accelerometers. b) Inside of current NI-DAQ SCC-68 with all cables attached. A protoboard is placed inside the housing to serve as a common ground for all inputs.

During data collection, the Gateway Laptop runs MATLAB© and uses the Analog Data Acquisition toolkit, specifically the "analoginput" function. During accelerometer data collection, the sampling rate was set to 10,000 samples/sec and acquisition windows were typically 30-45 s in duration. A schematic of the Resoundant™ MRE actuation system set up for the Siemens 3T Trio® in the Center for Clinical Imaging Research at Washington University in St. Louis can be found in Figure A.4.

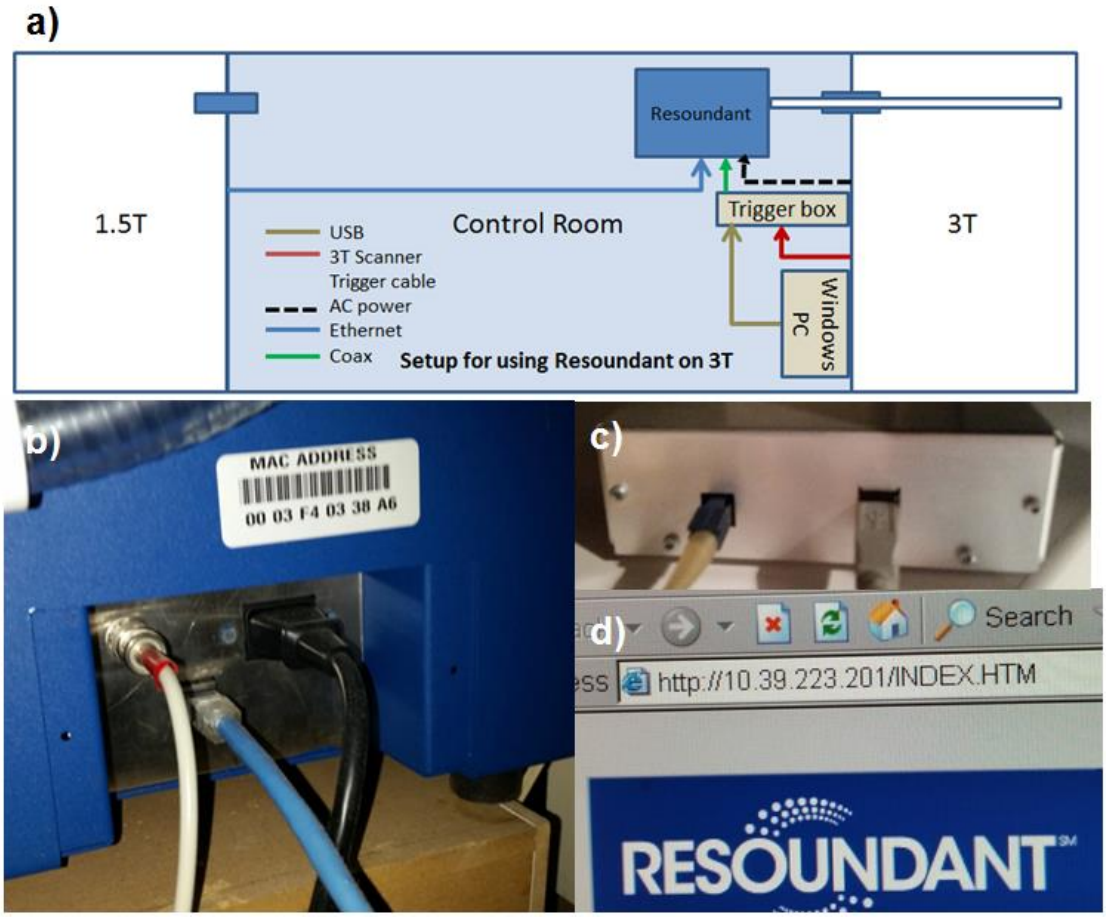

Figure A.4: **Resoundant™ setup in the Washington University Center for Clinical Imaging Research. A) Schematic of the positioning for the Resoundant™ hardware and cabling. B) Rear of the Resoundant™ has ports for a coaxial cable that plugs into the trigger box, AC power, and an Ethernet cable that provides network connection for the Resoundant™. C) Trigger box takes in the optical trigger cable from the 3T scanner and a coaxial cable from the back of the Resoundant™. D) Resoundant™ IP address entered into the Windows PC.**

References

[1] M. Faul and V. Coronado, "Epidemiology of traumatic brain injury," *Handb. Clin. Neurol.*, vol. 127, pp. 3–13, 2015.

[2] V. G. Coronado *et al.*, "Trends in Sports- and Recreation-Related Traumatic Brain Injuries Treated in US Emergency Departments: The National Electronic Injury Surveillance System-All Injury Program (NEISS-AIP) 2001-2012.," *J. Head Trauma Rehabil.*, vol. 30, no. 3, pp. 185–197, 2015.

[3] E. J. Pellman *et al.*, "Concussion in professional football: Reconstruction of game impacts and injuries," *Neurosurgery*, vol. 53, no. 4, pp. 799–814, 2003.

[4] D. A. Hovda, "The neurophysiology of concussion," in *Concussion*, 2012, pp. 28–37.

[5] S. J. Tepper, "Mild traumatic brain injury in U.S. soldiers returning from Iraq: Commentary," *Headache*, vol. 48, no. 6. pp. 985–986, 2008.

[6] V. E. Johnson, W. Stewart, and D. H. Smith, "Axonal pathology in traumatic brain injury," *Experimental Neurology*, vol. 246. pp. 35–43, 2013.

[7] F. Crawford *et al.*, "Identification of plasma biomarkers of TBI outcome using proteomic approaches in an APOE mouse model.," *J. Neurotrauma*, vol. 29, no. 2, pp. 246–260, 2012.

[8] B. A. Plog *et al.*, "Biomarkers of traumatic injury are transported from brain to blood via the glymphatic system," *J Neurosci*, vol. 35, no. 2, pp. 518–526, 2015.

[9] C. Giordano and S. Kleiven, "Connecting fractional anisotropy from medical images with mechanical anisotropy of a hyperviscoelastic fibre-reinforced constitutive model for brain tissue," *J. R. Soc. Interface*, vol. 11, no. 91, pp. 20130914–20130914, 2013.

[10] S. Kleiven and W. N. Hardy, "Correlation of an FE Model of the Human Head with Local Brain Motion – Consequences for Injury Prediction," *Stapp Car Crash J.*, vol. 46, no. November 2202, pp. 123–144, 2002.

[11] C. Giordano, R. J. H. Cloots, J. A. W. van Dommelen, and S. Kleiven, "The influence of anisotropy on brain injury prediction," *J. Biomech.*, vol. 47, no. 5, pp. 1052–1059, 2014.

[12] H. Mao *et al.*, "Development of a finite element human head model partially validated with thirty five experimental cases," *J. Biomech. Eng.*, vol. 135, no. 11, p. 111002, 2013.

[13] S. S. Margulies, L. E. Thibault, and T. A. Gennarelli, "Physical model simulations of brain injury in the primate.," *J. Biomech.*, vol. 23, no. 8, pp. 823–36, 1990.

[14] V. R. Hodgson, E. S. Gurdjian, and L. M. Thomas, "Experimental skull deformation and brain displacement demonstrated by flash x-ray technique.," *J. Neurosurg.*, vol. 25, no. 5, pp. 549–52, 1966.

[15] D. E. Raymond and C. A. Bir, "A Biomechanical Evaluation of Skull-Brain Surrogates to Blunt High-Rate Impacts to Postmortem Human Subjects," *J. Forensic Sci.*, vol. 60, no. 2, pp. 370–373, 2015.

[16] R. L. Stalnaker, J. W. Melvin, G. S. Nusholtz, N. M. Alem, and J. B. Benson, "Head Impact Response," *Brain Inj.*, pp. 3156–3170, 1977.

[17] A. A. Sabet, E. Christoforou, B. Zatlin, G. M. Genin, and P. V. Bayly, "Deformation of the human brain induced by mild angular head acceleration," *J. Biomech.*, vol. 41, no. 2,

pp. 307–315, 2008.
[18] Y. Feng, T. M. Abney, R. J. Okamoto, R. B. Pless, G. M. Genin, and P. V Bayly, "Relative brain displacement and deformation during constrained mild frontal head impact.," *J. R. Soc. Interface*, vol. 7, no. 53, pp. 1677–88, 2010.
[19] A. K. Knutsen *et al.*, "Improved measurement of brain deformation during mild head acceleration using a novel tagged MRI sequence," *J. Biomech.*, vol. 47, no. 14, pp. 3475–3481, 2014.
[20] A. G. Monea, I. Verpoest, J. Vander Sloten, G. Van der Perre, J. Goffin, and B. Depreitere, "Assessment of Relative Brain-Skull Motion in Quasistatic Circumstances by Magnetic Resonance Imaging," *J. Neurotrauma*, vol. 29, no. 13, pp. 2305–2317, 2012.
[21] S. Ji, F. Liu, D. Roberts, A. Hartov, and K. Paulsen, "Brain-skull boundary conditions in a computational deformation model," in *Medical Imaging 2007 Visualization and Image Guided Procedures*, 2007, vol. 6509, p. 65092J–65092J–11.
[22] S. Ji, D. W. Roberts, A. Hartov, and K. D. Paulsen, "Brain-skull contact boundary conditions in an inverse computational deformation model," *Med. Image Anal.*, vol. 13, no. 4, pp. 659–672, 2009.
[23] C. Ljung, "A model for brain deformation due to rotation of the skull," *J. Biomech.*, vol. 8, no. 5, pp. 263–274, 1975.
[24] R. H. Daffner, A. R. Lupetin, N. Dash, Z. L. Deeb, R. J. Sefczek, and R. L. Schapiro, "MRI in the detection of malignant infiltration of bone marrow," *Am. J. Roentgenol.*, vol. 146, no. 2, pp. 353–358, 1986.
[25] X.X. Jiang, Z.X. Yan, Y.Y. Song, and W.L. Zhao, "A pooled analysis of MRI in the detection of bone marrow infiltration in patients with malignant lymphoma.," *Clin. Radiol.*, vol. 68, no. 3, pp. e143-53, 2013.
[26] T. Woolsey, J. Hanaway, and M. Gado, *The Brain Atlas: A Visual Guide to the Human Central Nervous System*, 3rd ed. Hoboken, NJ: John Wiley and Sons, 2013.
[27] E. H. Clayton, G. M. Genin, and P. V. Bayly, "Transmission, attenuation and reflection of shear waves in the human brain," *J. R. Soc. Interface*, vol. 9, no. 76, pp. 2899–2910, 2012.
[28] H. Zou, S. Kleiven, and J. P. Schmiedeler, "The effect of brain mass and moment of inertia on relative brain-skull displacement during low-severity," *Int. J. Crashworthiness*, vol. 12, no. 4, pp. 341–353, 2007.
[29] S. A. Shatsky, W. A. Alter, D. E. Evans, V. W. Armbrustmacher, G. Clark, and K. M. Earle, "Traumatic distortions of the primate head and chest: correlation of biomechanical, radiological and pathological data," *Proc. Stapp Car Crash Conf.*, vol. 18, p. , 1974.
[30] S. Kleiven and H. Von Holst, "Consequences of head size following trauma to the human head," *J. Biomech.*, vol. 35, no. 2, pp. 153–160, 2002.
[31] X. Trosseille, C. Tarriere, F. Lavaste, F. Guillon, and A. Domont, "Development of a FEM of the human head according to a specific test protocol," *Proc. 46th Stapp Car Conf.*, pp. 235–253, 1992.
[32] W. N. Hardy, C. D. Foster, M. J. Mason, K. H. Yang, A. I. King, and S. Tashman, "Investigation of Head Injury Mechanisms Using Neutral Density Technology and High-Speed Biplanar X-ray," *Stapp Car Crash J.*, vol. 45, pp. 337–368, 2001.
[33] C. Giordano, S. Zappalà, and S. Kleiven, "Anisotropic finite element models for brain injury prediction: the sensitivity of axonal strain to white matter tract inter-subject

variability," *Biomech. Model. Mechanobiol.*, vol. 16, no. 4, pp. 1269–1293, 2017.
[34] R. Muthupillai, D. Lomas, P. Rossman, J. Greenleaf, A. Manduca, and R. Ehman, "Magnetic resonance elastography by direct visualization of propagating acoustic strain waves," *Science (80-.).*, vol. 269, no. 5232, pp. 1854–1857, 1995.
[35] S. A. Kruse *et al.*, "Magnetic resonance elastography of the brain," *Neuroimage*, vol. 39, no. 1, pp. 231–237, Jan. 2008.
[36] M. J. Sands and A. Levitin, "Basics of magnetic resonance imaging," *Semin. Vasc. Surg.*, vol. 17, no. 2, pp. 66–82, 2004.
[37] T. Geva, "Magnetic resonance imaging: historical perspective.," *J. Cardiovasc. Magn. Reson.*, vol. 8, no. 4, pp. 573–580, 2006.
[38] Z.P. Liang and P. C. Lauterbur, *Principles of Magnetic Resonance Imaging*, vol. 177, no. 4. 2000.
[39] M. J. Graves, "Magnetic resonance angiography.," *Br. J. Radiol.*, vol. 70, no. April 1996, pp. 6–28, 1997.
[40] W. M. Lai, D. Rubin, and E. Krempl, "Kinematics of a Continuum," in *Introduction to Continuum Mechanics*, 2010, pp. 69–153.
[41] M. C. Murphy *et al.*, "Magnetic resonance elastography of the brain in a mouse model of Alzheimer's disease: Initial results," *Magn. Reson. Imaging*, vol. 30, no. 4, pp. 535–539, 2012.
[42] R. Sinkus, M. Tanter, T. Xydeas, S. Catheline, J. Bercoff, and M. Fink, "Viscoelastic shear properties of in vivo breast lesions measured by MR elastography," in *Magnetic Resonance Imaging*, 2005, vol. 23, no. 2 SPEC. ISS., pp. 159–165.
[43] Y. K. Mariappan, K. J. Glaser, and Richard L Ehman, "Magnetic Resonance Elastography: a Review," *Clin. Anat.*, vol. 23, no. 5, pp. 497–511, 2010.
[44] S. A. Kruse *et al.*, "Magnetic resonance elastography of the brain," *Neuroimage*, vol. 39, no. 1, pp. 231–237, 2008.
[45] E. H. Clayton, G. M. Genin, and P. V Bayly, "Transmission, attenuation and reflection of shear waves in the human brain," *J. R. Soc. Interface*, vol. 9, no. 76, pp. 2899–2910, 2012.
[46] M. C. Murphy *et al.*, "Measuring the characteristic topography of brain stiffness with magnetic resonance elastography," *PLoS One*, vol. 8, no. 12, pp. 1–14, 2013.
[47] J. Guo *et al.*, "Towards an Elastographic Atlas of Brain Anatomy," *PLoS One*, vol. 8, no. 8, 2013.
[48] C. L. Johnson *et al.*, "Local mechanical properties of white matter structures in the human brain," *Neuroimage*, vol. 79, pp. 145–152, 2013.
[49] M. C. Murphy *et al.*, "Decreased brain stiffness in Alzheimer's disease determined by magnetic resonance elastography," *J. Magn. Reson. Imaging*, vol. 34, no. 3, pp. 494–498, 2011.
[50] A. Arani *et al.*, "Measuring the effects of aging and sex on regional brain stiffness with MR elastography in healthy older adults," *Neuroimage*, vol. 111, pp. 59–64, 2015.
[51] K.J. Streitberger *et al.*, "In vivo viscoelastic properties of the brain in normal pressure hydrocephalus.," *NMR Biomed.*, vol. 24, no. 4, pp. 385–92, 2011.
[52] A. Romano *et al.*, "In vivo Waveguide elastography: Effects of neurodegeneration in patients with amyotrophic lateral sclerosis," *Magn. Reson. Med.*, vol. 72, no. 6, pp. 1755–1761, 2014.

[53] R. J. H. Cloots, J. A. W. Van Dommelen, T. Nyberg, S. Kleiven, and M. G. D. Geers, "Micromechanics of diffuse axonal injury: Influence of axonal orientation and anisotropy," *Biomech. Model. Mechanobiol.*, vol. 10, no. 3, pp. 413–422, 2011.
[54] T. E. Oliphant, A. Manduca, R. L. Ehman, and J. F. Greenleaf, "Complex-valued stiffness reconstruction for magnetic resonance elastography by algebraic inversion of the differential equation," *Magn. Reson. Med.*, vol. 45, no. 2, pp. 299–310, 2001.
[55] M. D. J. McGarry *et al.*, "Multiresolution MR elastography using nonlinear inversion," *Med. Phys.*, vol. 39, no. 10, p. 6388, 2012.
[56] C. L. Johnson *et al.*, "Magnetic resonance elastography of the brain using multishot spiral readouts with self-navigated motion correction," *Magn. Reson. Med.*, vol. 70, no. 2, pp. 404–412, 2013.
[57] L. V Hiscox *et al.*, "Magnetic resonance elastography (MRE) of the human brain: technique, findings and clinical applications," *Phys. Med. Biol.*, vol. 61, no. 24, pp. R401–R437, 2016.
[58] D. Klatt, C. Friedrich, Y. Korth, R. Vogt, J. Braun, and I. Sack, "Viscoelastic properties of liver measured by oscillatory rheometry and multifrequency magnetic resonance elastography," *Biorheology*, vol. 47, no. 2, pp. 133–141, 2010.
[59] J. Vappou, E. Breton, P. Choquet, C. Goetz, R. Willinger, and A. Constantinesco, "Magnetic resonance elastography compared with rotational rheometry for in vitro brain tissue viscoelasticity measurement," *Magn. Reson. Mater. Physics, Biol. Med.*, vol. 20, no. 5–6, pp. 273–278, 2007.
[60] E. S. Gurdjian, V. R. Hodgson, and L. M. Thomas, "Studies on mechanical impedance of the human skull: Preliminary report," *J. Biomech.*, vol. 3, no. 3, 1970.
[61] J. Genin and J. H. Ginsberg, *Dynamics*. West New York, NJ: Wiley, 1995.
[62] I. Sack, B. Beierbach, U. Hamhaber, D. Klatt, and J. Braun, "Non-invasive measurement of brain viscoelasticity using magnetic resonance elastography," *NMR Biomed.*, vol. 21, no. 3, pp. 265–271, 2008.
[63] S. A. Kruse *et al.*, "Tissue characterization using magnetic resonance elastography: preliminary results.," *Phys. Med. Biol.*, vol. 45, no. 6, pp. 1579–90, 2000.
[64] A. A. Badachhape *et al.*, "The Relationship of 3D Human Skull Motion to Brain Tissue Deformation in Magnetic Resonance Elastography Studies," *J. Biomech. Eng.*, vol. 139, no. May, pp. 1–12, 2017.
[65] R. G. Steen, R. M. Hamer, and J. A. Lieberman, "Measuring brain volume by MR imaging: Impact of measurement precision and natural variation on sample size requirements," *Am. J. Neuroradiol.*, vol. 28, no. 6, pp. 1119–1125, 2007.
[66] R. J. Okamoto, E. H. Clayton, and P. V Bayly, "Viscoelastic properties of soft gels: comparison of magnetic resonance elastography and dynamic shear testing in the shear wave regime," *Phys. Med. Biol.*, vol. 56, no. 19, pp. 6379–6400, 2011.
[67] S. M. Smith *et al.*, "Advances in functional and structural MR image analysis and implementation as FSL," in *NeuroImage*, 2004, vol. 23, no. SUPPL. 1.
[68] M. D. J. McGarry, E. E. W. Van Houten, P. R. Perriñez, A. J. Pattison, J. B. Weaver, and K. D. Paulsen, "An octahedral shear strain-based measure of SNR for 3D MR elastography," *Phys. Med. Biol.*, vol. 56, no. 13, pp. N153–N164, 2011.
[69] K. Scharnhorst, "Angles in complex vector spaces," *Acta Appl. Math.*, vol. 69, no. 1, pp.

95–103, 2001.
[70] C. L. Johnson *et al.*, “3D multislab, multishot acquisition for fast, whole-brain MR elastography with high signal-to-noise efficiency,” *Magn. Reson. Med.*, vol. 71, no. 2, pp. 477–485, 2014.
[71] S. M. Atay, C. D. Kroenke, A. Sabet, and P. V. Bayly, “Measurement of the Dynamic Shear Modulus of Mouse Brain Tissue In Vivo By Magnetic Resonance Elastography,” *J Biomech Eng*, vol. 22, no. 5, p. 629, 2008.
[72] M. Jenkinson, “Fast, automated, N-dimensional phase-unwrapping algorithm,” *Magn. Reson. Med.*, vol. 49, no. 1, pp. 193–197, 2003.
[73] S. P. Broglio, J. T. Eckner, and J. S. Kutcher, “Field-based measures of head impacts in high school football athletes,” *Curr. Opin. Pediatr.*, vol. 24, no. 6, pp. 702–708, 2012.
[74] D. B. Camarillo, P. B. Shull, J. Mattson, R. Shultz, and D. Garza, “An instrumented mouthguard for measuring linear and angular head impact kinematics in american football,” *Ann. Biomed. Eng.*, vol. 41, no. 9, pp. 1939–1949, 2013.
[75] L. C. Wu *et al.*, “In Vivo Evaluation of Wearable Head Impact Sensors,” *Ann. Biomed. Eng.*, vol. 44, no. 4, pp. 1234–1245, 2016.
[76] L. C. Wu *et al.*, “Bandwidth and sample rate requirements for wearable head impact sensors,” *J. Biomech.*, vol. 49, no. 13, pp. 2918–2924, 2016.
[77] P. A. Yushkevich, Y. Gao, and G. Gerig, “ITK-SNAP: An interactive tool for semi-automatic segmentation of multi-modality biomedical images,” in *Proceedings of the Annual International Conference of the IEEE Engineering in Medicine and Biology Society, EMBS*, 2016, vol. 2016–Octob, pp. 3342–3345.
[78] P. Yushkevich, J. Piven, H. Cody, and S. Ho, “User-guided level set segmentation of anatomical structures with ITK-SNAP,” *Neuroimage*, vol. 31, no. 3, pp. 1116–1128, 2006.
[79] N. (University of I. Grosland, V. (University of I. Magnotta, S. (Isomics) Pieper, and C. (KnowledgeVis) Lisle, “Image to Finite Element Mesh : An End to End Workflow,” *Computing*. 2010.
[80] E. Clayton and M. S. Conradi, “Magnetic Resonance Elastography of the Brain : from Phantom to Mouse to Man,” *Electron. Theses Diss.*, pp. 1–684, 2012.
[81] N. Umov, “Poynting Vector,” *Physics (College. Park. Md).*, pp. 1–7, 2008.

Vita

Andrew A. Badachhape

Education

Ph.D. in Biomedical Engineering **December 2017**

Washington University in St. Louis, St. Louis, MO

Thesis: "Characterization of Structural Dynamics of the Human Head using Magnetic Resonance Elastography"

Mentor: Philip V. Bayly, Ph.D.

M.S. in Biomedical Engineering **August 2016**

Washington University in St. Louis, St. Louis, MO

B.S.E. in Bioengineering **May 2013**

Rice University, Houston, TX

Capstone Project: "A Low Cost Ambulatory Blood Pressure Monitor for the Developing World"

Research Experience

Brain Biomechanics Lab at Washington University in St. Louis
August 2013 – December 2017

Tkaczyk Optics Lab at Rice University
May 2012 – August 2012

Neurosciences Research Group at the Methodist Research Institute
May 2011 – September 2011

Publications

Badachhape, A.A., Okamoto, R. J., Johnson, C. L., and Bayly, P. V. 2017. Characterizing Coupled Human Brain, Scalp, and Skull Dynamics using Magnetic Resonance Elastography. *Journal of Biomechanics*. (In Review).

Badachhape, A.A ., Okamoto, R. J., Durham, R. S., Efron, B. D., Nadell, S. J., Johnson, C. L., and Bayly, P. V. 2017. The Relationship of 3D Human Skull Motion to Brain Tissue Deformation in Magnetic Resonance Elastography. *ASME Journal of Biomechanical Engineering*. DOI: 10.1115/1.4036146

Schmidt, J.L, Tweten, D.J., **Badachhape, A.A.**, Reiter, A.J., Okamoto, R.J., Garbow, J.R., and Bayly, P.V. 2017. Measurement of Anisotropy Mechanical Properties in Porcine Brain White Matter *ex vivo* using Magnetic Resonance Elastography. *Physics in Medicine and Biology*. (In Review).

Guertler, C.A., Okamoto, R.J., Schmidt J.L., **Badachhape, A.A.**, Johnson, C. L., and Bayly, P. V.2017. Mechanical Properties of Porcine Brain Tissue *in vivo* and *ex vivo* Estimated by MR Elastography. *Journal of Biomechanics* (In Review)

Conference Presentations

Badachhape, A.A., Okamoto, R. J., Johnson, C. L., and Bayly, P. V. 2017. Measurement of Human Brain, Scalp, and Skull Motion in vivo using Magnetic Resonance Elastography and Tri-axial Accelerometers. *ISMRM 25th Annual Meeting and Exposition,* Honolulu, HI.

Badachhape, A.A., Okamoto, R. J., Durham, R. S., Efron, B. D., Johnson, C. L., and Bayly, P. V. 2016. In Vivo Characterization of the Human Skull-Brain Interface using Magnetic Resonance Elastography. *BMES Annual Meeting.*

Badachhape, A.A., Durham, R.S., Okamoto, R.J., Johnson, C.L., Bayly, P.V., 2015. Relating Human Skull Acceleration to Brain Tissue Motion during Magnetic Resonance Elastography. *ASME IMECE*.

Guertler, C.A., Okamoto, R.J., Schmidt J.L., **Badachhape, A.A.**, Johnson, C. L., and Bayly, P. V.2017. Mechanical Properties of Porcine Brain Tissue *in vivo* and *ex vivo* Estimated by MR Elastography. *Summer Biomechanics, Bioengineering, and Biotransport Conference.*

Schmidt, J.L., Tweten, D.J., **Badachhape, A.A.,** Okamoto, R.J., Garbow, J.R., Bayly, P.V. 2016. Magnetic Resonance Elastography of White Matter Brain Tissue *Ex-Vivo. Summer Biomechanics, Bioengineering, Biotransport Conference*.

Okamoto, R.J., Johnson, C.L., Matthew D.M., **Badachhape, A.A.,** Sutton, B.P. Georgiadis, J.G., Bayly, P.V., 2014. Comparison of MR Elastography Inversion Methods on High-Resolution Measurements in the Human Brain. *ISMRM 22nd Annual Meeting and Exposition*.

Awards

Finalist – Washington University in St. Louis Outstanding BME Doctoral Research Award (2017)

1st Place – Third Annual National Undergraduate Global Health Technologies Design Competition (2013)

1st Place – Rice University Research Symposium (2013)

Teaching

Graduate Teaching Assistant, *Washington University in St. Louis* **Fall 2015**
Course: Biomedical Engineering Senior Design

Undergraduate Teaching Assistant, *Rice University* **Spring 2013**
Course: Digital Design and Visualization